

Charge correlations and collective dynamics in Pb–Pb collisions at $\sqrt{s_{\text{NN}}} = 2.76 \text{ TeV}$

Ladungsabhängige Korrelationen und kollektive Dynamik in Pb–Pb Kollisionen bei $\sqrt{s_{\text{NN}}} = 2.76 \text{ TeV}$

Zur Erlangung des Grades eines Doktors der Naturwissenschaften (Dr. rer. nat.)
genehmigte Dissertation von M.Sc. Jacobus Onderwaater aus Stavanger



TECHNISCHE
UNIVERSITÄT
DARMSTADT

Fachbereich Physik
Institut für Kernphysik

Charge correlations and collective dynamics in Pb–Pb collisions at $\sqrt{s_{NN}} = 2.76$ TeV
Ladungsabhängige Korrelationen und kollektive Dynamik in Pb–Pb Kollisionen bei $\sqrt{s_{NN}} = 2.76$ TeV

Genehmigte Dissertation von M.Sc. Jacobus Onderwaater aus Stavanger

Betreuer: Dr. Ilya Selyuzhenkov

1. Gutachten: Priv. Doz. Dr. Anton Andronic
2. Gutachten: Prof. Dr. Guy Moore

Prüfungskommission:

Priv. Doz. Dr. Anton Andronic

Prof. Dr. Guy Moore

Prof. Dr. Tetyana Galatyuk

Prof. Dr. Thomas Walther

Tag der Einreichung: 18 Oktober 2016

Tag der Prüfung: 7 November 2016

Darmstadt 2017 – D 17

Bitte zitieren Sie dieses Dokument als:

URN: urn:nbn:de:tuda-tuprints-69388

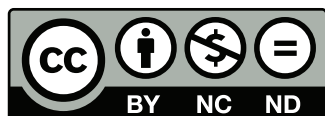
URL: <http://tuprints.ulb.tu-darmstadt.de/6938>

Dieses Dokument wird bereitgestellt von tuprints,

E-Publishing-Service der TU Darmstadt

<http://tuprints.ulb.tu-darmstadt.de>

tuprints@ulb.tu-darmstadt.de



Die Veröffentlichung steht unter folgender Creative Commons Lizenz:

Namensnennung – Keine kommerzielle Nutzung – Keine Bearbeitung 4.0 International

<https://creativecommons.org/licenses/by-nc-nd/4.0/deed.de>

Abstract

The theory of the strong force is called Quantum Chromodynamics (QCD). Within experimental limits it is observed that QCD respects \mathcal{CP} -symmetry, although there is no confirmed fundamental explanation for why this is the case. This is known as the strong \mathcal{CP} problem. Despite the observed symmetry conservation, it is expected that fluctuations in a larger system may locally result in a violation of \mathcal{CP} -symmetry. It was argued that local parity violation, which is driven by the nontrivial topological structure of the QCD vacuum, coupled with a strong magnetic field may result in a separation of charges along the direction of the magnetic field. This phenomenon is called the chiral magnetic effect (CME).

Relativistic heavy ion collisions such as at the LHC could meet the conditions for a measurement of the CME. For this, knowledge of the orientation of the magnetic field, which is perpendicular to the reaction plane, is needed. Collision symmetry planes can be estimated with Q -vectors that quantify the preference in the azimuthal direction of measured particles. To correct for detector imperfections in the measurement of the Q -vector, a ROOT-based correction framework was developed, building on corrections proposed by Selyuzhenkov and Voloshin. The functionality is increasingly used as a common tool in the ALICE collaboration. Due to its general applicability to data from heavy ion experiments, the package is publicly available and has already gained interest from researchers in CBM and NA61.

With understanding of the orientation of the magnetic field, the CME can be searched for with parity-even two- and multi-particle correlations, such as the charge dependence of two-particle correlations with respect to the reaction plane. However, these observables are also sensitive to the presence of background correlations, notably arising from the anisotropic flow modulation of locally created opposite charged particle pairs (local charge conservation), which obstructed a definite conclusion on the origins of the observed charge dependence.

This work presents the measurement of an extended set of mixed harmonic correlations based on $\langle \cos(\varphi_\alpha + \varphi_\beta - 2\Psi_{RP}) \rangle$, in Pb–Pb collisions at $\sqrt{s_{NN}} = 2.76$ TeV with ALICE, that characterize the facets of the shape of the signal. Additionally, the mentioned correlation is measured with one identified hadron (pion, kaon, or proton), reported as a function of the identified hadron transverse momentum. The measurements of the correlators with different sensitivity to the CME and background effects show varying degrees of charge dependence. The $\langle \cos(\varphi_\alpha + \varphi_\beta - 2\Psi_{RP}) \rangle$ correlation, which has maximum sensitivity to the CME but also background effects, shows a charge dependence increasing towards peripheral collisions, as is qualitatively in line with expectations. The second harmonic of this correlator is not sensitive to the charge separation perpendicular to the reaction plane, as associated to the CME, but can be used to quantify correlations from background sources, for example clusters of particles exhibiting charge conservation with angular correlations modulated by anisotropic flow, and is found to be consistent with zero within the systematic uncertainty. The measurement of the CME correlator with pions, kaons and protons reveals a particle type dependence in the charge dependence. More data for higher precision and model comparisons are required to make a better defined and quantitative conclusion about the contributions from background sources in the observation of the charge separation in the various correlations.



Zusammenfassung

Die Theorie der starken Kraft ist die Quantenchromodynamik (QCD). Innerhalb der experimentellen Grenzen wurde beobachtet, dass die QCD die \mathcal{CP} -Symmetrie erhält, obwohl keine bestätigte fundamentale Erklärung besteht, warum dies der Fall ist. Dies ist bekannt als starkes \mathcal{CP} Problem. Trotz der beobachteten Symmetrienerhaltung wird erwartet, dass individuelle Wechselwirkungen die \mathcal{CP} -Symmetrie in mikroskopischer Größenordnung innerhalb größerer Systeme verletzen. Es wurde vorgeschlagen, dass lokale Paritätsverletzung, hervorgerufen durch die nicht-triviale topologische Struktur des QCD-Vakuums, in Verbindung mit einem starken Magnetfeld, zu einer experimentell beobachtbaren Separation von Ladungen entlang der Richtung des Magnetfeldes führen könne. Dieses Phänomen wird chiraler magnetischer Effekt (CME) genannt.

Relativistische Schwerionenstöße, wie jene am LHC, könnten die Bedingungen für die Messung des CME erfüllen. Dafür sind Kenntnisse über die Orientierung des Magnetfeldes, das senkrecht zur Reaktionsebene steht, notwendig. Symmetrieebenen der Kollision können mit Q -Vektoren abgeschätzt werden, welche die bevorzugte azimuthale Richtung der gemessenen Teilchen quantifiziert. Um Detektor-Unvollkommenheiten in der Messung des Q -Vektors auszugleichen, wurde ein auf ROOT basierendes Korrektur-Framework entwickelt, aufbauend auf den von Selyuzhenkov und Voloshin vorgeschlagenen Korrekturen. Die Funktionalität findet zunehmend als ein verbreitetes Werkzeug in der ALICE-Kollaboration Verwendung. Aufgrund der allgemeinen Anwendbarkeit auf Daten aus Schwerionen-Experimenten ist das Paket öffentlich zugänglich und hat bereits das Interesse von Forschern in CBM und NA61 geweckt.

Mithilfe der erworbenen Kenntnisse über die Orientierung des Magnetfeldes kann der CME mittels paritätsgerader Zwei- und Vielteilchen-Korrelationen gesucht werden, wie der Ladungsabhängigkeit von Zweiteilchenkorrelationen in Bezug auf die Reaktionsebene. Diese Observablen sind jedoch ebenfalls sensitiv auf Untergrundkorrelationen, insbesondere hervorgerufen durch Modulationen lokal erzeugter ungleichnamig geladener Teilchenpaare (lokale Ladungserhaltung) durch den anisotropen Fluss, was eine definitive Antwort auf die Frage des Ursprungs der beobachteten Ladungsabhängigkeit verhinderte.

In dieser Arbeit wird eine Erweiterung von Messungen gemischt-harmonischer Korrelationen, basierend auf $\langle \cos(\varphi_\alpha + \varphi_\beta - 2\Psi_{RP}) \rangle$, Pb–Pb Kollisionen bei $\sqrt{s_{NN}} = 2.76$ TeV, gemessen durch ALICE, vorgestellt, welche die Aspekte der Form des Signals charakterisieren. Außerdem wurde die erwähnte Korrelation mit einem identifizierten Hadron (Pion, Kaon oder Proton) gemessen. Sie wird als Funktion des Transversalimpulses des identifizierten Hadrons präsentiert. Die Messungen von Korrelatoren mit unterschiedlich starker Sensitivität bezüglich des CME und Untergrundeffekten zeigen unterschiedlich starke Ladungsabhängigkeit. Die $\langle \cos(\varphi_\alpha + \varphi_\beta - 2\Psi_{RP}) \rangle$ -Korrelation, die maximale Sensitivität bezüglich CME, aber auch bezüglich Untergrundeffekten aufweist, zeigt eine zu peripheren Kollisionen hin zunehmende Ladungsabhängigkeit, was qualitativ mit Erwartungen übereinstimmt. Die zweite Harmonische dieses Korrelators ist nicht sensitiv auf Ladungstrennung senkrecht zur Reaktionsebene, wie sie mit dem CME verbunden wird, kann jedoch benutzt werden, um Korrelationen aus Untergrundbeiträgen zu quantifizieren, wie

zum Beispiel Cluster von Teilchen, die Ladungserhaltung aufweisen mit Winkelkorrelationen, die vom anisotropen Fluss moduliert werden. Innerhalb der systematischen Unsicherheiten ist diese nicht von Null verschieden. Die Messung des CME-Korrelators mit Pionen, Kaonen und Protonen offenbart eine Abhängigkeit vom Teilchentyp in der Ladungsabhängigkeit. Messungen mit höherer Statistik und Modell-Vergleiche sind notwendig, um besser bestimmte und quantitativere Schlussfolgerungen bezüglich der Anteile von Untergrundbeiträgen in der Beobachtung der Ladungstrennung in den verschiedenen Korrelationen zu ziehen.

Contents

1	Introduction	7
1.1	Fundamental forces of nature	7
1.2	Standard model	8
1.3	Quantum-chromo dynamics	9
1.4	The QCD phase diagram	11
1.5	Fundamental symmetries	11
1.6	Chiral anomaly & the QCD vacuum	13
1.7	Heavy-ion collisions at relativistic energies	13
1.7.1	Collision geometry and related phenomena in heavy-ion collisions	15
1.7.2	Chiral Magnetic Effect	20
2	The ALICE experiment at the LHC	25
2.1	Large Hadron Collider	25
2.2	The ALICE experiment	25
2.2.1	Particle tracking and identification	27
2.2.2	Forward detectors	32
2.2.3	Triggers	33
2.2.4	Event characterization	34
3	Anisotropic flow methods and flow vector corrections	37
3.1	Flow methods	37
3.1.1	The Q-vector	37
3.1.2	Event plane method	37
3.1.3	Scalar product method	38
3.1.4	Cumulant method	38
3.2	Q-vector corrections	39
3.2.1	Recentering, diagonalization and rescaling	39
3.2.2	Misalignment	41
3.2.3	Extraction of correction parameters for diagonalization and rescaling	41
3.2.4	Gain equalization	43
3.3	Implementation of correction procedure	43
3.3.1	Software package <i>FlowVectorCorrections</i>	44
3.4	Toy Monte Carlo study	45
3.5	Corrections with ALICE data	46
3.5.1	Signal equalization	47
3.5.2	Q-vector recentering	50
3.5.3	Q-vector alignment	50
3.5.4	Higher order corrections	51
3.5.5	Measurement of event plane resolution correction factors	52

3.5.6	Elliptic flow with multiple event planes	53
3.5.7	Limitations on the corrections for the Q -vector.	54
3.6	Summary	56
4	Charge-dependent correlations	57
4.1	Correlators	57
4.1.1	Sensitivity to the CME	58
4.1.2	Sensitivity to local charge conservation	59
4.1.3	Sensitivity to anisotropic flow fluctuations	60
4.1.4	Other sources of charge dependent correlations	60
4.2	Measurement technique	61
4.3	Experimental setup	61
4.3.1	Event selection	61
4.3.2	Track selection	62
4.4	Systematic uncertainties	62
4.4.1	Track reconstruction and quality cuts	65
4.4.2	Charge combinations	67
4.4.3	Sine term	67
4.4.4	Event planes	67
4.4.5	Closure test for identified particle correlations	68
4.5	Results	70
4.5.1	Two particle correlation	70
4.5.2	First and second moments of the two particle correlation relative to Ψ_n	71
4.5.3	Mixed harmonic correlation with the first moment relative to Ψ_n	72
4.5.4	Moments of the two particle correlation differentially	72
4.5.5	Three particle correlation with identified particles	75
4.6	Summary	76
5	Conclusions and outlook	79
6	Appendix	81
6.1	Run list	81
	List of Figures	92
	List of Tables	93

1 Introduction

The matter in our universe presents us with a puzzle of which only parts are solved. From astronomical observations it is estimated that 96% percent of the matter in our universe is of unknown origin; so far no theories for hypothetical dark matter candidates have been supported with experimental evidence, but searches are being expanded and will continue in the foreseeable future. The other 4% is made up by particles which were all discovered in the 20th century: protons, neutrons, electrons, photons and neutrino's. The protons and neutrons themselves consist of more fundamental particles, the so-called quarks. The quarks and the other fundamental particles make up the elementary particles of the Standard Model, which provides an incredibly accurate framework for many properties of the different particles. However there are still open questions, for example the underlying reason for the values of the free parameters in the Standard Model (like the Higgs mass), or the exact properties of neutrinos. These open questions drive many fields of research in nuclear physics, particle physics and astronomy.

The Standard Model includes a theory for interactions between quarks and gluons called Quantum Chromodynamics (QCD). In the matter of the visible universe, QCD binds quarks in protons and neutrons. If nuclear matter is pushed to a state of extreme temperature and density, the quarks will no longer be confined and can behave as free particles in a new phase of matter called the Quark Gluon Plasma (QGP). After the Big Bang, as the universe was created and before atoms existed, for a few microseconds QGP was the state of matter in the universe. Currently it exists nowhere except for a tiny fraction of a second in heavy ion collisions, and possibly in the core of neutron stars. The creation of QGP requires a considerable investment in the construction and operation of large colliders, such as the existing Relativistic Heavy Ion Collider (RHIC) in Brookhaven and the Large Hadron Collider (LHC) at CERN, as well as the particle detectors that are placed at various interaction points around them. Other than for the study of QGP, colliders are very useful tools to study the properties of individual particles, to search for new fundamental particles (Higgs or supersymmetric particles), composite particles (tetra- or pentaquarks), or detect other previously unseen (un)expected interactions. The colliders function as huge microscopes which allow to probe interactions between particles far below the nuclear (1 fm) length scale. By making observations and developing models or new theories to describe or predict those observations, we improve our understanding of fundamental interactions and matter.

1.1 Fundamental forces of nature

Everything we know in our universe is subjected to at least one of the four fundamental forces of nature, which are the strong, weak, electro-magnetic and gravitational force.

In everyday life, the strong force (the strongest force), which acts within atomic range (1 fm), is the force that binds nuclei together, overcoming the Coulomb repulsion of the electrically charged protons. The electromagnetic force locks electrons into orbit around the nuclei, and its massless force carriers, the photons, illuminate the universe with indefinite range. The weak

Force	Relative strength [1]	Force carriers	Range
Strong	1	Gluons (g)	$10^{-15}m$
Electro-magnetic	10^{-2}	Photon (γ)	∞
Weak	10^{-6}	Intermediate vector boson (Z, W^{\pm})	$10^{-18}m$
Gravity	10^{-39}	-	∞

Table 1.1: The fundamental forces and their relative strength (at 1 GeV), force carriers and ranges. A force carrier for the gravitational force has not (yet) been experimentally verified.

force is responsible for β -decay. Gravity warps time and space and affects everything existing in that space. Early in the 20th century it became understood that the electro-magnetic force was carried in energy packages (quanta). This required a new perspective on the interactions of this force and led to the development of quantum mechanics. The concept of quantum force carriers was also part of the upcoming strong and weak theories. Only the gravitational force yet escapes this concept, though gravitons and similar force carriers are postulated in yet unverified theories.

1.2 Standard model

The force carriers of the fundamental forces and the fundamental particles whose interactions they mediate together make up the particles of the Standard Model, shown in Figure 1.1.

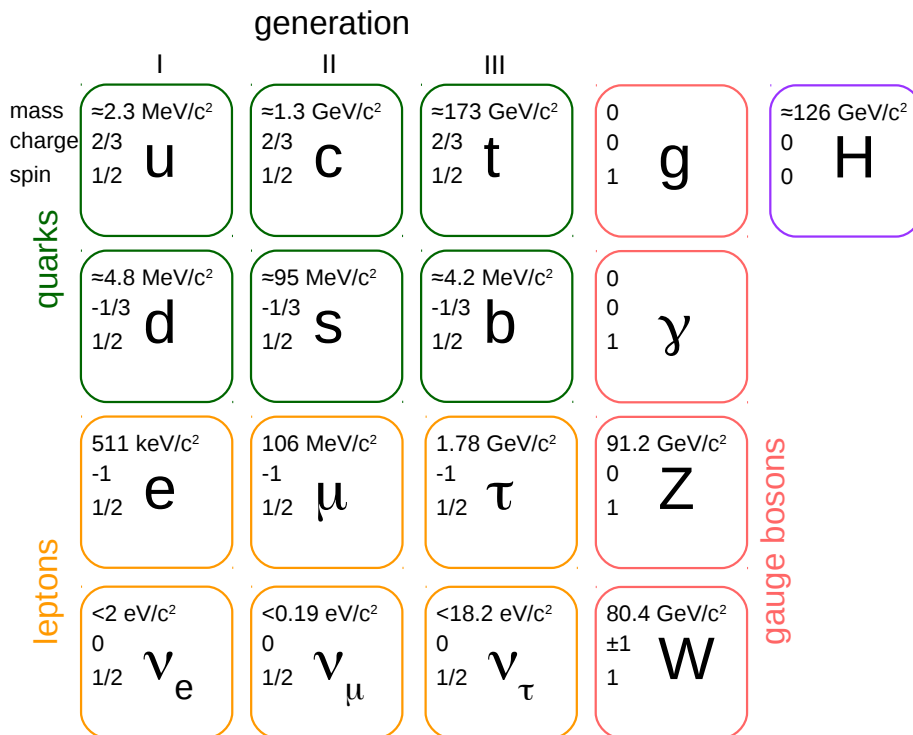


Figure 1.1: The Standard Model of elementary particles.

The particles in the electromagnetic sector are three generations of fermions, electrons, muons, and taus, as well as the electromagnetic force mediator, the neutrally charged photon. The quarks which are principally in the strong sector are fractionally charged and also interact electromagnetically, as do the W bosons in the weak sector. In the strong sector there are three generations of quarks, which are the fundamental particles of all hadrons. They come in three flavours: *red*, *green*, *blue*. The gluons themselves also carry color, and cause a self-interaction not seen in the electromagnetic sector. In the weak sector the W and Z bosons are the only particles to interact with three neutrally charged neutrinos, but interact also with all other known existing particles. With the recent discovery of the Higgs boson which explains the mechanism through which particles acquire mass, the existence of the last particle of the standard model was confirmed experimentally.

1.3 Quantum-chromo dynamics

The strong force only applies to particles carrying ‘color’, namely quarks and gluons. The theory describing the strong interactions between these particles is called quantum-chromo dynamics (QCD). In addition to the color charge, quarks carry fractional electric charge, $\frac{2e}{3}$ for u, c, t and $-\frac{1e}{3}$ for d, s, b quarks, and all have spin $\frac{1}{2}$. Of the six quarks, only the lightest two, the u and d quarks, are stable. The symmetry of QCD with respect to the color charges is described by the Lie group $SU(3)$. The group is generated by eight independent Hermitian traceless matrices. There is one gauge field associated to each independent generator. The QCD Lagrangian is

$$\mathcal{L}_{QCD} = \sum_q \bar{\psi}_{q,a} (i\gamma^\mu \partial_\mu \delta_{ab} - g_s \gamma^\mu t_{ab}^C A_\mu^C - m_q \delta_{ab}) \psi_{q,b} - \frac{1}{4} (F_{\mu\nu}^A)^2, \quad (1.1)$$

where γ^μ are the Dirac matrices, $\psi_{q,a}$ the quark fields spinor for quarks with flavor q and mass m_q , which have 3 possible color charges from $a = 1..3$. A_μ^C are the eight gluon potentials with $C = 1..8$ for the eight types of gluon. t_{ab} represents the eight generators of $SU(3)$ (related to the Gell-Mann matrices by $t_{ab} = \lambda_{ab}/2$) and g_s is the dimensionless QCD coupling constant. The gluon field tensor $F_{\mu\nu}^A$ is

$$F_{\mu\nu}^A = \partial_\mu A_\nu^A - \partial_\nu A_\mu^A - g_s f_{ABC} A_\mu^B A_\nu^C, \quad [t^A, t^B] = i f_{ABC} t^C, \quad (1.2)$$

with f_{ABC} the structure constants of the $SU(3)$ group. The first two terms are also familiar to QED, being the kinetic term of a massless vector field. But the last term is very different, it introduces the self interaction of gluons. Using Feynman rules one can now calculate different interactions between quarks and gluons, including 2- and 4-gluon vertices which have no equivalent in QED. The structure of the QCD Lagrangian is defined by local gauge invariance under $SU(3)$ transformations.

The coupling of the strong interaction (as of the EM interaction) depends on the transferred energy. This has two reasons. One is due to ‘dressing’ of the leading order (LO) diagram (gluon/quark loop) with higher order diagrams (double gluon/mixed quark-gluon loops etc.) as the energy is increased, which modifies the measured ‘effective’ coupling. Predictions for observables in QCD rely on renormalization because of this changing coupling with the momentum scale, $\alpha_s(\mu_R^2)$, and is described by the renormalization group equation (RGE):

$$\mu_R^2 \frac{d\alpha_s}{d\mu_R^2} = \beta(\alpha_s) = -\frac{33 - 2n_f}{12\pi} \alpha_s^2 + \mathcal{O}(\alpha_s^3), \quad (1.3)$$

where β_0 is LO beta-function coefficient. The LO loop has two vertices, hence the scaling with α_s^2 . The number of flavors n_f changes with the energy scale. Below the charm threshold, $n_f = 3$, and the value increases incrementally as the threshold for heavier quarks is reached. The minus sign reflects that the coupling gets weaker at higher momentum scales. If one takes the number of flavors as constant and ignoring higher orders, the coupling is given by

$$\alpha_s(\mu_R^2) = \frac{1}{b_0 \ln(\mu_R^2/\Lambda_{\text{QCD}}^2)} \quad (1.4)$$

The integration constant Λ_{QCD} sets the non-perturbative scale of QCD, it is experimentally determined as $\Lambda_{\text{QCD}} \approx 200\text{MeV}$.

QCD can be characterized by two main features: confinement and asymptotic freedom. Confinement is the requirement that all observable objects in nature are neutral in color. That means that particles carrying color ((anti-)red, (anti-)blue and (anti-)green) are part of a composite object that overall is color neutral. Hence we can combine quarks in color-anticolor pairs (mesons) and in red-green-blue (antired-antigreen-antiblue) triplets (baryons). One can also imagine color neutral objects consisting of four quarks (possibly recently observed by LHCb) or five or more quarks. Also composite gluon objects (glueballs) or the gluon singlet are a possibility.

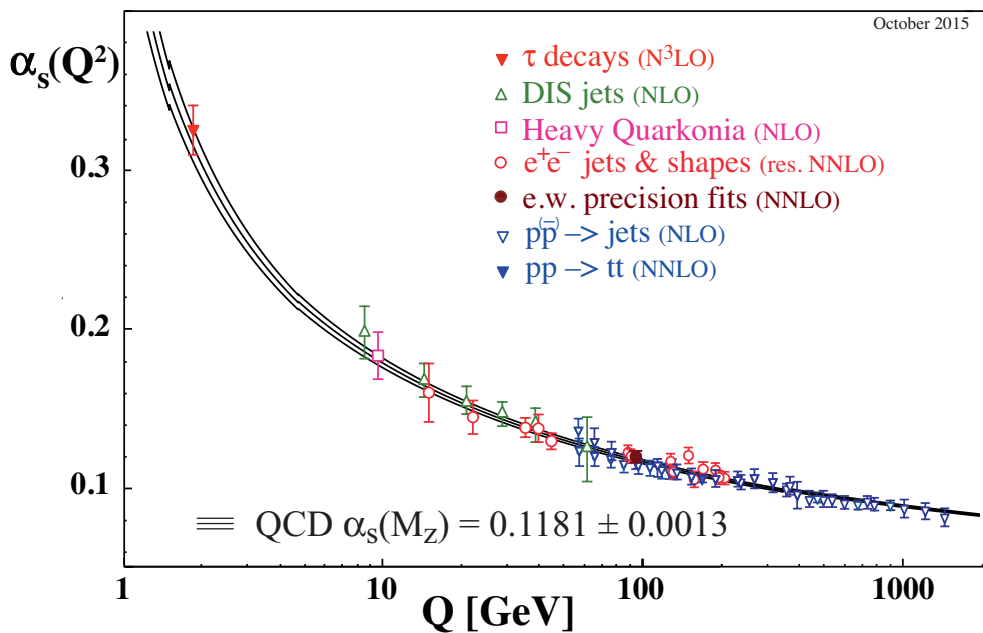


Figure 1.2: Running of the strong coupling constant [2].

Asymptotic freedom is the dependence of the coupling (strength) $\alpha_s = \frac{g_s^2}{4\pi}$ of the strong force on the energy transfer Q between two interacting bodies. As shown in Figure 1.2, if the energy transfer is small, the coupling is large. Conversely for high energy transfer, the coupling is small. As a result of asymptotic freedom, at high energies it is possible to precisely calculate the total likelihood of the interaction by considering the likelihood of specific paths that the strong force can mediate the interaction (this regime is called perturbative QCD, or pQCD). However at low energies ($\alpha_s > 1$), the more complex the path, the more likely it becomes, and precise calculations become impossible (this regime is called non-perturbative QCD). The concept of

asymptotic freedom also led to the prediction that at very large densities, quarks and gluons can form a soup where they barely interact with each other.

1.4 The QCD phase diagram

An instructive illustration of how the strong force shapes the phases of partonic matter is shown in Figure 1.3, where (net) baryon density is plotted on the x -axis and temperature on the y -axis. The world around us consists of partons contained in protons and nucleons in the ground state. In the early universe the temperature was high and net baryon density close to 0 (the matter/anti-matter asymmetry notwithstanding). The current generation of relativistic heavy ion collisions probe the same region of the phase diagram, up to approximately 300 MeV. Surrounding the region of normal nuclei is the hadronic matter, in which phase partons are confined in color neutral objects. This is also the region where chiral symmetry is broken, which generates most of the mass of the light flavor hadrons. If we compress baryonic matter sufficiently, or heat it enough, the relevant degrees of freedom change from hadrons to partons and a phase transition occurs to the quark-gluon plasma. At the same boundary, or close to it, chiral symmetry is restored and the quarks only carry the bare Higgs mass. At low baryonic density, lattice QCD calculations indicate that the phase transition is crossover [3]. For higher baryonic densities, it is expected that there is a critical point beyond which the phase transition is of first order. The CBM experiment at the future FAIR facility will probe the phase diagram towards high baryon density, and provide measurements in the search of the critical endpoint.

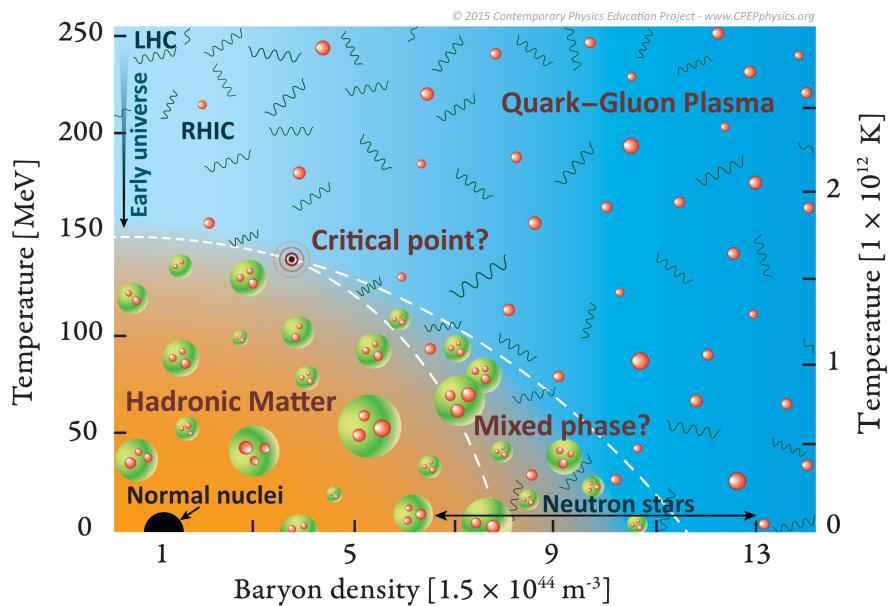


Figure 1.3: The QCD phase diagram [4].

1.5 Fundamental symmetries

Symmetry was defined by Weyl in the following way [5]: if one doesn't change the physical observation by changing something about an object, the change itself is connected to a symmetry.

Operation	Conservation
Translation in space	momentum
Rotation in space	angular momentum
Translation in time	energy
Uniform velocity in a straight line	Lorentz invariance
Reversal of time	
Reflection of space	Parity
Interchange of identical atoms or identical particles	
Quantum-mechanical phase	Charge
Matter-antimatter	Baryon number Lepton number

Table 1.2: Symmetry operators and corresponding conservation laws.

Later Noether recognized that for every symmetry continuous there is a conservation law [6]. In nature, there are many symmetries that are perfectly upheld. Others are slightly broken, but are still useful to describe related phenomena. The following table lists an overview of symmetries and their corresponding conservation laws.

There are two types of symmetry breaking: explicit and spontaneous. Examples of explicit symmetry breaking is through the presence of mass. Isospin symmetry is explicitly broken in the light quark doublet due to the different masses of the u and d quarks. The Brout-Englert-Higgs mechanism is an example of spontaneous symmetry breaking. The non-zero vacuum expectation value gives rise to a scalar boson that gives mass to the Z and W bosons while leaving the photon massless, breaking the electroweak symmetry. It was long thought that the discrete symmetries of Parity (\mathcal{P}), Charge (\mathcal{C}) and Time (\mathcal{T}) were fundamental and preserved symmetries of nature. In 1953, particle physicists were confronted with the $\theta - \tau$ puzzle. Two decay processes were observed that pointed to a parent particle with identical properties, however due to their different intrinsic parity (the θ decays to two pions and has parity $+1$, while the τ decays to three pions and thus has parity -1), \mathcal{P} -conservation dictated that the θ and τ are two distinct particles. Lee and Yang thought that parity might be violated in weak interactions and suggested an experiment to test the assumption [7]. Wu led the experiment where ^{60}Co was cooled to low temperatures and placed in an external magnetic field, which caused the nuclear spin to align. It was observed that the electrons from the β -decaying cobalt had a preferential direction along the nuclear spin [8]. In a parity transformation of this setup, the electrons would travel opposite to the nuclear spin. Thus this observation proved P -violation in weak decays, and the $\theta - \tau$ puzzle was resolved since they were now allowed to be the same particle (the K^+). From the discovery that neutrinos only couple when they are left-handed neutrinos or right-handed antineutrinos, it was clear that also \mathcal{C} -symmetry is violated. It was thought that \mathcal{CP} -symmetry might still be preserved, but this was disproven with the discovery of the \mathcal{CP} violating decay $K_L^0 \rightarrow \pi^+ \pi^-$ in the Cronin-Fitch experiment in 1964 [9].

1.6 Chiral anomaly & the QCD vacuum

The QCD Lagrangian as commonly described in the previous section in fact has a generalized version that includes an additional term that explicitly allows for \mathcal{CP} -violation:

$$\mathcal{L} = \theta \frac{\alpha_s}{8\pi} F_{\mu\nu}^A \tilde{F}^{A\mu\nu}. \quad (1.5)$$

This part of the Lagrangian, where θ is a free parameter, has important implications in QCD. The value of θ determines the vacuum structure. The vacuum is not empty but consists of particle pairs jumping in and out of existence. There are an infinite number of solutions for the ground state, each corresponding to a local minimum in the energy. From measurements of the neutron dipole moment, the value of θ is constrained to $\theta \leq 10^{-10}$ and indicates that globally \mathcal{CP} -symmetry is to high extent conserved. Other (so far less constraining) methods include measuring the branching ratio of \mathcal{CP} -violating decays, for example $\eta \rightarrow \pi^+ \pi^-$ [10]. \mathcal{CP} -symmetry may still be violated locally as follows. An infinite number of solutions exist for the ground state, parametrized by the Chern-Simons number (N_{CS}) which corresponds to a specific region of the gluon potential. It was found that the chiral anomaly gives rise to transitions between the different states [11–13], which results in symmetry non-conserving effects. In an environment of high energy density, a state can transition to another through an instanton (tunneling) or sphaleron (over the potential barrier). Such a transition implies changing N_{CS} and is \mathcal{CP} -odd. Above $\Lambda_{\text{QCD}} \approx 200$ MeV, it is thought that while instantons are suppressed, the rate of sphaleron transitions greatly increases [14]. Massless quarks present in regions with nonzero N_{CS} can interact with this field configuration, after which

$$(N_L - N_R) = 2N_{CS}, \quad (1.6)$$

where N_L and N_R are the number of respectively the left- and right-handed quarks. This effect may lead to observations such as discussed in the next section.

1.7 Heavy-ion collisions at relativistic energies

At the RHIC and LHC accelerator complexes, heavy nuclei are accelerated up to high relativistic energies (currently up to a maximum of $\sqrt{s_{\text{NN}}} = 200$ GeV and $\sqrt{s_{\text{NN}}} = 5.26$ TeV) respectively. As shown in the left panel of Figure 1.4, as observed from the lab frame (which coincides with the rest frame for beams containing identical particles), the Lorentz factor contracts the nuclei along the beam axis and both nuclei are observed as two flat disks. In the ensuing collisions between the ions, in addition to the mass density of the overlapping nuclei, a tremendous amount of kinetic energy is released by parton interactions and converted in mass and heat. In this dense and hot environment quarks and gluons are no longer confined in their initial color neutral objects. Instead, they can move freely through the medium. This phase of matter is called the quark gluon plasma (QGP). The properties of this deconfined matter and the study thereof lie at the heart of the physics programs at RHIC, as well as the dedicated ALICE experiment at the LHC. When the medium expands it cools down and the particles are again confined to hadrons in a process called hadronization. Aside from the usual up and down quarks that make up almost all hadrons in our universe, the energy in the collision is sufficient to produce a wealth

of particles drawn from the building blocks of the standard model. Some are very short lived, like the Z-boson, but other particles travel through the medium before they, or their remnants, are registered in detectors that function as state-of-the-art 3d cameras recording almost all particles and several particle properties as they pass through the detector. Through the tedious process of putting all pieces back together, the goal is to obtain a full picture of the particles created in the collision and their behaviour, and consequentially increase our understanding of the laws that govern them.

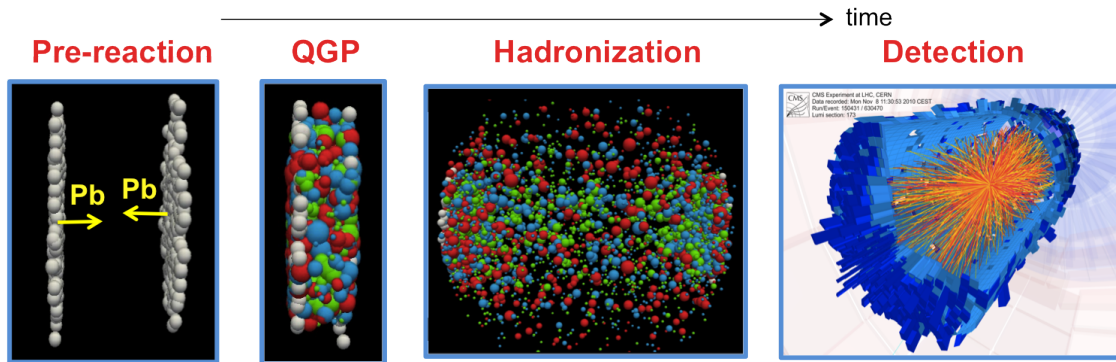


Figure 1.4: Sketch of a relativistic heavy ion collision [15].

We can look closer at the timeline of the heavy ion collision in Figure 1.5, where the beam is displayed as a lightcone (since it is moving very close to the speed of light), with on the horizontal axis the beam direction and on the vertical axis the proper time ($\tau = t/c$). At the axis origin the lead nuclei collide. Through scatterings in the following first tenths of femtoseconds matter is created in the collision volume. Most of the hard scatterings, and thus the creation of heavy quarks and bosons, take place in this initial collision stage. Through not exactly known mechanisms the produced particles thermalize very quickly. This means that the momentum distribution of the matter throughout the volume is thermal and consequently the laws of thermodynamics apply. At this moment the matter in the ‘fireball’ consists of QGP with a temperature of several hundred MeV. In this stage it appears that the evolution of the matter with time can be described with hydrodynamical models (a prerequisite for which is thermalization and a short mean free path). After several femtoseconds of expansion and cooling the QGP transitions to a hadron gas. This transition in itself is also one worth of extensive studies, regarding the phase transition, the critical point and the mechanism of color recombination. In the hadron gas the particles are still interacting, as well as evolving hydrodynamically. Then first chemical freeze-out occurs (particles can no longer be created or destroyed). After the kinetic freezeout (τ_f) particles no longer interact and enter the vacuum (and then possibly a detector).

Heavy-ion collisions are often popularly described as ‘little big bangs’, the reason for which can be quickly glanced from the right side of Figure 1.5. In the laboratory the conditions of the early universe (between 10^{-10} and 10^{-5} s) are recreated, and from that moment follow a similar evolution. It is remarkable that with something as small as two nuclei, we can recreate an environment that resembles a state where all existing energy of the universe was relatively concentrated. Hence heavy-ion collisions are closely related to and can increase our understanding of fundamental interactions and the evolution of our universe.

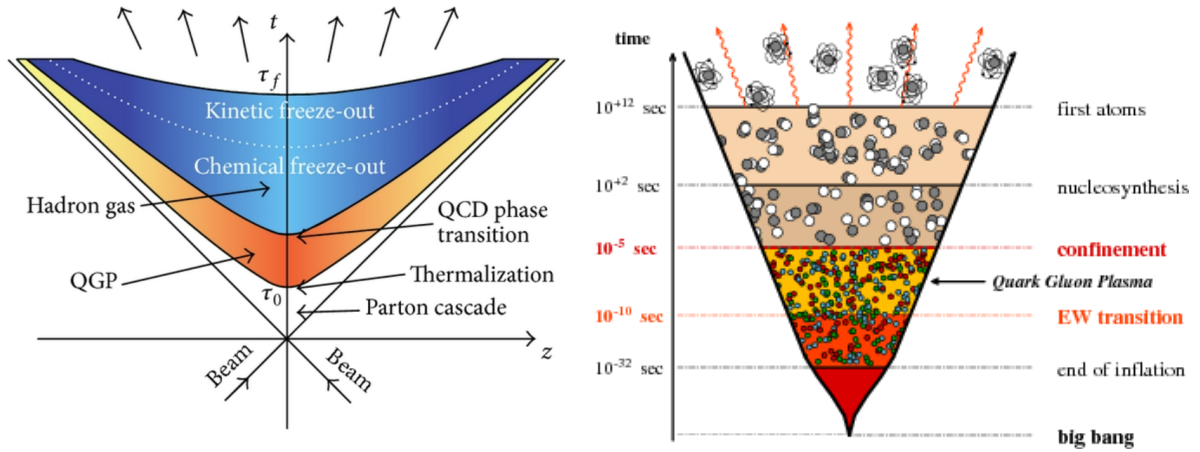


Figure 1.5: Different phases of heavy ion collision (left) [16] and the early universe (right) [17].

1.7.1 Collision geometry and related phenomena in heavy-ion collisions

Several features of the heavy ion collision are determined by the geometric configuration of the nuclei. The nuclei are highly charged, fast moving objects which induce a radial magnetic field like the current in a wire. In the space between the centers of the nuclei, at the moment of the collision, the fields superimpose and create the strongest man-made magnetic field in the overlap region. The shape of the overlap area depends on the distance between the centers of the nuclei and their internal mass distribution. In the following sections we describe these features and their influence on the evolution of the collision in more detail.

In the general picture of two colliding nuclei as shown in Figure 1.6, the two nuclei approach each other with a transverse distance between the centers of the nuclei called the impact parameter b . The plane that is spanned by the impact parameter and the direction of the nuclei (parallel to the z -axis) is called the reaction plane Ψ_{RP} . The two orange circles show the projection of the nuclei on the $x - y$ plane.

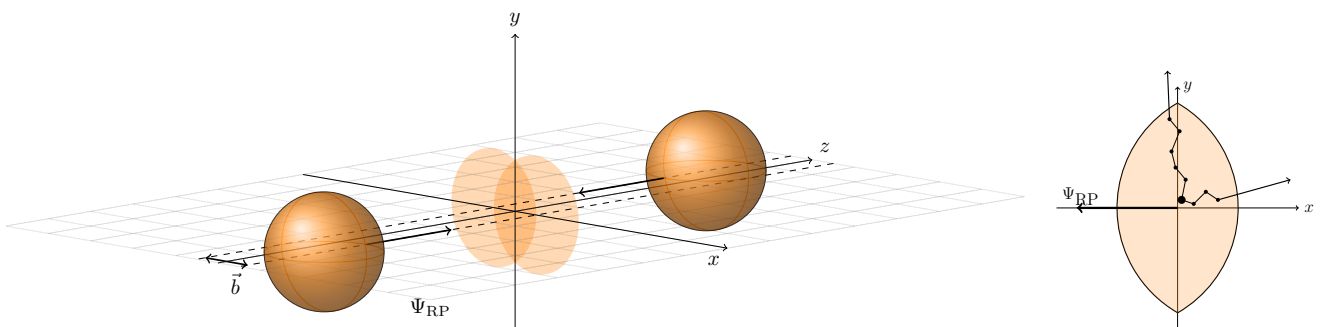


Figure 1.6: Left: the two nuclei approach each other along the direction of the z -axis with impact parameter b . The plane spanned by \vec{b} and \vec{e}_z is the reaction plane. Right: the spatial asymmetry develops through multiple scattering into a momentum asymmetry.

Anisotropic flow

From the distribution of matter and energy in the overlapping volume we can see pressure gradients going from maximum at the core to zero at the edge (the boundary with vacuum). This drives a collective radial expansion. In addition because of the almond shape the pressure gradient is stronger in x - than in y -directions. Through multiple scattering the particles are inclined to move along the pressure gradient and consequentially more particles move in x - than in y -direction. This effect is simulated in Figure 1.7 where the time development of the geometric eccentricity $\varepsilon_x(\tau) = \frac{\langle y^2 - x^2 \rangle}{\langle y^2 + x^2 \rangle}$, and the momentum anisotropy are shown following a hydrodynamic evolution.

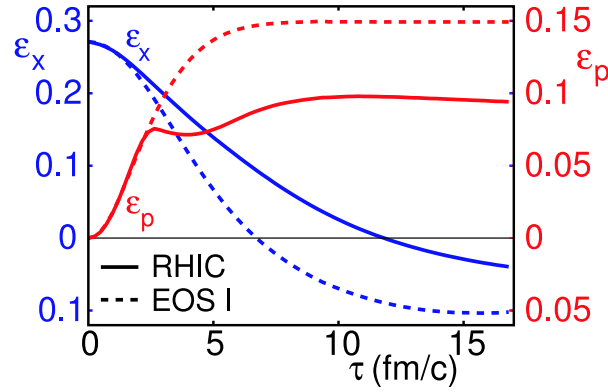


Figure 1.7: Simulation of the time evolution of the spatial and momentum anisotropy for Au–Au collisions at RHIC with $b = 7$ fm [18]. The two lines represent calculations with an equation of state for QGP only (EOS I) and one that additionally contains the phase transition to a hadronic system (RHIC).

This results in a non-isotropic azimuthal distribution of particles that can be registered in a detector. The modulation of the distribution can be quantified using a Fourier decomposition of measured spectra,

$$\frac{dN(p_T, y)}{d\phi} = \frac{1}{2\pi} \frac{d^2N}{p_T dp_T dy} \left(1 + \sum_{n=1}^{\infty} 2v_n \cos n(\varphi - \Psi_{SP}^{(n)}) \right). \quad (1.7)$$

Here n is the Fourier moment, v_n the corresponding amplitude, φ the azimuthal angle and $\Psi_{SP}^{(n)}$ the n^{th} harmonic symmetry plane. Generally there is no preferred out-of-plane direction which means that the sine terms are zero. Nevertheless there may exist phenomena that don't have this symmetry (see Section 1.7.2), in which case sine values can be of interest.

For the picture in Figure 1.6, the asymmetry creates a non-zero second harmonic Fourier moment, called v_2 or elliptic flow. It is expected that the magnitude of v_2 is proportional to the eccentricity of the overlap area, which relates to the impact parameter b . The eccentricity as a function of b is shown on the left side of Figure 1.8, where an optical Glauber model is used to calculate the initial anisotropy ε_x both for the wounded nucleon (WN) density, which scales with the number of 'soft' interactions, and the binary collision (BC) density, which scales with the number of 'hard' interactions [18]. In Figure 1.8 the elliptic flow as a function of collision centrality is shown. For low centrality (impact parameter), the overlap area is nearly circular

and v_2 is small, while for more peripheral collisions the eccentricity and v_2 increase. The value of v_2 does not reach zero for the most central collisions because event-by-event fluctuations in the positions of the nucleons prevent the initial overlap area from being isotropic, which is not taken into account in the calculations for the left figure.

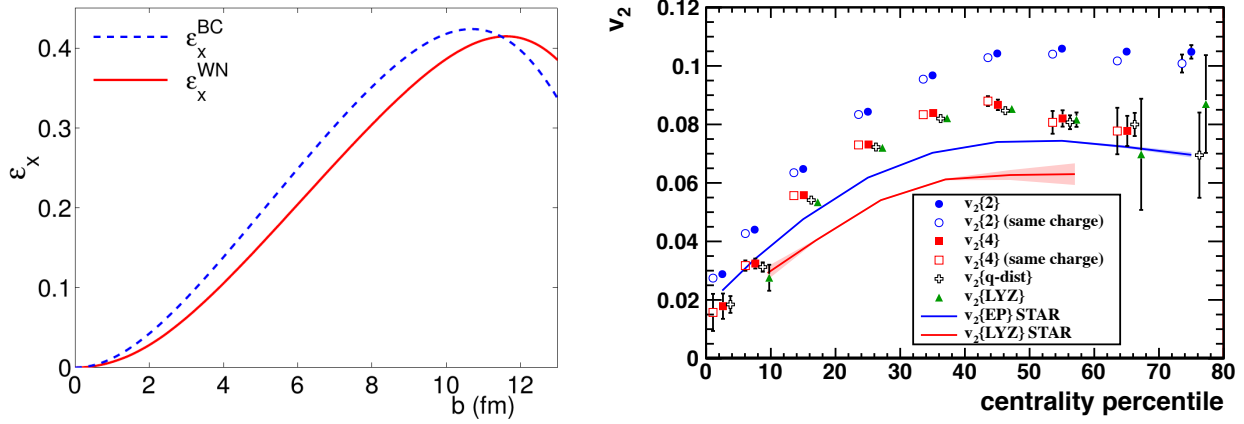


Figure 1.8: Left: the spatial anisotropy as a function of impact parameter b [18]. Right: elliptic flow v_2 for charged hadrons as a function of collision centrality for Pb–Pb collisions at $\sqrt{s_{\text{NN}}} = 2.76$ TeV [19].

When particle identification is applied in the measurement of elliptic flow, a mass scaling is observed that is further evidence of the hydrodynamic nature of the expansion. In a common velocity field, heavy particles pick up more momentum. This is visible in Figure 1.9. On the left side the v_2 as a function of transverse momentum is shown for several identified particles. At low momentum the light pions have high v_2 , while the proton v_2 increases at higher momenta. On the right side, the v_2 is measured as a function of the transverse kinetic energy divided by the number of quarks in the measured particle. This scaling provides a test of the quark coalescence picture, which implies that is the partonic content of the measured particles that is boosted during the medium evolution. As is visible in the figure, an approximate scaling is observed.

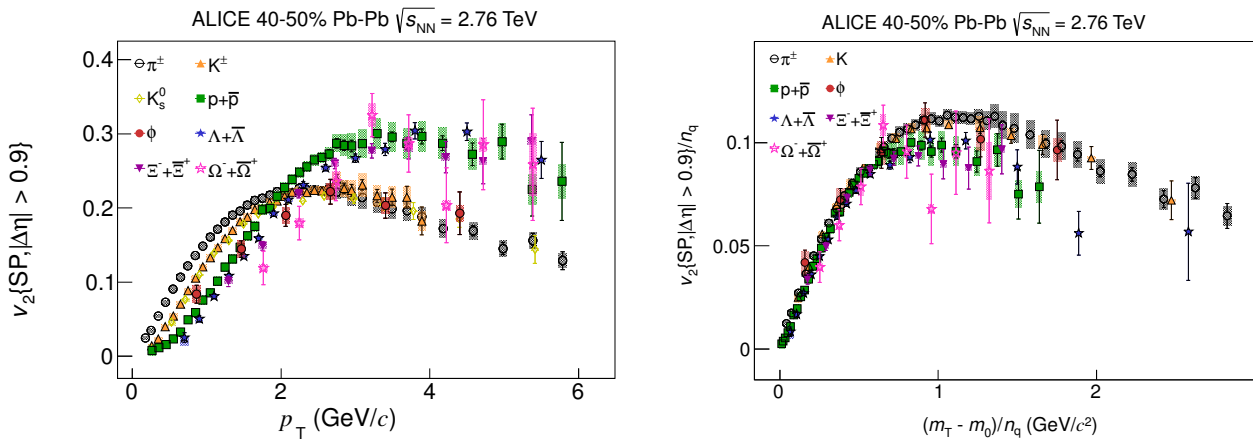


Figure 1.9: Left: Elliptic flow v_2 as a function of p_T . Right: Elliptic flow v_2 as a function of $(m_T - m_0)/n_q$ [20].

A closer view of the nuclear overlap area reveals that the nuclear matter density is not as smooth as depicted in Figure 1.6. Matter is clustered in nucleons, and the configuration of nucleons within a nucleus is fluctuating. In a nucleus-nucleus collision this means that the overlap area can not only take the shape of an ellipse, but also approximate a triangle, a square and so on. These initial conditions give rise to additional flow harmonics, which have been observed as well, as shown in Figure 1.10. The magnitude of elliptic flow for the higher harmonics is relatively independent of collision centrality.

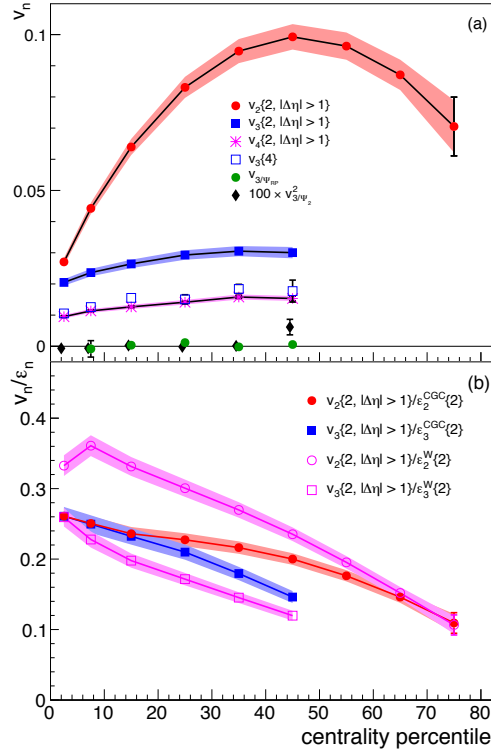


Figure 1.10: Fourier coefficients v_n as a function of centrality for $n = 2, 3, 4$ for Pb-Pb collisions at $\sqrt{s_{NN}} = 2.76$ TeV.

Magnetic field

According to Maxwell's equations, an electric current induces a magnetic field. Similarly the charges in heavy ions, which in the lab frame are moving at relativistic speed, generate a magnetic field. In fact, this field is the strongest magnetic field created in a laboratory. Possible effects due to its presence, including on the nature of the chiral phase transition and charge separation in the presence of a chiral imbalance [21], touch on fundamental physics and are of great interest.

So far no direct measurement of the magnetic field in heavy ion collisions exist, but with some assumptions the strength can be calculated. One of the earlier calculations [14] uses the following recipe. The magnetic field of a moving charge in the labframe is given by the Liénard-Wiechert potential:

$$e\mathbf{B}(\mathbf{x}) = Z\alpha_{EM} \sinh(Y) \frac{(\mathbf{x}'_{\perp} - \mathbf{x}_{\perp}) \times \mathbf{e}_z}{[(\mathbf{x}'_{\perp} - \mathbf{x}_{\perp})^2 + (t \sinh(Y) - z \cosh(Y))^2]^{3/2}}, \quad (1.8)$$

where \mathbf{x}_\perp denotes the transverse position of a charge Z moving along the beam axis \mathbf{e}_z with rapidity Y , and $\mathbf{x}'_\perp = \mathbf{x}_\perp(t=0)$.

When the nuclei are considered to be flat due to the Lorentz contraction the density can be projected on the $x-y$ plane, the number density is given by

$$\rho_\pm(\mathbf{x}_\perp) = \frac{2}{\frac{4}{3}\pi R^3} \sqrt{R^2 - (\mathbf{x}'_\perp \pm \mathbf{b}/2)^2} \theta_\pm(\mathbf{x}'_\perp), \quad (1.9)$$

where the projections of the nuclei on the transverse plane are

$$\theta_\pm(\mathbf{x}'_\perp) = \theta[R^2 - (\mathbf{x}'_\perp \pm \mathbf{b}/2)^2] \quad (1.10)$$

and \pm is the sign of the direction along \mathbf{e}_z .

Now we can look at the contribution of the charges in the colliding nuclei. The spectators can be considered to continue their movement undisturbed after the collision. For the participants the distribution becomes

$$f(Y) = \frac{a}{2 \sinh(aY_0)} e^{aY}, \quad -Y_0 \leq Y \leq Y_0 \quad (1.11)$$

where Y_0 is the rapidity along the beam axis, which depends on the energy, and a is a factor related to baryon stopping, experimentally determined to be around 0.5.

The magnetic field from the spectators can then be calculated with

$$e\mathbf{B}_s^\pm(\tau, \eta, \mathbf{x}_\perp) = \pm Z \alpha_{EM} \sinh(Y_0 \mp \eta) \int d^2 \mathbf{x}'_\perp \rho_\pm(\mathbf{x}'_\perp) [1 - \theta_\mp(\mathbf{x}'_\perp)] \quad (1.12)$$

$$\times \frac{(\mathbf{x}'_\perp - \mathbf{x}_\perp) \times \mathbf{e}_z}{[(\mathbf{x}'_\perp - \mathbf{x}_\perp)^2 + \tau^2 \sinh(Y_0 \mp \eta)^2]^{3/2}}, \quad (1.13)$$

and the participants with

$$e\mathbf{B}_p^\pm(\tau, \eta, \mathbf{x}_\perp) = \pm Z \alpha_{EM} \int d^2 \mathbf{x}'_\perp \int_{-Y_0}^{Y_0} dY f(Y) \sinh(Y \mp \eta) \rho_\pm(\mathbf{x}'_\perp) \theta_\mp(\mathbf{x}'_\perp) \quad (1.14)$$

$$\times \frac{(\mathbf{x}'_\perp - \mathbf{x}_\perp) \times \mathbf{e}_z}{[(\mathbf{x}'_\perp - \mathbf{x}_\perp)^2 + \tau^2 \sinh(Y_0 \mp \eta)^2]^{3/2}}. \quad (1.15)$$

Here $\tau = \sqrt{t^2 - z^2}$ is the proper time. In this approximation the particles that are produced in the overlap area are neglected, since their net charge is zero due to charge conservation and the directions are roughly outward, resulting in a much smaller contribution compared to from the charges that are initially present. An evaluation of the above equations at the origin for Au–Au collisions at 200 GeV is shown on the left side of Figure 1.11 for different impact parameters. The initial value of the magnetic field shows an enormous magnetic field of $e\mathbf{B} \sim 3m_\pi^2 \sim 3 \times 10^{18}$ Gauss [21], and it increases with increasing impact parameter. More recently calculations of the magnetic field have been developed that better encapsulate the dynamics of the heavy ion collision and medium properties [21, 22]. On the right side of

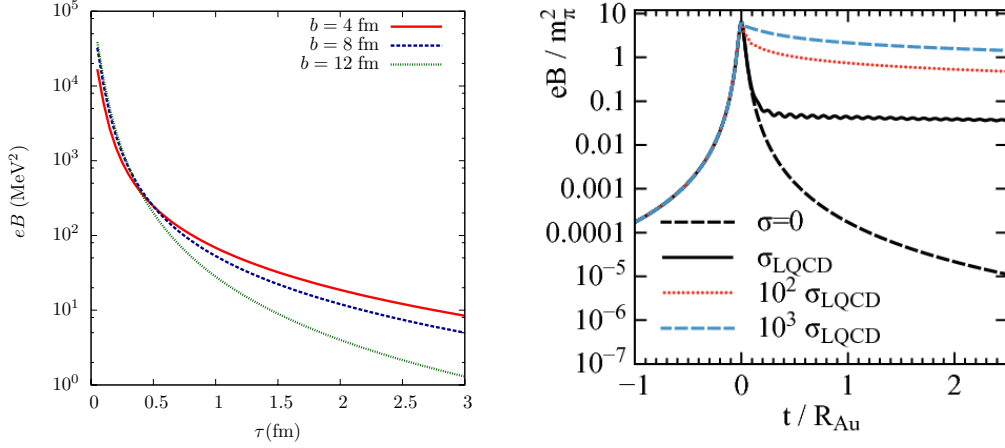


Figure 1.11: The time evolution of the magnetic field in heavy ion collisions for different impact parameters (left) [14] and values for the electric conductivity (right) [21] at RHIC top energy for Au–Au collisions.

Figure 1.11 such a calculation with the use of transport models is presented [21]. Here is also visible how the magnitude of the magnetic field rapidly increases as the nuclei approach each other. The development after the collision is less clear, as it depends on the properties of the medium, especially the electric conductivity.

For the right panel in Figure 1.11, the electric conductivity for QCD matter is estimated with lattice QCD (σ_{LQCD}). For $\sigma = 0$, the field decreases as rapidly as it increased. The presence of electric conductivity to great effect upholds the magnetic field. Despite the uncertainties related to the evolution of the magnetic field, experimental searches to related phenomena are of great interest. An example is the origin of the measured elliptic flow of direct photons [23], charge dependent elliptic flow [24] and other charge dependent correlations [25, 26], among others. For a recent overview see [27].

1.7.2 Chiral Magnetic Effect

In Section 1.6, a description was given of parity violating transitions in the QCD-vacuum that couple to either left- or right-handed quarks and induce a change in the chirality of the involved quark. For a finite number of these interactions, the number of left- (N_L) and right-handed (N_R) quarks can become unequal, breaking parity symmetry. Global parity conservation however requires that in total chirality is conserved. It is only when a subsection of these interactions are observed that we may find fluctuations. It was realized that a chiral imbalance in combination with the presence of a strong external magnetic field such as expected to be present in heavy ion collisions will result in a chiral and charge current. If the magnetic field is present during the initial phase of the heavy ion collision, including the QGP phase, the magnetic field can orient spins of the quarks along the magnetic field lines, as shown in Figure 1.12. In the event of a vacuum transition to a state with non-zero topological charge, this introduces the presence of a chiral potential $\mu_5 \neq 0$, which can induce the change of a quarks chirality by reversing its momentum.

Using the methods developed for flow as described in the previous chapter, we can also try construct an observable for the electric current along the magnetic field. It has to be considered

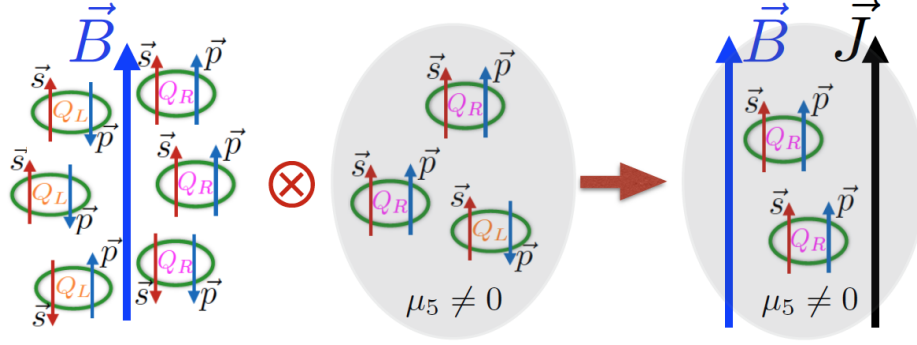


Figure 1.12: Strong magnetic field and non-zero topological charge leading to a charge current called the Chiral Magnetic Effect.

The presence of a strong magnetic field and non-zero topological charge leads to a charge current called the Chiral Magnetic Effect.

that the sign of the non-zero topological charge fluctuates event by event, and as such also the direction of the charge separation. Therefore, to be sensitive to the separation of charges along the magnetic field a \mathcal{P} -even observable is needed. This is the case for one of the main observables for probing the charge separation effect proposed by Voloshin [28]: a two particle correlation relative to the reaction plane,

$$c_{\alpha\beta} = \langle \cos(\varphi_{\alpha} + \varphi_{\beta} - 2\Psi_{RP}) \rangle, \quad (1.16)$$

where φ denotes the azimuthal angle, α, β the electric charges of two correlated particles and Ψ_{RP} the reaction plane angle. The reaction plane, which is defined by the impact-parameter vector and the beam direction, is oriented on average perpendicular to the magnetic field. The angular brackets denote the average over all pairs in all collisions. The parity-even correlation is sensitive to parity-odd symmetry breaking while canceling out background sources independent to the reaction plane. This correlation has been extensively studied at RHIC and LHC [26, 29–31], where a significant charge dependence was observed. The centrality dependence of the charge dependent correlation is shown in Figure 1.13, and in Figure 1.14 the measurement as a function of p_T difference, mean p_T and pseudorapidity difference is shown.

Recently the charge dependent correlation was measured at the STAR beam energy scan [32]. Since the effect of CME is thought to occur principally for a deconfined medium and with chiral symmetry restored, it is interesting to vary energy and consequently the lifetime of the QGP and the magnitude and lifetime of the magnetic field. The results are shown in Figure 1.15.

At the lowest energy the charge separation seems to disappear. With increasing energy the charge separation increases as is in line with expectations.

The interpretation of these results is subject to discussion, because various physical reaction plane dependent sources other than CME are likely to contribute to the observed correlation, like local charge conservation (LCC) and flow fluctuations [33–36]. With LCC, a pair of particles of opposite charge is created close to each other in a similar anisotropic flow field, which results in a symmetry plane dependent correlation between the particles.

Experimentally, LCC is studied using the balance function (BF) introduced in [38]. The balance function measures the correlation strength of balancing partners which is imprinted in the width of the distribution, and can probe through this, the time when the charges hadronized e.g. early versus late stage creation of charges. Recently the ALICE Collaboration reported the

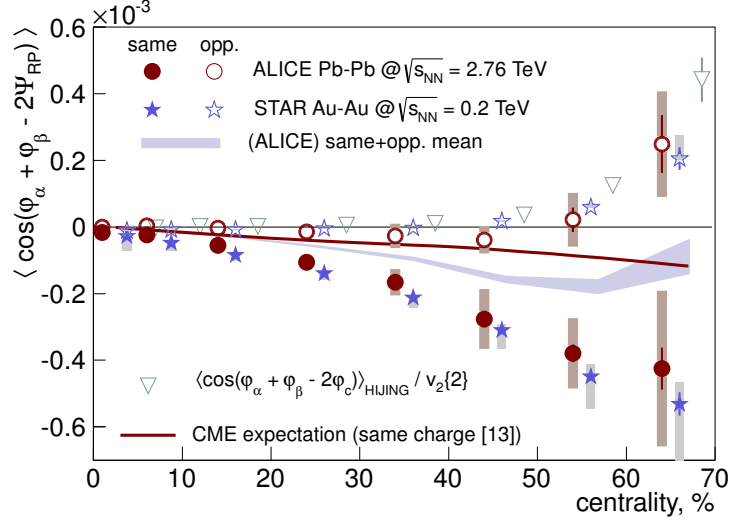


Figure 1.13: The charge dependence of the three-particle correlation $c_{\alpha\beta}$ as a function of centrality with the results from STAR and correlations from HIJING, as well as the CME expectation from STAR extrapolated to LHC energy [30].

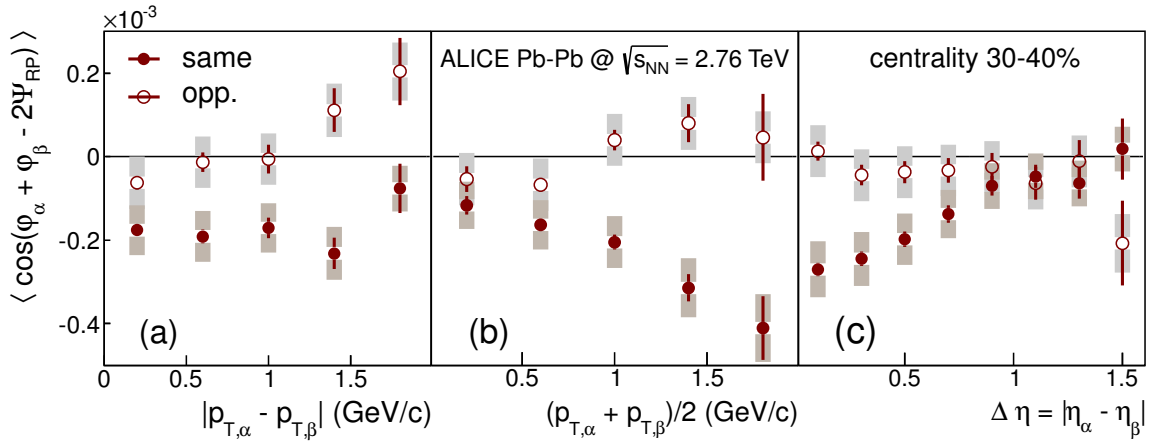


Figure 1.14: The charge dependence of the three-particle correlation $c_{\alpha\beta}$ as a function of p_T difference, mean p_T and pseudorapidity difference [30].

first results on the charge balance functions in Pb–Pb collisions at $\sqrt{s_{NN}} = 2.76$ TeV [39], with the characteristic narrowing of the width for more central collisions in both the relative pseudorapidity ($\Delta\eta$) and azimuthal angle ($\Delta\varphi$). This centrality dependence is qualitatively consistent with the picture of late stage creation of charges, being more correlated for central collisions due to the development of strong radial flow. The shape for the pseudorapidity difference in Figure 1.14 shows the largest signal at a small gap between the particles which decreases towards $\Delta\eta \sim 1$. This shape, indicating the locality of the origin of the correlation, is both expected for LCC and CME. A comprehensive study incorporating BF data in an estimation of the contributions to $\gamma_{\alpha\beta}$ is shown in Figure 1.16. Using a Blast-Wave model and incorporating charge-balancing pairs, the data from STAR can be well described. The individual contributions from LCC to $c_{\alpha\beta}$ originate from having more balancing pairs in-plane than out-of-plane ($v_2\langle c_b \rangle$), stronger correlation in $\Delta\varphi$ for in-plane pairs than the out-of-plane pairs (v_{2c}), and from the balancing charge having a higher probability of being emitted toward the event plane (v_{2s}). Dif-

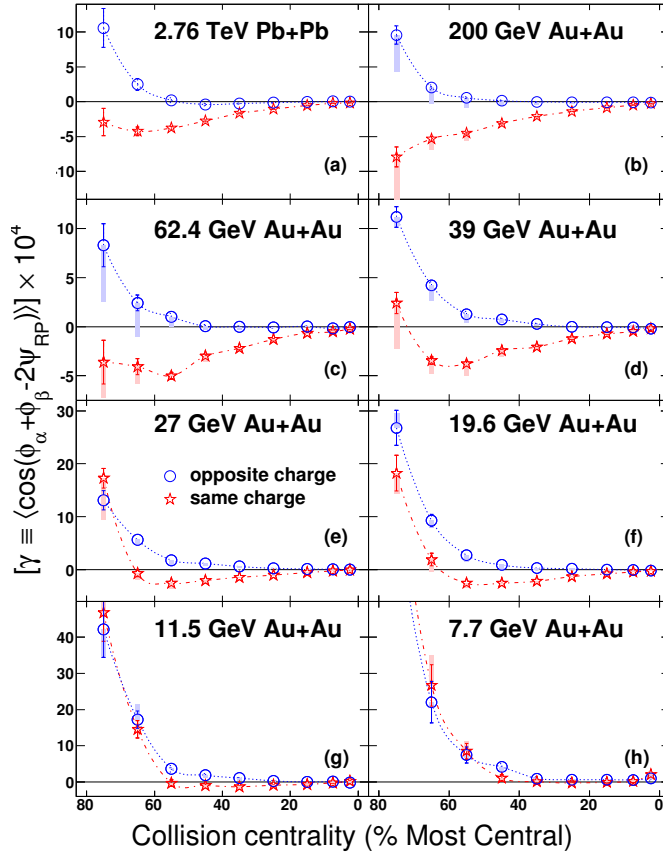


Figure 1.15: Beam energy dependence of the charge dependent correlation [32].

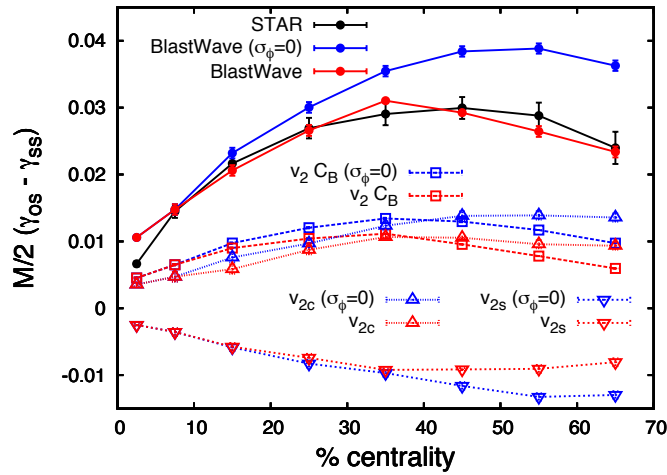


Figure 1.16: Measurement of the charge separation at STAR (Au-Au at $\sqrt{s_{NN}} = 200\text{GeV}$) compared to a Blast-Wave model, where the modulation of charge-balancing pairs by elliptic flow is simulated [37].

ferent values of the width of the distribution of azimuthal angle between the charge-balancing pairs (σ_φ give the same qualitative picture.

Considering the similarity of the CME and other charge dependent signals, it is important to develop not only a qualitative but a quantitative understanding of the contributing sources through additional measurements, which can constrain detailed model calculations.

In the studies presented in this document, additional information about the nature of the charge-dependent correlation is drawn by measuring different moments, as well with the use of identified particles.

2 The ALICE experiment at the LHC

2.1 Large Hadron Collider

The Large Hadron Collider (LHC) at CERN was built to investigate some of most significant questions in physics concerning fundamental matter. Among those were the search for the (since discovered [40, 41]) Higgs boson, and beyond the Standard Model studies like the search for supersymmetric particles. These are the main areas of investigation for the ATLAS and CMS experiments. The focus of the LHCb experiment is the origin of the matter/antimatter asymmetry in the universe through study of b-quarks. Last but not least A Large Ion Collider Experiment (ALICE) is a dedicated heavy ion experiment which aims to clarify the properties of deconfined matter called Quark Gluon Plasma (QGP) which existed in the early stage of the universe, and is created briefly when two heavy ions collide.

The LHC is built in the 26.7 km circular tunnel of the decommissioned LEP collider and several of the large experiments are placed in the caverns of former LEP experiments along the tunnel. The rich history of research with particle accelerators at CERN is visible from the complex of accelerators that form the accelerator complex that provides accelerated particles to the LHC. In the case of the heavy ions, ^{208}Pb atoms are evaporated from a solid source, ionized and sent through LINAC3. From here they pass through LEIR into the PS, from where they follow the same path as accelerated protons for the pp and p-Pb programs coming from LINAC2 and the Proton Synchrotron Booster (PSB). From PS the ions go to the Super Proton Synchrotron (SPS) and are finally injected into the LHC. In the LHC ion beams circulate until they are focussed in several of the experimental caverns, among them ALICE. The energy of the protons and lead ions at the respective stages is shown in Table 2.1.

p		Pb	
Accelerator	Top energy	Accelerator	Top energy
LINAC2	50 MeV	LINAC3	4.2 MeV/u
PSB	1.4 GeV	LEIR	72.2 MeV/u
PS	25 GeV	PS	5.9 MeV/u
SPS	450 GeV	SPS	177 GeV/u
LHC	7 TeV	LHC	5.52 TeV/u

Table 2.1: The accelerator chain with associated energies for protons and lead ions.

2.2 The ALICE experiment

The main goal of the ALICE experiment is to improve our understanding of QCD matter, a state that is achieved briefly in heavy ion collisions. Therefore it is desirable to collect as much information from (the remnants of) collisions as current state of the art technology possibly can

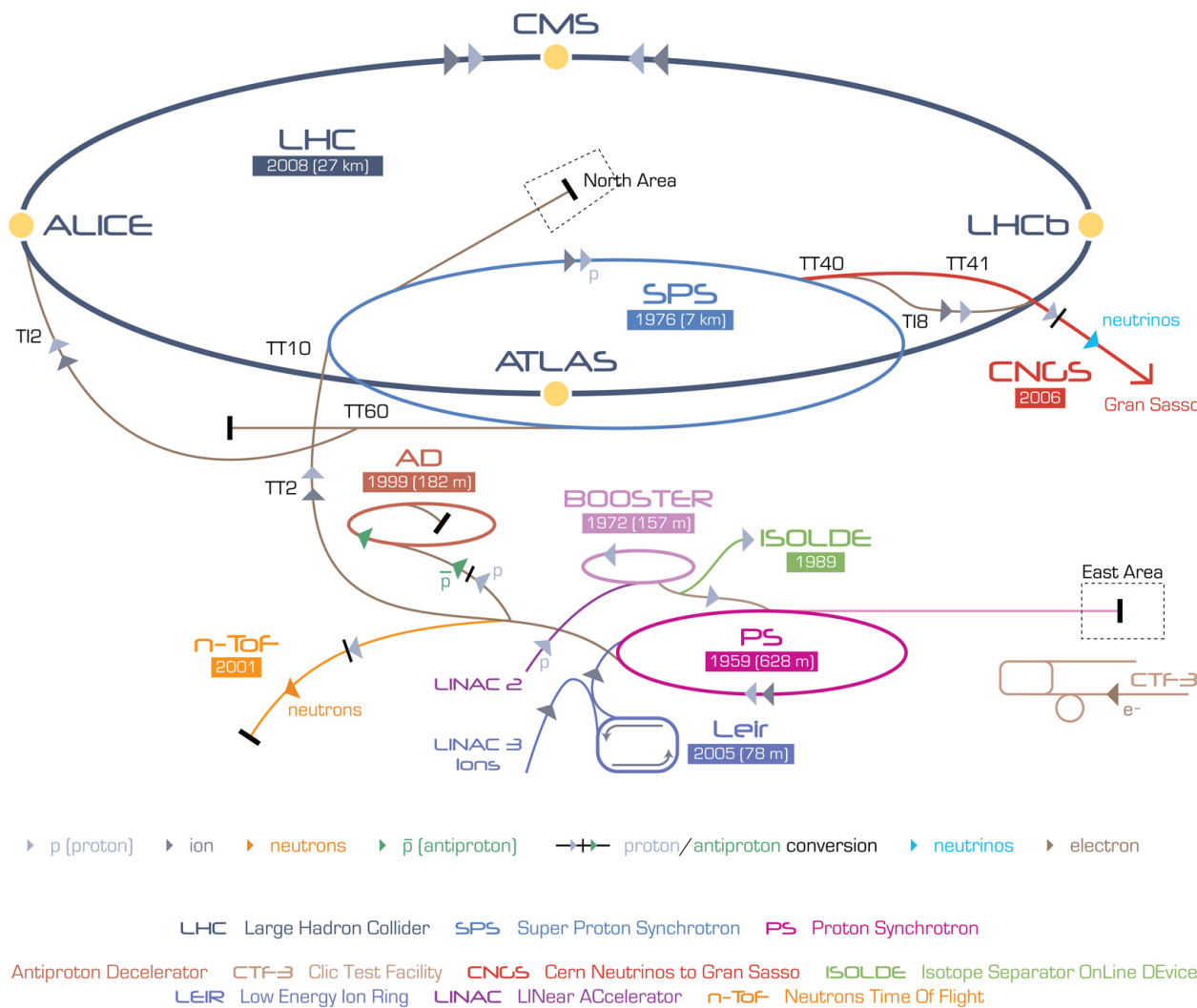


Figure 2.1: The CERN accelerator complex, consisting of the LHC and a chain of pre-accelerators.

allow. This requires recording the properties (momentum, mass, charge, direction) of a diverse range of particles with high precision and acceptance, while detectors and related electronics operate at high speed and in a harsh radiation environment. The ALICE experiment, pictured in Figure 2.2, is such a machine. It consists of an array of subsystems each optimized to cover one or several aspects of the collisions. In total it measures approximately 26 by 16 by 16 meters and weighing 10,000 tons. The backbone of the ALICE detector is the Time Projection Chamber (TPC), which is a gas filled cylinder measuring the path of charged particles passing through the volume. With 4π coverage and high efficiency over a wide p_T -range it is an extremely capable tracking detector and used in most of the physics analyses. Closer to the beam pipe is the Inner Tracking System (ITS), which consists of two layers of Silicon Pixel Detector (SPD), two layers of Silicon Drift Detector (SDD) and two layers of Silicon Strip Detector (SSD). The strength of the ITS lies in very precise vertexing, providing separation power for b quark decays and pile-up rejection. On the outer side of the TPC is the Time-Of-Flight (TOF) detector, which provides a precise time measurement for the particles passing through. In combination with a momentum measurement this gives an estimate of the mass of a particle. Furthermore in midrapidity there is the Transition Radiation Detector (TRD) for electron identification, the High Momentum Particle IDentification detector (HMPID) for particle identification at high momentum, the

Electro-Magnetic CALorimeter (EMCAL) for measurement of jet and neutral particle energies. Several multiplicity detectors are placed at forward rapidity: the V0, the Forward Multiplicity Detector (FMD) and the T0. The V0 and FMD provide multiplicity measurements, and the T0's main purpose is to determine the moment of the collision. On one side of the ALICE detector system dedicated to muons is placed, consisting of an absorber, four muon tracking stations and a muon trigger. Lastly there is a Zero Degree Calorimeter (ZDC) at approximately 115m on both sides of the interaction point that measures spectator fragments. Aside from the ZDC and part of the muon setup all detectors are immersed in a magnetic field of $B = 0.5$ T generated by the L3 solenoid magnet.

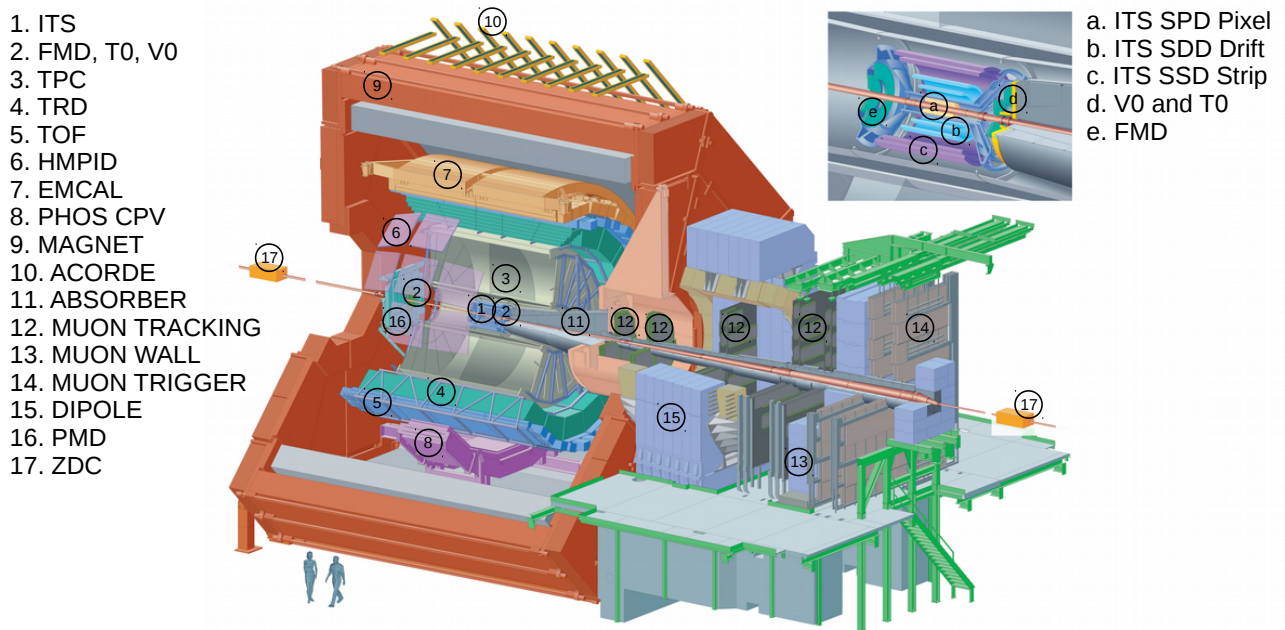


Figure 2.2: The ALICE detector.

2.2.1 Particle tracking and identification

The TPC detector consists of a field cage where the electrons from ionized particles in the gas drift away from the cathode (the central pad planes) and towards the anode at the edges of the TPC. Eighteen sectors divide the read-out for the inner part, the so-called Inner Read-Out Chambers (IROC) of the TPC from 0.8 m to 1.3 m, as well as the outer part of the TPC from 1.3 m to 2.5 m, the Outer Read-Out chambers (OROC). The cathode is operated at 100 kV creating a field gradient of 400 V/cm in the active volume, resulting in a maximum drift time of 100 μ s. The signals from the drifting electrons are collected in multiwire proportional chambers (MWPCs). The electrons first pass a layer of cathode wires that separate the drift from the amplification region. When are close to the anode wires, the electrons are accelerated whereby they start to ionize gas molecules creating an avalanche of electrons, which induce a

signal on the pad plane. The pad plane consists of a series of 159 tangentially oriented readout strips, from where the positions, signal amplitudes and signal times are used to reconstruct 3d tracks and their respective energy loss dE/dx . A gating grid is used to collect the positive ions and prevent the buildup of charges causing distortions in the TPC electric field. The drift time and the closing of the gating grid are components limiting the data taking frequency to approximately 1 kHz, if pile-up is to be avoided. The gas mixture in the TPC has to be chosen to optimize stability, electron/ion drift velocity, high quenching capability (absorption of UV photons created during the electron amplification) and low drift electron absorption. A typical gas mixture contains an inert gas that offers good stability and low electron loss and a gas with good quenching capability. The optimal gas composition depends on the detector and data taking conditions. The choice of gas mixture for the ALICE TPC is 85.7% Ne, 9.5% CO₂ and 4.8% N₂. Some components of the TPC will require a different approach in Run 3 due to the much higher interaction frequency (50 kHz for Pb–Pb). The MWPC's will be replaced by Gas Electron Multiplier (GEM) foils, which amplify the signal from the drifting electrons while limiting the ion back flow. This will allow to operate the TPC in continuous, untriggered readout mode, thereby improving the recordable event frequency by a factor of 100.

The ITS is designed for primary vertex determination with an accuracy below 100 μm , accurate impact parameter measurement for the separation of secondary vertices from D and B mesons, providing energy loss measurements at low p_T and improved momentum measurement by extending the range already covered by the TPC. Because the ITS is placed in front of the other detectors, the material budget is kept to a minimum to avoid multiple scattering and knockout of detector material. However, some presence of material is useful to induce photon conversion for the detection of direct photons using tracks in the TPC. The inner two layers of the ITS, the SPD, are at 3.9 and 7.6 cm from the beam pipe and extend 24.5 cm in z -direction. There are a total of 1200 readout chips with 8192 pixels each measuring 50 μm ($r\phi$) \times 425 μm (z), providing the precision that is required to handle the high track densities at this distance from the primary vertex. The SDD has two layers at 15 and 23.9 cm extending 44.4 and 59.4 cm along the z -direction consisting of 260 modules with silicon drift technology. The SSD consists of two layers at 38 and 43 cm extending 86.2 and 97.8 cm along the z -direction with a total of 1698 modules, each with 1536 silicon sensor strips. The outer four layers of the ITS measure position and energy loss dE/dx . By fitting hits between the two layers, constructing so-called tracklets, the primary vertex can be determined with high precision. The second set of two layers, the SDD, is used to measure the energy loss dE/dx .

Track reconstruction

The main track reconstruction includes information from TPC, ITS and is used to match signals in other detectors. The reconstruction is done through a three stage procedure, going inward, outward and back again. In the first step seeds are created in the TPC. These are built from 2 TPC clusters and the vertex, followed by a fit to 3 TPC clusters without the vertex. From this point, TPC clusters are added in an inward direction if they are close enough to the track. The algorithm allows cluster sharing between multiple tracks. Afterwards, tracks that share a certain amount of clusters are filtered to one track based on the quality of the track. The tracks are corrected for energy loss in detector material while assuming a preliminary particle identification based on dE/dx information.

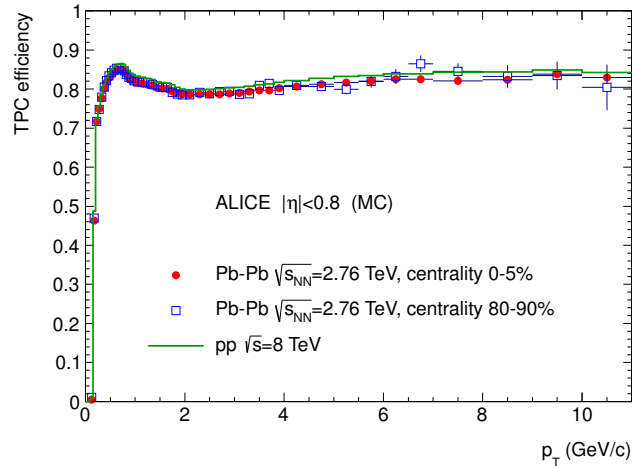


Figure 2.3: Tracking efficiency in the TPC for different detector occupancy using simulations.

In Figure 2.3, using simulations the tracking efficiency in the TPC is shown as a function of the transverse momentum. Three different scenarios, pp, peripheral Pb–Pb and central Pb–Pb show that the tracking efficiency is largely independent of detector occupancy. The turn-on curve results from energy loss in detector material, while at dip around 2 GeV/c results from the relatively longer fraction particles can spend in the dead zone between TPC sectors.

The TPC tracks are extrapolated to the outer ITS layer where they are matched to hit and further propagated inward similar to the procedure within the TPC. The fitting procedure allows for missing clusters in layers of the ITS. Afterwards the tracks are again cleared from large amounts of cluster sharing. An ITS standalone fitting procedure is also applied to unmatched clusters, which leads to a high reconstruction efficiency for low momentum particles down to 80 MeV/c. At this point tracks are extrapolated to the distance of closest approach, from where the tracks are fitted in the outwards direction, finding matches in the TOF and with TRD tracklets, as well as signals in EMCal, PHOS and HMPID. Finally the tracks are refitted starting the propagation from the outer radius of the TPC using clusters associated in the previous fitting and updated for information on the position, curvature, energy loss and the covariance matrix. The combined fit using information from TPC+ITS delivers the most accurate determination of track parameters. However, due to holes in the ITS acceptance in the 2010 data taking period, it can also be preferable for analyses requiring good uniform acceptance to use TPC tracks. An alternative option is to fill 'missing' TPC+ITS tracks with TPC standalone tracks. In this case the track type is called 'hybrid'.

Particle identification

The ALICE detector has several subsystems with different characteristics that contribute to the capability for the identification of particles. ITS, TPC and HMPID measure energy loss of charged hadrons (also light nuclei) as well as electrons. The TOF can identify the same group of particles by measuring the arrival time of a particle, which determines the mass if the moment of the collision and the particles momentum is known. Further identification with a focus on separating electrons from pions and protons is provided by the TRD through a measurement of both energy loss and the emission of transition radiation by electrons. The EMCal can identify protons, neutrons, electrons and photons through the measurement of energy deposited, shower shape

analysis and time-of-flight information. While electrons and photons are typically stopped in the EMCal, hadrons mostly pass through. The fraction of energy deposited to the particle momentum provides a way to separate the two groups of particles. The presence or absence of a matched track in the TPC provides the charge information. The PHOS photon spectrometer dedicated to the measurement of photons works on the same principles as the EMCal but has improved photon identification and a smaller acceptance. Lastly muons are simply ‘identified’ by placing a thick absorber in front of the muon tracking stations, blocking all particles except muons from passing through.

TPC

The main detectors for particle identification of the most common charged hadrons (pions, kaons, protons) at intermediate p_T are the TPC and the TOF.

Charged particles traversing the volume of the TPC mostly lose energy through collisions with the electrons in the gas molecules. The energy loss for heavy particles at relativistic speeds ($0.1 \lesssim \beta\gamma \lesssim 1000$) follows the Bethe equation, which describes the mean rate of energy loss for heavy charged particles,

$$-\langle dE/dx \rangle = Kz^2 \frac{Z}{A} \frac{1}{\beta^2} \left[\frac{1}{2} \ln \frac{2m_e c^2 \beta^2 \gamma^2 T_{\max}}{I^2} - \beta^2 - \frac{\delta(\beta\gamma)}{2} \right]. \quad (2.1)$$

Here A is the atomic mass number, $\frac{K}{A} = 4\pi N_A r_e^2 m_e c^2 / A$ with N_A Avogadro’s number, r_e and m_e the classical electron radius and mass, further Z is the atomic number of the absorber, I the mean excitation energy, T_{\max} the maximum energy transfer in a single collision, and $\delta(\beta\gamma)$ a density effect correction.

The description of the mean energy loss is in fact not a very practical one, since fluctuations on a per collision basis can be large. The ALICE TPC can retrieve a maximum of 159 charged clusters related to a given track in the MWPCs, of which the pulse height is proportional to the ionization strength. A truncated mean is taken to estimate the dE/dx , which can be determined with a resolution of 5%. For the purpose of particle identification a parametrization of the Bethe formula is applied to the detector measurement,

$$f(\beta\gamma) = \frac{P_1}{\beta^{P_4}} \left(P_2 - \beta^{P_4} - \ln \left(P_3 + \frac{1}{(\beta\gamma)^{P_5}} \right) \right), \quad (2.2)$$

where $P_{1..5}$ are fit parameters. The top left panel of Figure 2.4 shows the dE/dx measured in the TPC as a function of momentum. The lines are the parametrizations of dE/dx for the various particle species. The position of a dE/dx measurement relative to one of the parametrizations in combination with knowledge of the width of the distribution around a parametrization can be used to calculate the probability for a certain particle identity.

TOF

The purpose of the Time Of Flight detector is to measure the arrival time of particles with high precision. The detector consists of Multigap Resistive Plate Chambers (MRPCs), which are built from 11 sheets of thin glass with narrow gas filled gaps with in high electric field in between.

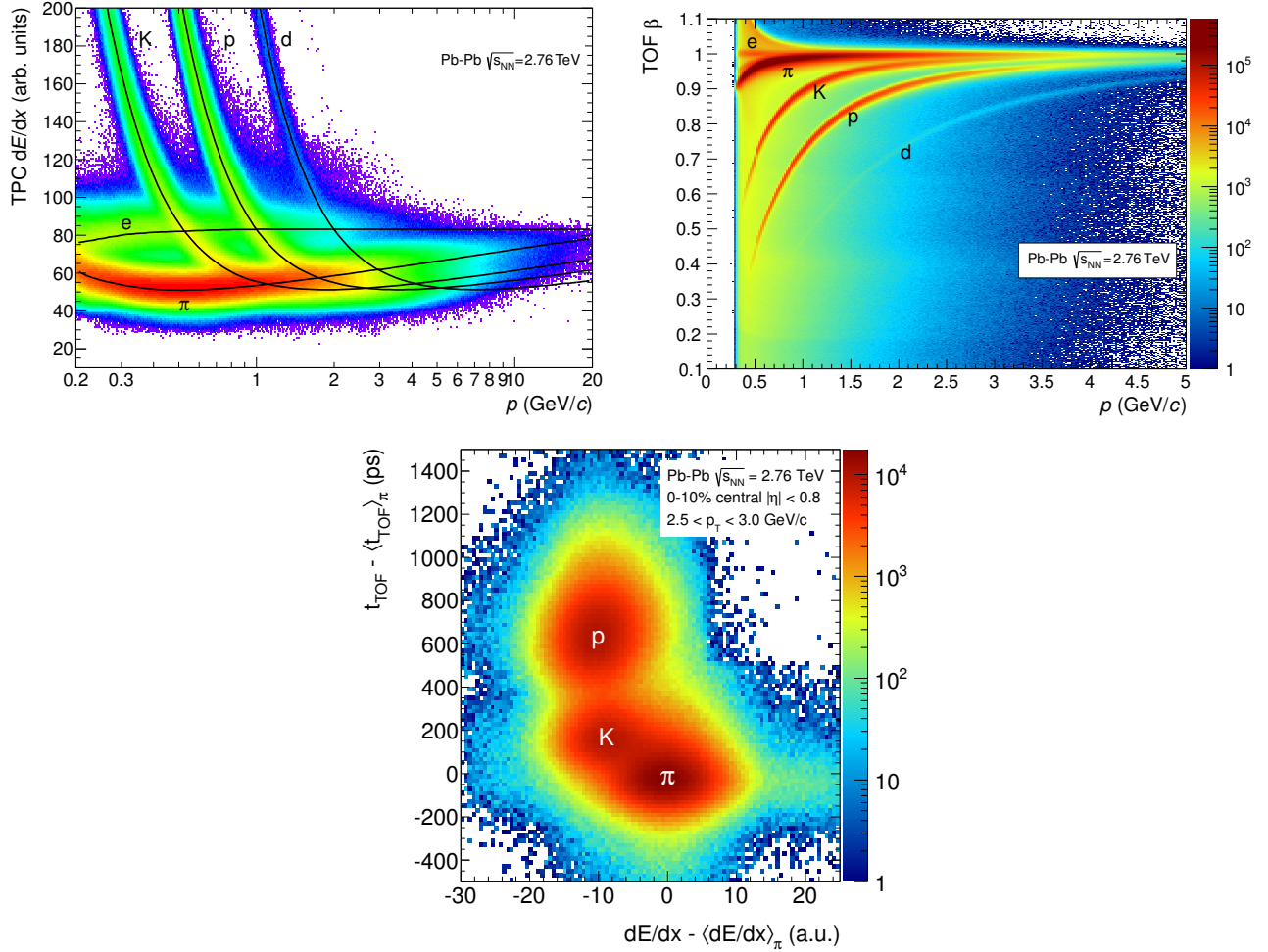


Figure 2.4: Energy loss in TPC (left) and velocity measurement with TOF (right) as a function of particle momentum [42]. Data from the two detectors combined improves the separation power for particle identification (bottom) [43].

The timing resolution of the TOF is approximately 80 ps. The start time is provided by the T0 detector which is described in Section 2.2.2. Due to the small acceptance of the T0, it does not always provide a start time measurement. In these cases it is necessary to estimate the start time using assumptions on the mass of the arriving particles.

The momentum of a particle, which is needed to calculate the velocity, is provided by a matched track in the TPC. The top right panel of Figure 2.4 shows the β measurement of particles in Pb–Pb collisions. Good separation is achieved for pions, kaons and protons in the region up to 2.5 GeV/c for pions and kaons, and up to 4 GeV/c for protons.

Bayesian particle identification

Particle identification measurements from different detectors can be combined to fully utilize the identification capabilities of the ALICE detector as a whole [43]. The bottom panel of Figure 2.4 shows the correlation between the dE/dx and β measurement for particles in a momentum range of $2.5 < p_T < 3.0$ GeV/c in central events. It is visible that the combined information gives better separation between particle types than having only a projection on either the x -

or y -axis. One procedure for the utilization of information from both detectors is to calculate Bayesian probabilities for a particle to be associated to a specific particle type. The conditional probability to measure a signal S for particle type H_i is denoted as $P(S|H)$. $P(S|H)$ is obtained by parametrizing the response of a detector to different particle species. For a range of detectors, the combined probability is the product

$$P(\vec{S}|H_i) = \prod_{\alpha=\text{TPC,TOF},\dots} P_\alpha(S_\alpha|H_i), \quad (2.3)$$

with $\vec{S} = (S_{\text{TPC}}, S_{\text{TOF}}, \dots)$.

With knowledge of the a priori probability to detect a certain particle $C(H_i)$ (a prior), the probability to detect a certain particle type for measured detector signals using Bayes' theorem is

$$P(H_i|\vec{S}) = \frac{P(\vec{S}|H_i)C(H_i)}{\sum_{k=e,\mu,\pi,\dots} P(\vec{S}|H_k)C(H_k)}. \quad (2.4)$$

The priors are determined with an iterative procedure starting with a value of 1 for all species and then measuring the relative abundances of particles for the priors in the next iteration [43]. The Bayesian probability is a convenient tool to select the desired purity in a sample of identified particles and is used for the selection of identified particles in Chapter 4.

2.2.2 Forward detectors

The ALICE detector has three systems in the forward region that measure produced particle (and secondary particle) multiplicities: the T0, V0 and FMD. In addition there is a calorimeter positioned at the beam axis to measure spectator fragments.

T0

The T0 detector measures Cherenkov radiation and consists of two arrays of 12 quartz radiators with photo multiplier tubes (PMTs) at $-3.28 < \eta < -2.97$ and $4.61 < \eta < 4.92$. The measurement with the T0 provides the timing of the collision and is used for the β measurement with the TOF. In addition the timing difference between the T0-A and T0-C can be used to estimate the interaction point and to reject pile-up or satellite collisions. The T0 can also be used as a trigger. The uniform placement of the T0 and the multiplicity measurement also makes it useful for the estimation of the reaction plane (see Section 3), although the sensitivity is low due to the small acceptance.

V0

The V0 detector has 32 segments divided in 4 azimuthally uniform rings (each with 8 sectors) with equal rapidity coverage on each side of the interaction point. The sectors contain scintillator tiles that are read out with optical fibres. The V0-C covers a pseudorapidity region of $-5.1 < \eta < -2.8$ and V0-A $1.7 < \eta < 3.7$. The azimuthal segmentation of the detector makes it

useful for symmetry plane estimation especially up the third flow harmonic. The sensitivity to higher harmonics decreases due to the limited granularity.

FMD

The FMD detector consists of 5 subsystems equipped with narrow silicon strips. The coverage partly overlaps with that of the V0: the FMD-C is from $-3.4 < \eta < -1.7$ and FMD-A $1.7 < \eta < 5.0$. Three subsystems contain 20 strips oriented azimuthally symmetric and radially outward from the beam axis. Two of subsystems have 40 strips with similar orientation. The FMD detectors also have fine granularity in η , in total providing 152000 individual multiplicity measurements. Between the FMD and the interaction point is a considerable amount of material which leads to large amounts of secondaries in the detector, requiring detailed filtering. The FMD detector is used to measure forward spectra and because of its uniformity, large acceptance and high granularity is a very capable detector for flow studies.

ZDC

The ZDC-A and ZDC-C is dedicated to the measurement of spectator protons, neutrons and fragments traveling along the beam axis after the nuclei from which they originate interacted inelastically. The geometry is a square, and each side is equipped with a tungsten-quartz neutron and a brass-quartz proton calorimeter. The readout is divided into 4 quadrants, offering limited sensitivity to the azimuthal distribution of spectators, mainly useful for the first flow harmonic.

2.2.3 Triggers

The LHC offers a high rate of crossing bunches. It is impossible for ALICE in terms of detector read-out speed and disk volume to record fully each collision. Depending on the physics interests different triggers are designed to collect data from specific detectors at specific rates. These include a Minimum Bias (MB) trigger, high multiplicity triggers, EMCal triggers, muon triggers and others. Most of the triggers are designed to use the full capabilities of the ALICE detector, while the for example the fast muon trigger can collect data at a high rate that excludes use of the TPC. While signals from the detectors are temporarily stored, triggers have to make fast decisions about whether or not to record an event. Triggers consist of several levels labeled L0-2 and the High Level Trigger system (HLT). Every machine clock cycle of approximately 25 ns. the Central Trigger Processor takes input from the different detector systems. The L0 decision is made after $0.9 \mu\text{s}$ based on data from V0, T0, EMCal, PHOS and a muon trigger detector (MTR). The events passing L0 go to L1 which takes a decision after $\sim 6.5 \mu\text{s}$ after processing of EMCal, TRD and ZDC data. A positive decision from L2 results in the readout of data from the detectors to the front-end electronics with a latency of $\sim 300 \text{ ns}$. After 100 ms, L2 may determine whether an event contains pile-up and decides whether to send data to the DAQ and the HLT. The HLT processes and reconstructs data from all available detectors to make a trigger decision and in addition the HLT compresses event data without loss of relevant physics information.

2.2.4 Event characterization

A heavy ion collision consists of several stages, from initial state to final state. Although we can't experimentally control the initial state (other than by the choice of ions), we can extract information about initial configuration of matter density from the particles in the final state, which are measured in the detector. The main quantities that can be obtained are the centrality, which is related to the impact parameter, and the flow vectors, which contain information on the shape of the overlap area.

Centrality

The impact parameter of heavy ion collisions can be estimated through the produced particle multiplicities or spectator multiplicities. The first step is to divide the multiplicity measurement in so-called centrality bins, which then can be related to a certain number of binary collisions and impact parameter. Because the last step is not model independent, experimental results are often reported for ranges of centrality. The centralities measured using charged particles and spectator fragments are defined experimentally as

$$c \approx \frac{1}{N_{\text{ev}}} \int_{N_c}^{\infty} \frac{dn}{dN'_c} dN'_c \approx \frac{1}{N_{\text{ev}}} \int_0^{E_{\text{ZDC}}} \frac{dn}{dE'_{\text{ZDC}}} dE'_{\text{ZDC}}. \quad (2.5)$$

The number of tracks N_c increases monotonically with centrality, while the number of spectators decreases towards more central events. Above 50% centrality, the fragments end up outside the ZDC acceptance, limiting the applicability of the ZDC energy (E_{ZDC}) measurement to more central events. N_{ev} is the number of events (corrected for trigger efficiency).

The left panel of Figure 2.5 shows the measurement of the total V0 multiplicity for a sample of Pb–Pb minimum bias events. The data is fitted with a parametrization based on the Glauber model. The Glauber model can be used to calculate the number of binary collisions N_{coll} based on the nuclear density profile and the assumption that particles follow straight lines and collide with one another with a likelihood according to the nucleon-nucleon cross section. The parametrization is $f N_{\text{part}} + (1 - f) N_{\text{coll}}$, where a fraction of collisions f represents the soft particle distribution, and every source produces a number particles according to a negative binomial distribution (NBD) which has two parameters. The fit is used to relate the measured centrality to N_{coll} and N_{part} .

The right panel of Figure 2.5 shows the determination of the ZDC centrality up to 30%, where the different colors represent the corresponding centralities as determined with the V0.

Symmetry planes

The symmetry planes are also determined from produced particles or spectator fragments and carry information on the initial distribution of nuclear matter, as previously described in Section 1.7.1. The ALICE detector has a range of detectors with good azimuthal coverage and therefore sensitivity to the anisotropic emission of particles. Before expanding on the topic in Chapter 3, a short overview is presented of the sensitivity of various ALICE subsystems to particle flow. The resolution correction factor (Equation 3.3) for various detector subsystems is shown in Figure 2.6.

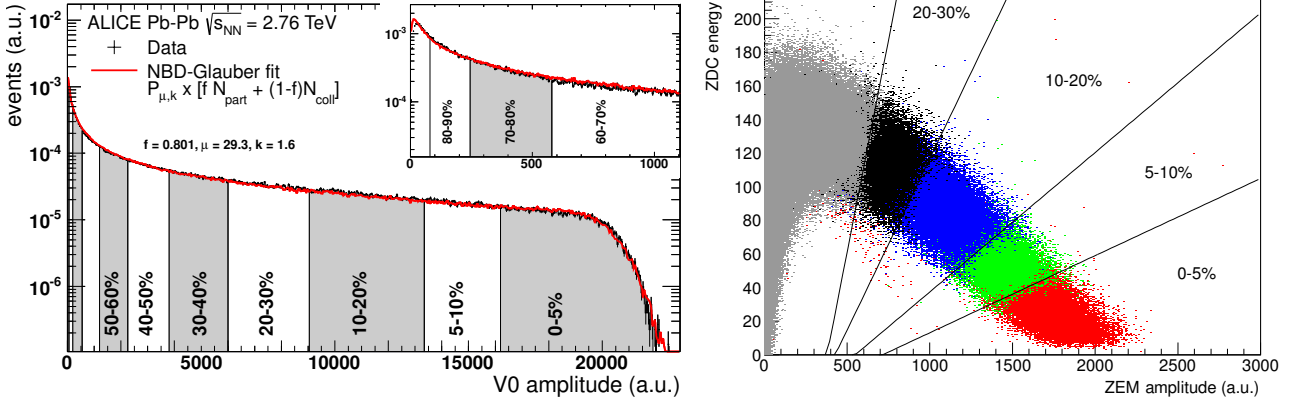


Figure 2.5: Centrality estimation using V0 multiplicity (left) and ZDC energy (right).

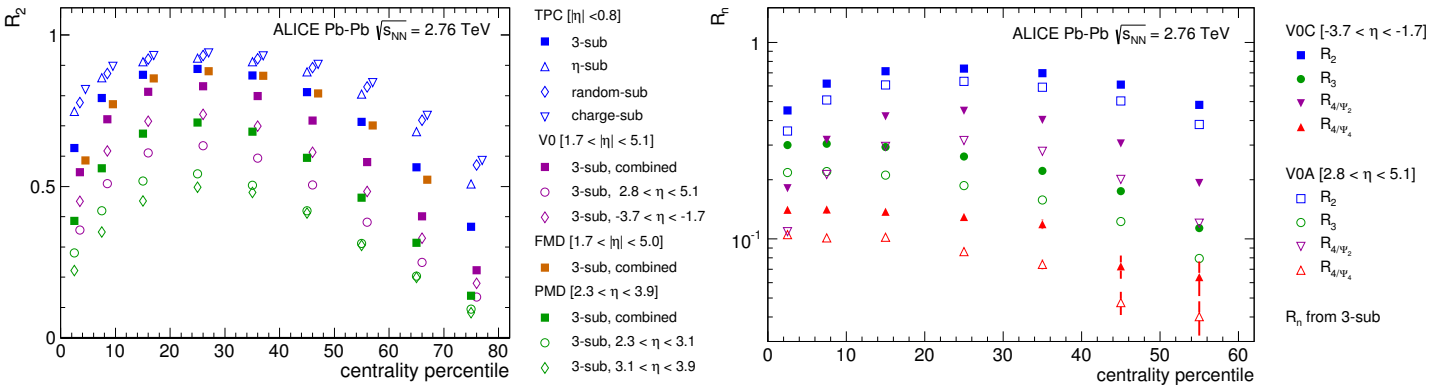


Figure 2.6: The resolution correction factor for symmetry plane estimation with the TPC, V0, FMD and PMD detectors for second harmonic (left) and with V0 detector for up to fourth harmonic (right).

Event shape engineering

The flow vectors are not only useful for the determination of collision symmetry planes, but carry even more detailed information on the configuration of the colliding nucleons. Hydrodynamic models indicate that the measured v_2 is closely correlated to the initial eccentricity (ϵ_2). This means we can use an event-by-event measurement of the particle anisotropy to select on the eccentricity of the initial matter distribution. This technique is called event-shape-engineering (ESE)[44]. In ESE events are classified using the reduced q -vector (Q/\sqrt{M}), which removes trivial multiplicity dependence from Q . These terms are explained in the next chapter.

Figure 2.7 shows that the magnitude of q_2 (left panel) and v_2 (right panel) are correlated, demonstrating that the q_2 vector can effectively be used to select on event shape.

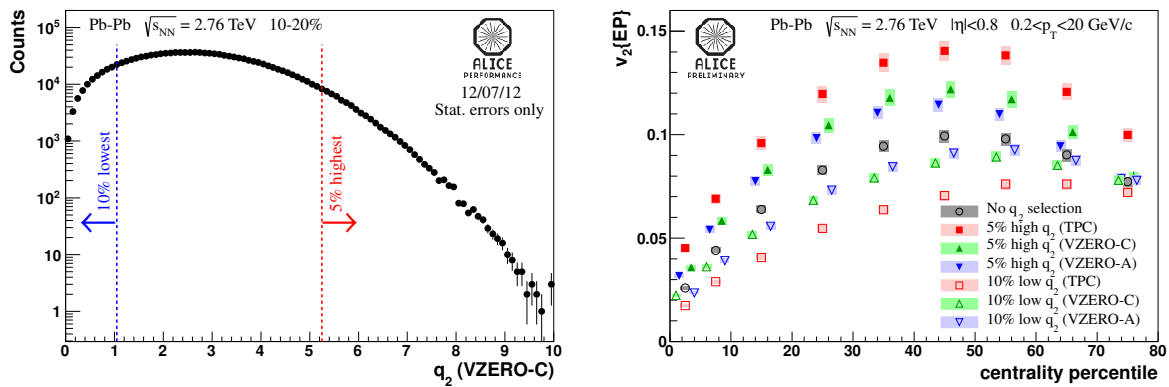


Figure 2.7: Measurement and selection of q_2 with the V0-A detector (left) and its impact on the measurement of v_2 (right) [45].

3 Anisotropic flow methods and flow vector corrections

3.1 Flow methods

Several methods have been developed to measure collectivity in heavy ion collisions through correlations of particle azimuthal angles. Correlations between particles measured in the final state can reveal information about the initial state and the evolution of the collision system. One of the common parameters that characterize the collectivity is the Fourier decomposition of the single particle distribution introduced in Equation 1.7. In addition to measuring the flow harmonic coefficients v_n , correlations between flow magnitudes and symmetry plane angles can also be studied [46, 47]. Event shape engineering, which is the selection on event shape, is a useful tool to determine event classes based on their shape and was briefly described in Section 2.2.4. In this chapter, we focus on the use of Q -vectors in flow measurements. For the corrections of non-azimuthal detector acceptance a software package was developed and results with ALICE data are presented.

3.1.1 The Q -vector

The Fourier decomposition in Equation 1.7 contains an experimentally inaccessible parameter, the symmetry plane Ψ_{SP} . An estimation of the orientation this plane can be deduced from the anisotropic distribution of particles. This is done by constructing a so-called flow vector, or Q -vector,

$$Q_{n,(x,y)} = \sum_{i=0}^M e^{in\varphi_i} = \sum_{i=0}^M (\cos n\varphi_i, \sin n\varphi_i), \quad (3.1)$$

which is constructed from M particles with azimuthal angles φ , and n corresponds to the flow harmonic. The flow vector will give the average direction of particles for a given harmonic.

3.1.2 Event plane method

Due to the finite number M , only an estimate can be made of the true symmetry plane. This estimate is called the event plane (Ψ_{EP}) is calculated from the Q -vector

$$\Psi_{EP} = \frac{1}{n} \text{atan2}(Q_{n,y}, Q_{n,x}). \quad (3.2)$$

How well Ψ_{EP} coincides with Ψ_{SP} is quantified by the resolution parameter R , which scales with the number of particles M and the magnitude of the flow, $R \approx v_n \sqrt{M}$. R itself can be

measured by splitting the observed particles in three independent subevents and measuring the three sets of two-subevent correlations over many events.

$$R^{(n),A} = \cos(\Psi_{EP}^{(n)A} - \Psi_{SP}^{(n)}) = \sqrt{\frac{\langle \cos(\Psi_{EP}^{(n)A} - \Psi_{EP}^{(n)B}) \rangle \langle \cos(\Psi_{EP}^{(n)A} - \Psi_{EP}^{(n)C}) \rangle}{\langle \cos(\Psi_{EP}^{(n)B} - \Psi_{EP}^{(n)C}) \rangle}} \quad (3.3)$$

With the event plane and the resolution parameter, the Fourier coefficients in Equation 1.7 can be calculated with the event plane method,

$$v_n = \langle \langle \cos n(\varphi - \Psi_{SP}^{(n)}) \rangle \rangle = \frac{1}{R_n} \langle \langle \cos n(\varphi - \Psi_{EP}^{(n)}) \rangle \rangle. \quad (3.4)$$

It was described in [48] that the event plane method has differing sensitivity to event-by-event fluctuations in v_n . For $R \approx 1$, the observed $\langle v_n \rangle$ coincides with v_n , while for $R \ll 1$, we obtain $\sqrt{\langle v_n^2 \rangle}$.

When the ϕ and Ψ_{EP} are measured in the same rapidity window, the correlation is also sensitive to nonflow, i.e. the correlation between particles unrelated to the common symmetry plane. This can occur when particles are correlated at production like in jets or decays. Due to the nature of nonflow, it can be suppressed by correlating particles from different pseudo-rapidity regions.

3.1.3 Scalar product method

The ambivalence of the event plane method can be avoided with the scalar product method, which is similar to the event plane method but removes the $Q/|Q|$ normalization of the Q -vector, instead normalizing by M or \sqrt{M} . This method consistently measures $\sqrt{\langle v_n^2 \rangle}$.

3.1.4 Cumulant method

The Fourier coefficients can also be estimated with particle cumulants:

$$c_n = \langle \langle e^{in(\varphi_i - \varphi_j)} \rangle \rangle, \quad (3.5)$$

where $i \neq j$ in the correlation of particles. The two-particle cumulant is related to the flow coefficient as $v_n = \sqrt{c_n}$. Non-flow in the two particle cumulant can be suppressed by imposing a rapidity gap between the particles. Another way to suppress nonflow is by measuring multiparticle correlations, for example the four particle cumulant which is given by

$$c_n = \langle \langle e^{in(\varphi_i - \varphi_j + \varphi_k - \varphi_l)} \rangle \rangle, \quad (3.6)$$

which is related to flow with

$$v_n = \sqrt{-c_4 - c_2^2}. \quad (3.7)$$

The four particle cumulant removes two particle nonflow and suppresses further nonflow by an additional $1/M^2$ factor [49]. It does however, require a much larger statistical sample. The

fluctuating initial energy density also causes fluctuations of the event-by-event magnitude of flow, even for a fixed impact parameter. If these fluctuations (σ_v) are assumed to be Gaussian-shaped and small compared to the flow ($\sigma_v \ll \langle v \rangle$), the cumulants measure

$$v_2\{2\}^2 = v_0^2 + 2\sigma_n^2, \quad (3.8)$$

$$v_2\{n\} = v_0, n \geq 4. \quad (3.9)$$

The difference between the measurements of the two observables is visible on the right side of Figure 1.8. More details about cumulants can be found in [49, 50].

The correlation techniques described in this section are not only useful for the determination of the flow harmonics, or correlations among them, but also for other effects that may depend on the symmetry plane orientation. One such example, the main subject of this document, is discussed in the next chapter.

3.2 Q-vector corrections

The Q-vector which is used for observables which aim to distinguish between different initial state configurations measures the anisotropy of particles created in the collision, or of spectator fragments. In an ideal case, the only limiting factor to relate the Q to a symmetry plane is number of charged particles measured, which depends on the number of particles produced and the placement and acceptance of a detector. Also a certain amount of flow has to be present. However, detector imperfections may introduce biases in the measurement of the Q-vector, which have to be accounted for. In this section the different steps are discussed that are needed to correct for detectors with non-uniform acceptance.

3.2.1 Recentering, diagonalization and rescaling

Effects of non-uniform acceptance of detectors in the measurement of anisotropic flow have been described in [51]. The relation between the participant plane Ψ_{pp} and its measured unit vector components can be expressed as

$$\langle x_n \rangle_{\Psi_{SP}} = \bar{x}_n + v_n a_{2n}^+ (\cos n\Psi_{SP} + \lambda_{2n}^{s+} \sin n\Psi_{SP}), \quad (3.10)$$

$$\langle y_n \rangle_{\Psi_{SP}} = \bar{y}_n + v_n a_{2n}^- (\sin n\Psi_{SP} + \lambda_{2n}^{s-} \cos n\Psi_{SP}), \quad (3.11)$$

where the acceptance coefficient a_{2n}^\pm is defined as

$$a_{2n}^\pm = 1 \pm \bar{x}_{2n}, \quad (3.12)$$

and the smallness parameter as

$$\lambda_{m \mp n}^{c \pm} = \frac{v_m}{v_n} \frac{\bar{x}_{m \pm n}}{a_{2n}^\pm}. \quad (3.13)$$

Non-azimuthal effects can then be corrected for by inverting the equation and applying three consecutive corrections:

Shift of the u_n -vector:

$$x'_n = x_n - \bar{x}_n, \quad y'_n = y_n - \bar{y}_n, \quad (3.14)$$

twist of the u_n -vector

$$x_n'' = \frac{x' - \lambda_{2n}^{s-} y'}{1 - \lambda_{2n}^{s-} \lambda_{2n}^{s+}}, \quad y_n'' = \frac{y' - \lambda_{2n}^{s+} x'}{1 - \lambda_{2n}^{s-} \lambda_{2n}^{s+}}, \quad (3.15)$$

and rescaling of u_n -vector

$$x_n''' = \frac{x_n}{a_{2n}^+}, \quad y_n''' = \frac{y_n}{a_{2n}^-}, \quad (3.16)$$

where \bar{c}_n is the shorthand notation for $\cos n\phi$ (similarly we introduce $\bar{s}_n = \sin n\phi$).

Similar to Equation 3.10 the relation between the event vector

$$Q_n = \sum_{EP} u_n = \sum_{EP} (\cos n\phi + i \sin n\phi), \quad (3.17)$$

and the symmetry plane Ψ_{SP} can be expressed as

$$\langle X_n \rangle = \bar{X}_n + A_{2n}^+ (\cos n\Psi_{SP} + \Lambda_{2n}^{s+} \sin n\Psi_{SP}), \quad (3.18)$$

$$\langle Y_n \rangle = \bar{Y}_n + A_{2n}^- (\sin n\Psi_{SP} + \Lambda_{2n}^{s-} \cos n\Psi_{SP}). \quad (3.19)$$

The correction parameters A_{2n} and Λ_{2n} can be extracted similarly to Equation 3.12-3.13. In certain cases the double harmonic required for extraction of the correction parameters is unavailable because of limited granularity of the detectors. In this event the acceptance and smallness parameters can be extracted using two random subevents as in [51] or with three subevents (α, β, γ). In the latter case we have the following coupled equations (only one permutation shown):

$$2\langle X_n^\alpha X_n^\beta \rangle = A_{2n}^{\alpha,+} A_{2n}^{\beta,+} (1 + \Lambda_{2n}^{\alpha,s+} \Lambda_{2n}^{\beta,s+}), \quad (3.20)$$

$$2\langle Y_n^\alpha Y_n^\beta \rangle = A_{2n}^{\alpha,-} A_{2n}^{\beta,-} (1 + \Lambda_{2n}^{\alpha,s-} \Lambda_{2n}^{\beta,s-}), \quad (3.21)$$

$$2\langle X_n^\alpha Y_n^\beta \rangle = A_{2n}^{\alpha,+} A_{2n}^{\beta,-} (\Lambda_{2n}^{\alpha,s+} + \Lambda_{2n}^{\beta,s-}), \quad (3.22)$$

$$2\langle Y_n^\alpha X_n^\beta \rangle = A_{2n}^{\alpha,-} A_{2n}^{\beta,+} (\Lambda_{2n}^{\alpha,s-} + \Lambda_{2n}^{\beta,s+}). \quad (3.23)$$

In addition symmetry requires

$$A_{2n}^+ \Lambda_{2n}^{s+} = A_{2n}^- \Lambda_{2n}^{s-}. \quad (3.24)$$

In total there are 12 coupled equations ((α, β) plus the permutations of (α, γ) and (β, γ)) with 3 symmetry constraints. There are 12 unknowns ($3 \times A_{2n}^\pm, \Lambda_{2n}^\pm$), thus this system is closed and presumably solvable.

3.2.2 Misalignment

The correction procedure described above assumes perfect knowledge of the azimuthal angle φ associated to a signal. In reality, the placement of a detector may have a shift with respect to the expected position, or non-azimuthal acceptance within a detector segment may shift the angle that should be associated to the measured signal. The shift of the actual coordinate of a signal with respect to the ascribed coordinate can have a radial and azimuthal component. A radial shift is in fact accounted for with the recentering, diagonalization and scaling procedure described in the previous section. However an azimuthal component will alter the measurement of the symmetry plane ($\Psi \rightarrow \Psi + \Delta\phi$). An angular offset $\Delta\phi_{\alpha,\beta}$ between two detectors (α, β) will modify measured correlations as follows

$$\langle X_n^\alpha X_n^\beta \rangle_M = \langle X_n^\alpha X_n^\beta \rangle \cos n\Delta\phi_{\alpha,\beta} - \langle X_n^\alpha Y_n^\beta \rangle \sin n\Delta\phi_{\alpha,\beta}, \quad (3.25)$$

$$\langle Y_n^\alpha Y_n^\beta \rangle_M = \langle Y_n^\alpha Y_n^\beta \rangle \cos n\Delta\phi_{\alpha,\beta} + \langle Y_n^\alpha X_n^\beta \rangle \sin n\Delta\phi_{\alpha,\beta}, \quad (3.26)$$

$$\langle X_n^\alpha Y_n^\beta \rangle_M = \langle X_n^\alpha Y_n^\beta \rangle \cos n\Delta\phi_{\alpha,\beta} + \langle X_n^\alpha X_n^\beta \rangle \sin n\Delta\phi_{\alpha,\beta}, \quad (3.27)$$

$$\langle Y_n^\alpha X_n^\beta \rangle_M = \langle Y_n^\alpha X_n^\beta \rangle \cos n\Delta\phi_{\alpha,\beta} - \langle Y_n^\alpha Y_n^\beta \rangle \sin n\Delta\phi_{\alpha,\beta}. \quad (3.28)$$

We can not solve this system and determine $\Delta\phi_{\alpha,\beta}$ without considering acceptance effects in the detector correlations. Combined with Equations 3.20-3.23 we can again write the equations as a function of the acceptance and smallness parameters. For a system with three detectors there are 15 unknowns ($3x A_{2n}^\pm, \Lambda_{2n}^{s\pm} + 3x \Delta\phi$). With permutations of Equations 3.25-3.28 there are 12 coupled equations and 3 symmetry constraints, which brings us to a total of 15 equations. Thus also this system is closed.

3.2.3 Extraction of correction parameters for diagonalization and rescaling

Solving the equations described above can be difficult in the general case, but is greatly simplified in some specific cases. One can find the parameters to correct for twist and rescaling corrections with the stand-alone method (Equations 3.12 and 3.13) as long as the azimuthal granularity is sufficient for a reliable measurement in the x and y directions for double the harmonic of interest, and when there are significant correlations to be measured (Eq. 3.20-3.23). In practice this requires at least a number of segments $N_s \geq 2n$.

If a detector β fulfills above requirements, and assuming azimuthal misalignment is uniform, we can correct for non-uniform azimuthal acceptance with the stand-alone method and then align other detectors α and γ to this detector. For a fully corrected detector $A_{2n}^+ = A_{2n}^- = A_{2n}$ and $\Lambda_{2n}^{s\pm} = 0$. Equations 3.20-3.23 then become

$$2\langle X_n^\alpha X_n^\beta \rangle = A_{2n}^{\alpha,+} A_{2n}^\beta, \quad (3.29)$$

$$2\langle Y_n^\alpha Y_n^\beta \rangle = A_{2n}^{\alpha,-} A_{2n}^\beta, \quad (3.30)$$

$$2\langle X_n^\alpha Y_n^\beta \rangle = A_{2n}^{\alpha,+} A_{2n}^\beta \Lambda_{2n}^{\alpha,s+}, \quad (3.31)$$

$$2\langle Y_n^\alpha X_n^\beta \rangle = A_{2n}^{\alpha,-} A_{2n}^\beta \Lambda_{2n}^{\alpha,s-}. \quad (3.32)$$

From the symmetry constraint of Equation 3.24 we can now see that for aligned systems $\langle X_n^\alpha Y_n^\beta \rangle = \langle Y_n^\alpha X_n^\beta \rangle$ and we rewrite Equations 3.25-3.28 to

$$\langle X_n^\alpha X_n^\beta \rangle_M = \langle X_n^\alpha X_n^\beta \rangle \cos n\Delta\phi_{\alpha,\beta} - \langle X_n^\alpha Y_n^\beta \rangle \sin n\Delta\phi_{\alpha,\beta}, \quad (3.33)$$

$$\langle Y_n^\alpha Y_n^\beta \rangle_M = \langle Y_n^\alpha Y_n^\beta \rangle \cos n\Delta\phi_{\alpha,\beta} + \langle X_n^\alpha Y_n^\beta \rangle \sin n\Delta\phi_{\alpha,\beta}, \quad (3.34)$$

$$\langle X_n^\alpha Y_n^\beta \rangle_M = \langle X_n^\alpha Y_n^\beta \rangle \cos n\Delta\phi_{\alpha,\beta} + \langle X_n^\alpha X_n^\beta \rangle \sin n\Delta\phi_{\alpha,\beta}, \quad (3.35)$$

$$\langle Y_n^\alpha X_n^\beta \rangle_M = \langle X_n^\alpha Y_n^\beta \rangle \cos n\Delta\phi_{\alpha,\beta} - \langle Y_n^\alpha Y_n^\beta \rangle \sin n\Delta\phi_{\alpha,\beta}. \quad (3.36)$$

The azimuthal shift can now be determined without considering non-uniform azimuthal acceptance in subevents α and γ :

$$\tan n\Delta\phi_{\alpha,\beta} = \frac{\langle X_n^\alpha Y_n^\beta \rangle_M - \langle Y_n^\alpha X_n^\beta \rangle_M}{\langle X_n^\alpha X_n^\beta \rangle_M + \langle Y_n^\alpha Y_n^\beta \rangle_M}. \quad (3.37)$$

If α and/or γ are constructed with a sectorized detector, we can also determine the azimuthal angle of the individual sectors by correlating them separately to β . For one sector we can write

$$\langle X_n^{\alpha 1} Y_n^\beta \rangle = \cos \phi_{\alpha 1} \langle M_1 X_n^\beta \rangle, \quad (3.38)$$

$$\langle Y_n^{\alpha 1} X_n^\beta \rangle = \sin \phi_{\alpha 1} \langle M_1 Y_n^\beta \rangle. \quad (3.39)$$

Since $\langle X_n^\alpha Y_n^\beta \rangle = \langle Y_n^\alpha X_n^\beta \rangle$, we get

$$\tan n\phi_{\alpha 1,\beta} = \frac{\langle M_1 X_n^\beta \rangle}{\langle M_1 Y_n^\beta \rangle}. \quad (3.40)$$

Since the solution to $\phi_{\alpha 1,\beta}$ has a period of π/n , approximate knowledge of the azimuthal placement of $\alpha 1$ is required to determine its actual position.

One example solution to Equations 3.29-3.31 (including the permutations and symmetry constraints) is given by

$$\Lambda_{2n}^{\alpha,s+} = \frac{\langle X_n^\alpha Y_n^\beta \rangle}{\langle X_n^\alpha X_n^\beta \rangle}, \quad \Lambda_{2n}^{\alpha,s-} = \frac{\langle X_n^\alpha Y_n^\beta \rangle}{\langle Y_n^\alpha Y_n^\beta \rangle}, \quad (3.41)$$

$$\Lambda_{2n}^{\gamma,s+} = \frac{\langle X_n^\gamma Y_n^\beta \rangle}{\langle X_n^\gamma X_n^\beta \rangle}, \quad \Lambda_{2n}^{\gamma,s-} = \frac{\langle X_n^\gamma Y_n^\beta \rangle}{\langle Y_n^\gamma Y_n^\beta \rangle}, \quad (3.42)$$

$$A_{2n}^{\alpha,+} = \frac{\sqrt{2\langle X_n^\alpha Y_n^\beta \rangle \langle X_n^\alpha X_n^\beta \rangle}}{\sqrt{\langle X_n^\alpha X_n^\beta \rangle \langle X_n^\gamma Y_n^\beta \rangle + \langle X_n^\alpha Y_n^\beta \rangle \langle Y_n^\gamma Y_n^\beta \rangle}}, \quad A_{2n}^{\alpha,-} = \frac{A_{2n}^{\alpha,+} \Lambda_{2n}^{\alpha,s+}}{\Lambda_{2n}^{\alpha,s-}}, \quad (3.43)$$

$$A_{2n}^{\gamma,+} = \frac{\sqrt{2\langle X_n^\alpha Y_n^\beta \rangle \langle X_n^\gamma X_n^\beta \rangle}}{\sqrt{\langle X_n^\alpha X_n^\beta \rangle \langle X_n^\gamma Y_n^\beta \rangle + \langle X_n^\alpha Y_n^\beta \rangle \langle Y_n^\gamma Y_n^\beta \rangle}}, \quad A_{2n}^{\gamma,-} = \frac{A_{2n}^{\gamma,+} \Lambda_{2n}^{\gamma,s+}}{\Lambda_{2n}^{\gamma,s-}}. \quad (3.44)$$

It is clear that the above solutions are only valid if the measurement of the correlations significantly differ from 0. When Equation 3.40 is first used to remove angular shifts from the subevents then $\langle X_n^\alpha X_n^\beta \rangle_M = \langle X_n^\alpha X_n^\beta \rangle$ etc, we can now apply twist and scaling corrections to subevents α and γ for a fully corrected measurement of the event vectors.

3.2.4 Gain equalization

A multiplicity detector is usually segmented and collects ionization electrons, or transition or Cherenkov photons. Typically the signals are amplified, for example with a PMT. The individual segments may function at different efficiencies and amplification may not be uniform. Or due to material budget in front of the detector the signal received is not uniform. The non-uniformity of the recorded signal may also depend on the occupancy or the location with respect to the primary vertex. With a gain equalization procedure applied for different event classes these effects can be, at least partially, mitigated.

One method is to divide the signal $M_{c,i}$ of each detector segment c measured for event i :

$$M'_{c,i} = \frac{M_{c,i}}{\langle M_c \rangle}. \quad (3.45)$$

where $\langle M_c \rangle$ is an average over events in a given event class.

$$\langle M_c \rangle = \frac{1}{N_{ev}} \sum_i^{N_{ev}} M_{c,i}. \quad (3.46)$$

Here N_{ev} is a number of events.

Alternatively a correction can be applied that includes width equalization of the multiplicity distribution for each segment:

$$M'_{c,i} = A + B \frac{M_{c,i} - \langle M_c \rangle}{\sigma_{M_c}}. \quad (3.47)$$

where A and B in Eq. (3.47) are free parameters which are the same for all channels. A and B are chosen to make an easier visual comparison with distributions resulting from Eq. (3.45). σ_{M_c} is the standard deviation of the multiplicity distribution

$$\sigma_{M_c} = \sqrt{\frac{1}{N_{ev}} \sum_i^{N_{ev}} M_{c,i}^2 - \frac{1}{N_{ev}^2} \left(\sum_i^{N_{ev}} M_{c,i} \right)^2}. \quad (3.48)$$

3.3 Implementation of correction procedure

For the rest of this chapter, we assume a detector setup with the following characteristics: presence of one tracking detector and two segmented, hit-based multiplicity detectors. This setup is typical of many heavy-ion physics experiments such as ALICE and STAR. From the corrections presented in the previous section we established the following sequence of flow vector corrections:

-
1. Gain equalization of individual detector channels
 2. Recentering
 3. Alignment
 4. Twist
 5. Rescaling

3.3.1 Software package *FlowVectorCorrections*

A correction framework based on ROOT [52] was developed together with Ilya Selyuzhenkov and Victor Gonzalez and is publicly available in [53]. Although developed for ALICE, the framework was specifically designed to be applicable to data from other experiments. The input for the framework is generally angles and weights, and the output is corrected Q -vectors. The definition of the Q -vector and the corrections that are applied depend on the user configuration. A brief overview of main concepts in the object-oriented framework is given here.

Configuration

The configuration object provides the user with handles for determining the settings used in the correction framework. The main settings are

- Definition of Q -vector: standard Q , Q/M , Q/\sqrt{M} , $Q/|Q|$
- Harmonics of interest
- Event classes based on event parameters
- Corrections to be applied
- Optional: track/channel selection

Input data

The main input for the framework is the azimuthal angle ϕ and relevant weight w from detector measurements. Track properties can also be provided in case a track selection is provided in the Configuration. Detector information can be associated to ID numbers to create subsets of the input data to build Q -vectors. From the input data Q -vectors are constructed for each Configuration object that the user defined.

Q -vectors

The Q -vector objects carry a range of information. Beyond the Q -vector components for the harmonics defined in the Configuration, the object retains information about the number of elements M , the sum of weights W , a flag that tracks the applied corrections and a flag for the definition of the Q -vector. The relevant class also contains functions to calculate the event plane or the vector length.

Event classes

Corrections may have to be applied in different event classes in order to avoid biases within the data sample. The user can define event parameters and the appropriate binning in the Configuration. The event information for these parameters has to be passed to the framework. The information relevant to the corrections is collected in multidimensional histograms where each bin represents an event class. The user has to ensure that a statistically significant number of events is present in each event class to ensure the accurate determination of the required corrections.

Corrections

The data passes through the set of corrections that the user determined in the Configuration. The structure of the framework allows for development of new corrections that can be added to the framework without disrupting its internal structure. The correction parameters are retrieved from correction histograms. Quality assurance (QA) histograms are filled on demand to monitor the performance of the corrections.

Output

The output from the framework contains the Q -vectors defined in the Configuration. The full Q -vector information is available from each correction step, such that the user has access to results from the entire pipeline. The framework also produces correction and QA histograms.

Operation of the framework

The user should provide a set of Configurations to an instance of the framework. The framework is then run while feeding the relevant event-by-event information. The framework identifies the corrections that have to be applied and the number of passes that are required to extract the correction parameters and apply the corrections. The correction parameters are stored in histograms and the output of one iteration serves as input for the next. After the number of required passes are applied, the user has access to the corrected Q -vectors.

3.4 Toy Monte Carlo study

To demonstrate the functionality of the framework for a specific combination of subevents and detector non-uniformities a simple Monte-Carlo routine is employed. Particles for three subevents A , B , and C are generated with $\nu_1 = 0.2$ and respective multiplicities 50, 200, and 50. In the simulation, subevent B consists of an ideal tracker, while subevent A and C are radially segmented in 16 equal parts. From simulated angles after detector acceptance the $\langle \nu_1 \rangle = \langle \cos(\varphi^B - \Psi_{EP}^A) \rangle / R_1^A$ is extracted where the resolution correction R_1^A is calculated using the 3-subevent method (Eq. 3.3). The azimuthal acceptance of A , B and C is represented by the disks in Fig. 3.1. Case 1 (triangle up) demonstrates the gain equalization, where for A and C four segments have 50% of the ideal gain (which mimics four miscalibrated channels). Case 2

(triangle down) demonstrates recentering, where two orthogonal segments are disabled. Case 3 (star) demonstrates the alignment correction. Here the subevents A and C have uniform acceptance, but the coordinate systems are rotated by $\pi/8$ to mimic misalignment. Case 4 (diamond) and 5 (cross) have gaps that maximize the twist and rescaling corrections respectively. However, these non-uniformities don't affect our observable and the corrections don't change the result. Case 6 is a superposition of cases 1-5. In all cases 1-6 the input value of ν_1 is accurately reconstructed. Limitations for the applicability of the corrections and the impact of multiplicity correlations are currently being studied.

The blue disks inside Figure 3.1 show the non-uniformity of the subevents.

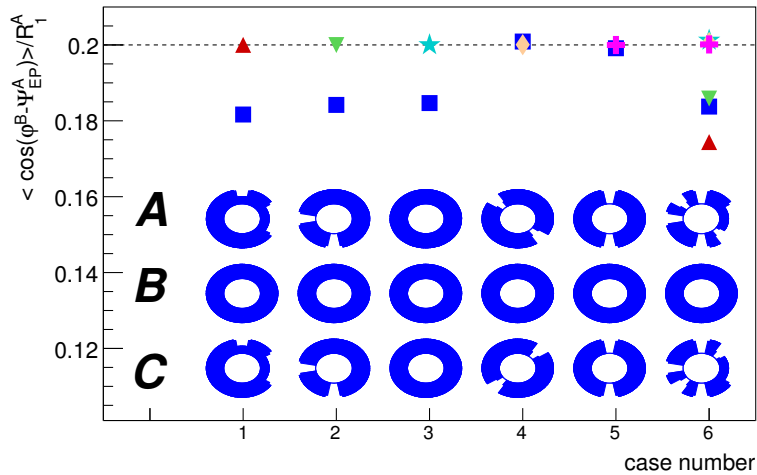


Figure 3.1: Estimates of input ν_1 (dashed line) from simulated azimuthal angle distributions before (blue squares) and after different corrections (other markers) [54].

3.5 Corrections with ALICE data

The application of the corrections to data was studied with a Minimum Bias data sample of 13M Pb–Pb collisions at $\sqrt{s_{NN}} = 2.76$ TeV recorded with the ALICE detector in 2010. Details on event and track selections are in Section 4.3.

This section describes separately each step of the event plane calibration procedure for the detectors TPC, V0, T0 and FMD.

Corrections are applied for the reduced two dimensional q -vector

$$q_{2,i} = (q_{2,x}, q_{2,y}) = \frac{Q_{2,i}}{M_i} = \frac{1}{M_i} \sum_c^{N_c} M_{c,i} u_{2,i} \quad (3.49)$$

where ϕ_c , N_c , $M_i = \sum_c^{N_c} M_{c,i}$ is an azimuthal angle of a segment (track), number of sectors (unity), and the total signal (number of tracks) measured in a given multiplicity (tracking) detector. In case of the TPC $M_{c,i} = 1$. A second harmonic unity vector $u_{2,i}$ is defined as

$$u_{2,i} = (u_{2,x}, u_{2,y}) = (\cos 2\phi_c, \sin 2\phi_c). \quad (3.50)$$

A full calibration of the q requires 2 passes over data for the TPC, and 4 passes for the other detectors. The corrections applied to data are detailed in the next sections.

3.5.1 Signal equalization

For channel equalization event classes are divided into 100 equal bins in V0 centrality and 10 bins in the event z -vertex position.

Gain equalization was only applied for channels of the V0 and T0 detectors. No additional calibration was applied for the FMD detector channels, for which an extensive correction procedure that accounts for charge sharing and secondaries is already applied within the ALIROOT framework [55].

V0 and T0

The V0 consists of two circular detectors on A- and C-side, each divided into 8 ϕ -segments and 4 η -segments, totalling a total of 64 readout signals. The T0 consists of two circular detectors on A- and C-side, each equipped with 12 PMT's for the readout.

Despite the azimuthal symmetric distribution of channels, the readout signal does not necessarily reflect this symmetry. Possible causes for this are different sector efficiencies, unequal signal amplification, or different amounts of secondaries due to fluctuating material budget, among others. The channel equalization procedure aims to symmetrize the multiplicity measurement from the different detector segments.

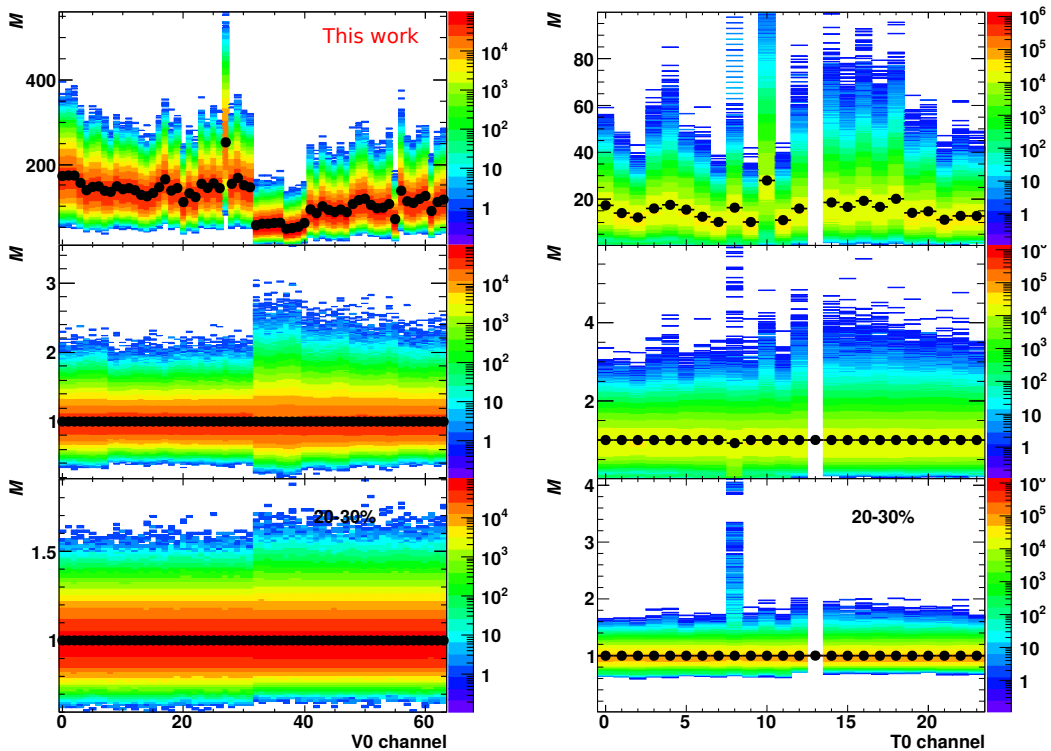


Figure 3.2: Left column: Multiplicity distribution for V0 channels in 10-20% V0 centrality. The top figure shows the distribution for raw multiplicity, the middle figure for multiplicity equalized channels, and the bottom figure with an additional width equalization. Right column: similar as left column, for T0.

Figure 3.2 shows the multiplicity distribution for the V0 and T0 detector channels for the 10-20% centrality range. The raw multiplicity distributions in the top figures show an uneven distribution of the multiplicity. It is also visible that the signal in several channels (27 for V0, 8 and 13 for T0) are outliers. The middle figures show the multiplicity distribution with signal equalization applied, by dividing by the average signal in the channel. The bottom figures show the equalized signal with the additional width equalization procedure applied. It is visible that for V0, the channels show a very similar distribution after the equalization procedures. For the T0, the signal for channel 8 and 13 does not reflect the same distribution as for the other T0 channels. This reflects the non-Gaussian response of the raw measurement. Such channels are probably better excluded for flow measurements, as is done in this document.

Figure 3.3 shows the multiplicity measurement for one channel of the V0 and T0 detectors in different stages of the signal equalization. As is the nature of the correction procedure, the shape of the signal is not strongly modified.

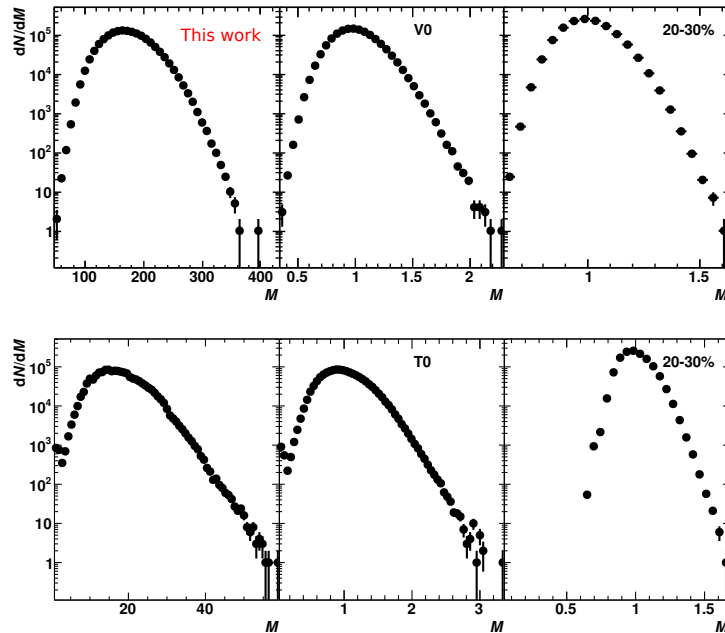


Figure 3.3: Top row: Multiplicity distribution for channel 0 of the V0 detector in 10-20% V0 centrality. The left figure shows the raw multiplicity, the middle figure the equalized multiplicity, and the right figure the multiplicity with the additional width equalization applied. Bottom row: similar as top row, for T0 channel 0.

The gain equalization has already an effect on the measurement of the mean q as is shown in Figure 3.4 and 3.5 for V0-C and T0-C. For T0-C, the y-component shows that the equalization procedure restores the symmetry in the measurement of the Q-vector distribution. For central events, the recentering procedure will have minimal effect. For more peripheral events where some of the channels become empty, the distribution will be off-center due to certain channels having more sensitivity to low multiplicity events.

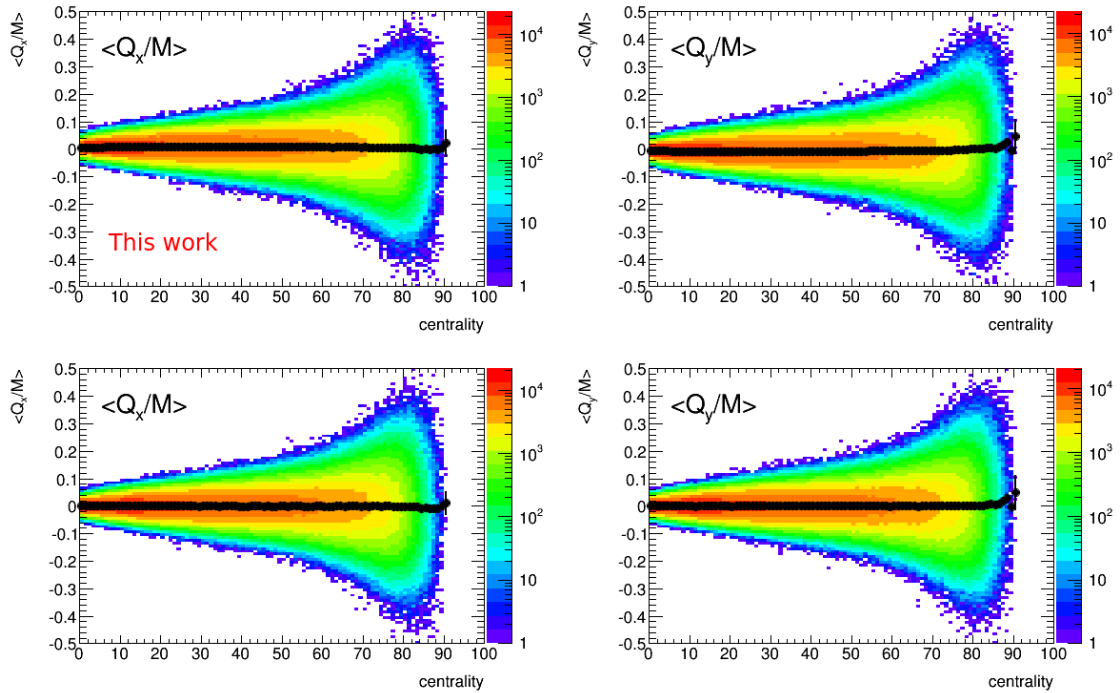


Figure 3.4: V0-C q before (top) and after (bottom) channel gain equalization. The left plots are for the x- and the right plots for the y-component of q.

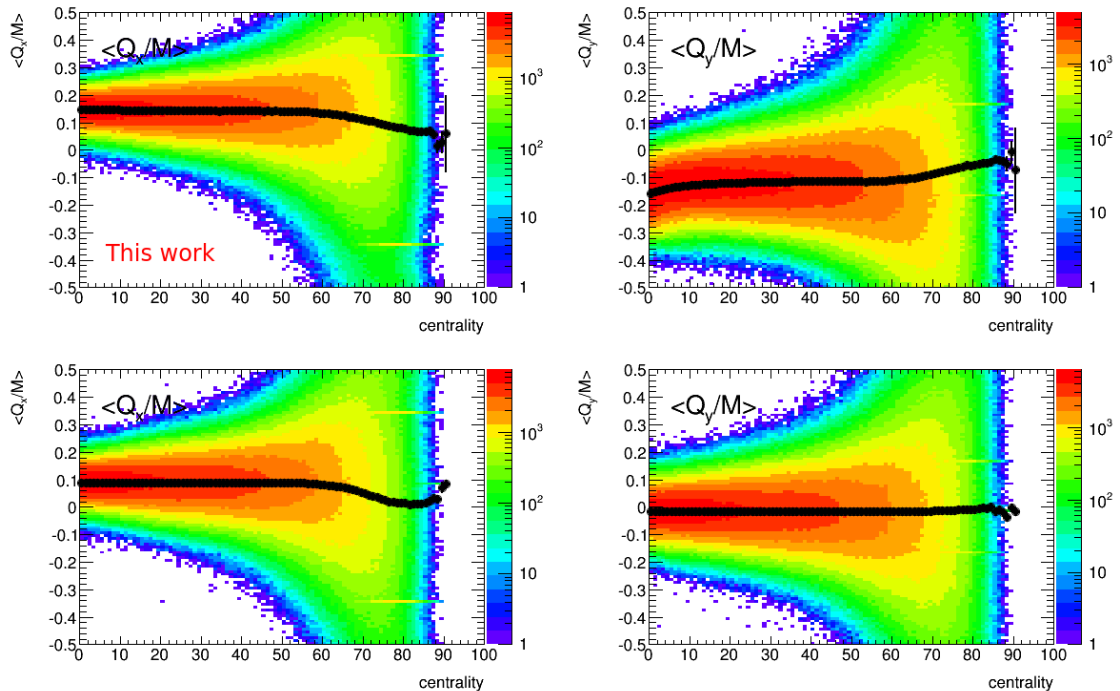


Figure 3.5: T0-C q before (top) and after (bottom) channel gain equalization. The left plots are for the x- and the right plots for the y-component of q.

FMD

The FMD channel measurements are corrected through an advanced procedure which accounts for hits from secondary particles due to detector material as well as multiple hits from overlap-

ping strips of different detector segments. The related correction procedure is described in more detail in [56].

3.5.2 Q-vector recentering

The recentering procedure (Eq. 3.14) ensures that the mean of the reconstructed Q -vectors is equal to zero, and is the first step suggested in [51]. The mean of Q/M (q) was extracted in 100 equal bins of centrality and 10 variable bins of event z -vertex.

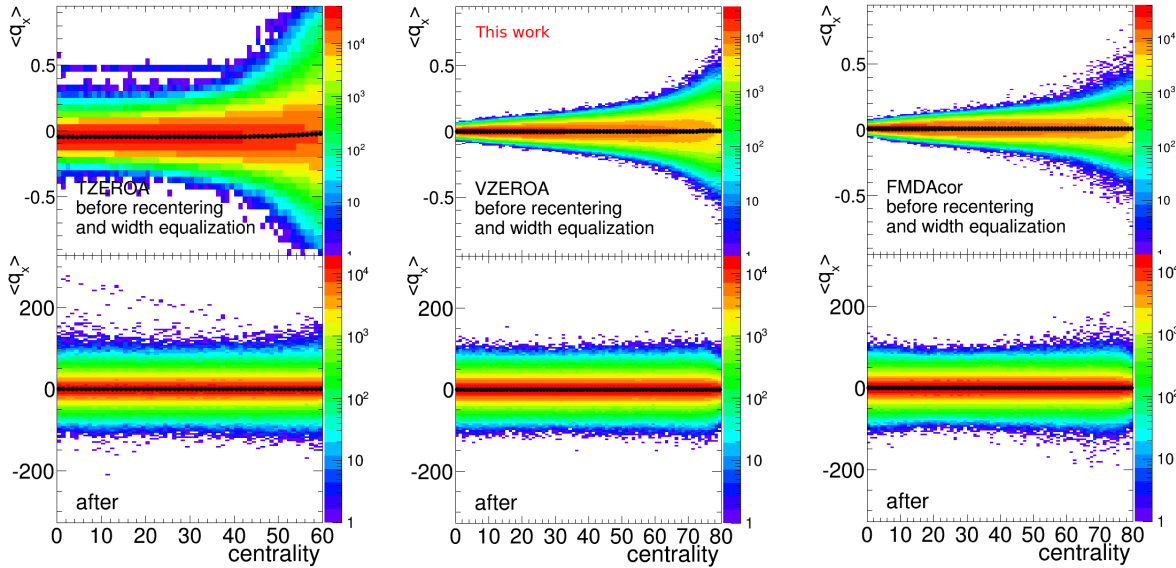


Figure 3.6: T0-A (left), V0-A (middle) and FMD-A (right) Q/M measurement before (top) and after (bottom) channel recentering. All plots are for the x -component of the Q -vector.

Figure 3.6 shows the effect of the recentering procedure for x -component of the Q -vector measured with the T0, V0 and FMD detector. The upper panel shows the distribution before recentering, and the lower panel after recentering. Additionally to a subtraction of the mean, the Q -vectors were divided by the standard deviation of the distribution. This procedure can be used to enforce a similar distribution of Q -vectors for events with varying multiplicity, but is not a correction to the Q -vector per se. Above 60% centrality the T0 width equalization becomes ineffective (not shown). This is probably related to the non-Gaussian distribution of the Q -vector in peripheral events, due to quantization of the Q -vector which results from only a few channels having a multiplicity measurement (see also Figure 3.12).

3.5.3 Q-vector alignment

Alignment of a Q -vector is a correction for the rotation of the vector, present due to detector effects or an offset between the assigned angle associated to a detector signal and its actual placement. The offset can be measured with two subevent correlations according to Equation 3.37.

An significant offset was observed in the outer ring of the V0 detector. The correlation of the Q -vector components of the V0-C ring 4 and the TPC is shown in Figure 3.7. Before the rotation,

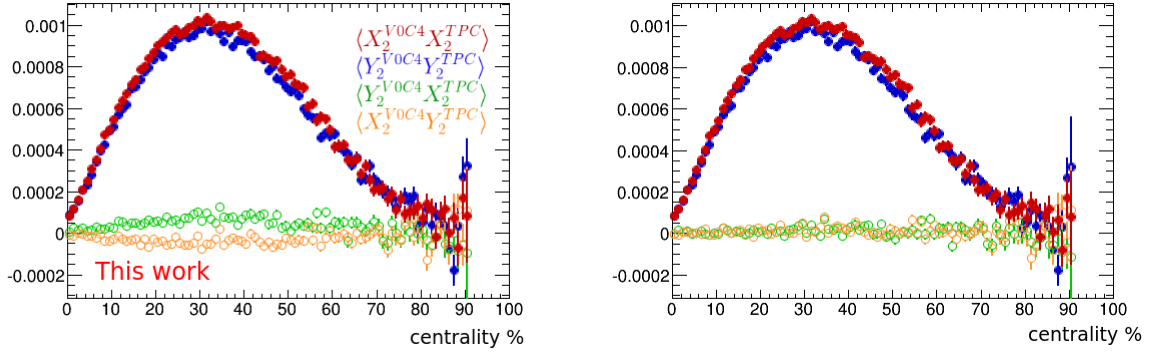


Figure 3.7: Q -vector correlations between ring 4 of the V0-C and the TPC, before (left) and after (right) the alignment correction.

the offset results in significant correlations of opposite sign for the xy - and yx -correlated Q -vector components. After the correction, these cross correlations become equal. It is visible that the impact of the rotation on the xx - and yy -correlations is minimal. This can be expected from Equations 3.33, since for small offsets the cross correlations are more sensitive to gaining a signal ($\propto \sin \Delta\phi$), than the xx, yy -correlations are to losing signal ($\propto \cos \Delta\phi$).

3.5.4 Higher order corrections

Correction parameters for twist and rescaling corrections were extracted with Equation 3.41, using subevent correlations between TPC, V0-A and V0-C. The effect of these, and the earlier corrections, is tested for the measurement of ν_2 and is shown in Fig. 3.8. The effects of twist

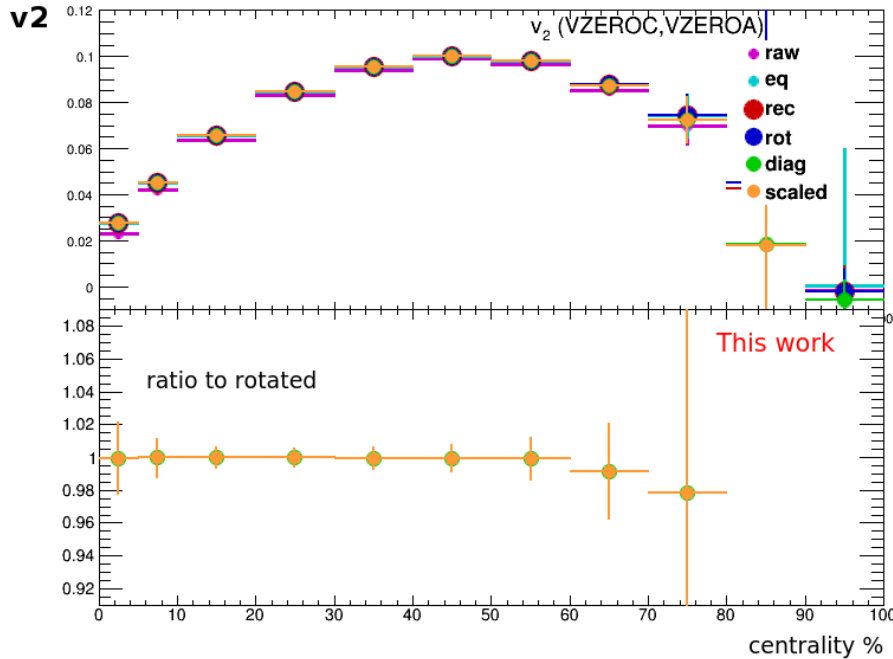


Figure 3.8: ν_2 with higher order corrections. The bottom panel shows the ratio of the alignment (rot), twist (diag) and rescaling (scal) corrections with respect to the recentered q analysis.

and rescaling are found to be below 1% on the measurement of ν_2 . In fact, limited statistics in the sample from where the correction factors are extracted can have a detrimental effect on the quality of the measurement, as we see here above 60% centrality. For the properties and the size of the studies sample, corrections further than rotation are not recommended, at least for the size of the event classes used within the sample.

3.5.5 Measurement of event plane resolution correction factors

Results for the measurement of event plane resolution correction factors are presented for the measured data sample for a range of subevents. For a given detector A a second order event plane angle is defined via q components as

$$\Psi_2 = \frac{1}{2} \text{atan2}(q_y, q_x). \quad (3.51)$$

The event plane resolution correction is calculated with the 3-subevent method [57] using event plane angles calculated for two additional sub-detectors (subevents) B and C via an equation

$$R_2^A = \sqrt{\frac{\langle \cos 2(\Psi_2^A - \Psi_2^B) \rangle \langle \cos 2(\Psi_2^A - \Psi_2^C) \rangle}{\langle \cos 2(\Psi_2^B - \Psi_2^C) \rangle}}, \quad (3.52)$$

Sub-detector correlations between the event plane angles is calculated separately for the x - and y -component of the q and combined for R_2 afterwards.

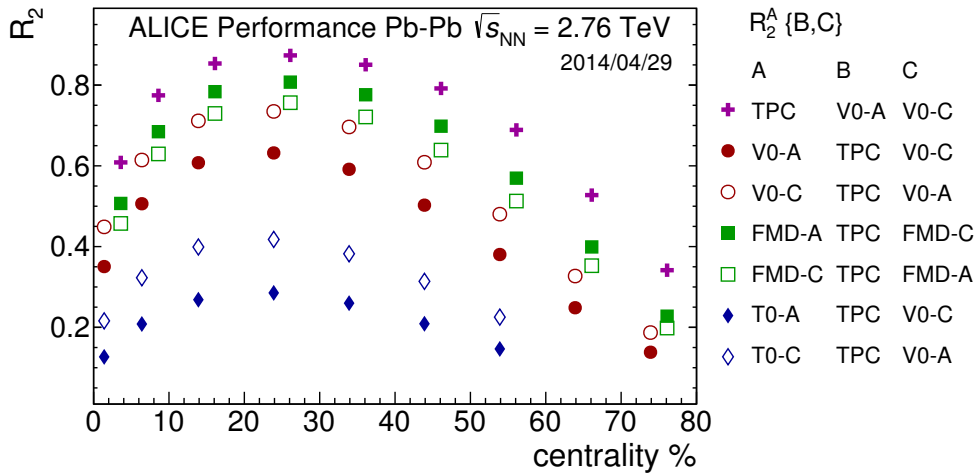


Figure 3.9: Event plane resolution of the TPC, A- and C- side V0, T0, and FMD detectors calculated with the 3-subevent method. Detector used for subevents are indicated in curly brackets, e.g. TPC{V0-C,V0-A}.

Results for the event plane resolution of the TPC, A- and C- side V0, T0, and FMD detectors are shown in Fig. 3.9. It demonstrates the wide range of capabilities that the ALICE detector has to reconstruct event symmetry planes. The T0 has a low resolution due to its small acceptance, which above 60% centrality can become problematic for the symmetry plane measurement. The other detectors show decent resolution for the full 0 – 80% centrality range.

3.5.6 Elliptic flow with multiple event planes

Elliptic flow estimates $v_2^{x,y}$ are calculated separately with x and y components of the Q-vector

$$v_2^x = \langle \cos 2\phi \cos 2\Psi_2^A \rangle / R_2^x, \quad v_2^y = \langle \sin 2\phi \sin 2\Psi_2^A \rangle / R_2^y. \quad (3.53)$$

where ϕ is the azimuthal angle of the TPC tracks selected for the analysis. The averaged results for elliptic flow (v_2) of charged particles with event planes from A- and C- side V0, T0, and FMD detectors are presented in Fig. 3.10.

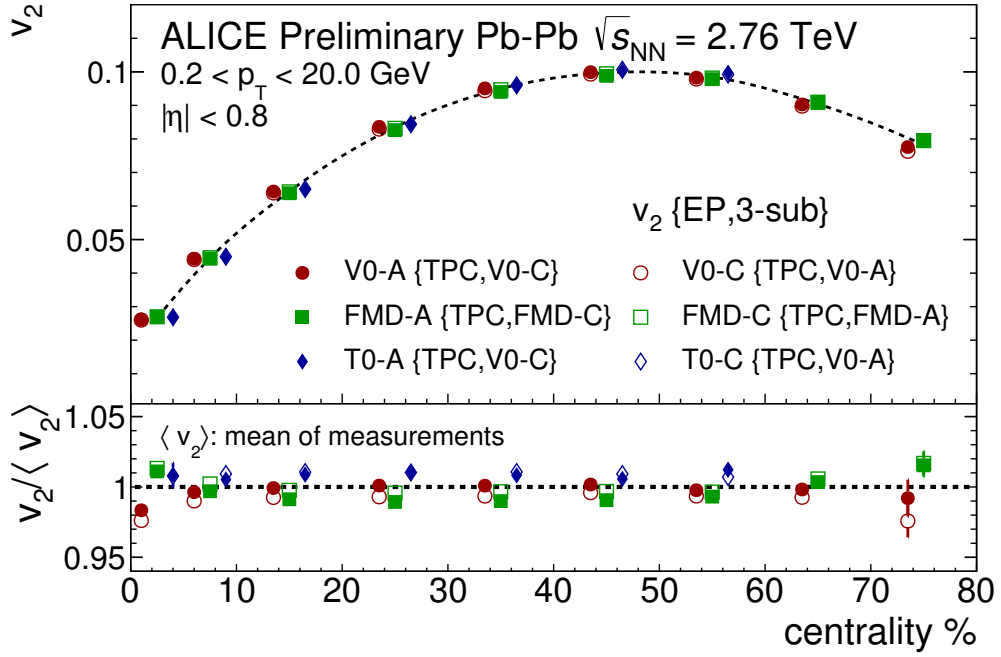


Figure 3.10: Elliptic flow (v_2) of charged particles estimated with event planes from A- and C-side V0, T0, and FMD detectors.

The results show a consistent picture for the measurement of v_2 across a wide centrality range. Detector effects in most central and peripheral events introduce a relatively large bias. In mid-central collisions small deviations are qualitatively in line with the expectations in Section 3.1.2, where it was mentioned that detectors with low resolution correction factors are more sensitive to flow fluctuations and can have a larger value.

3.5.7 Limitations on the corrections for the Q -vector.

The correction procedure as proposed in this chapter is not a guarantee for making a flawless measurement of the Q -vector. Some caveats are discussed in this section.

Assumptions in the derived corrections

The solution for the extraction of correction parameters as applied to the ALICE data and discussed in Section 3.2.3 relies on the presence of a tracking detector. Furthermore it was assumed that multiplicity correlations and flow harmonic correlations [51] are negligible. The validity of the assumptions and a more general solution to the correction equations may be subject for further studies.

Nonflow

Correlations from nonflow between subevents can bias the event plane resolution correction factor, which is not corrected for with the procedure laid out in this chapter. As non-flow decreases with increasing pseudo-rapidity between subevents, the best option is to maximize the gap. Using different regions of the TPC to define subevents and correlating them to the FMD-A and FMD-C subevents we can study the influence of the pseudo-rapidity gap on the estimation of the resolution correction factor.

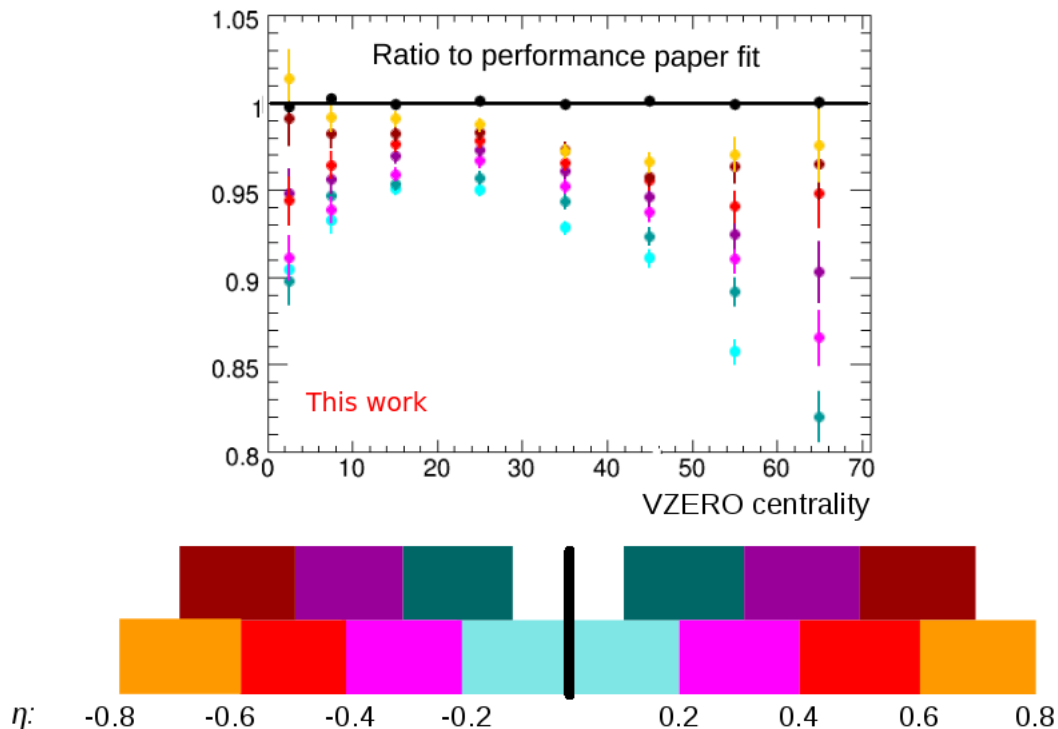


Figure 3.11: Resolution of the FMD with various sizes of η -gap as a ratio to the full FMD resolution in [42].

Figure 3.11 shows the FMD resolution calculated with tracks from two different ranges in the TPC compared to the FMD resolution correction in [42]. If the two subevents are close to

each other (in the most central region of the TPC), the calculated factor is clearly smaller than with two separated subevents at the edge of the TPC. Effects from nonflow in the estimation of the resolution correction factor should be considered for systematic uncertainties on related measurements.

Limited acceptance

The T0 detector has a limited acceptance, and in peripheral events this detector often measures no signal.

For the calculation of the T0 resolution for A or C side, the T0-A–T0-C plane correlations become skewed when one of the detectors is empty. When the T0 has a signal, it needs to be correlated with a detector that has a signal, e.g. the V0 detector. Figure 3.12 shows the v_2 results in fine bins for v_2 measured with the T0 A and C event plane with different subevents. v_2 for subevents that include the T0-A–T0-C correlation start deviating below 60% centrality, and T0-V0 subevents above 60%. Effects from the empty channels could not be mitigated here for the flow measurement.

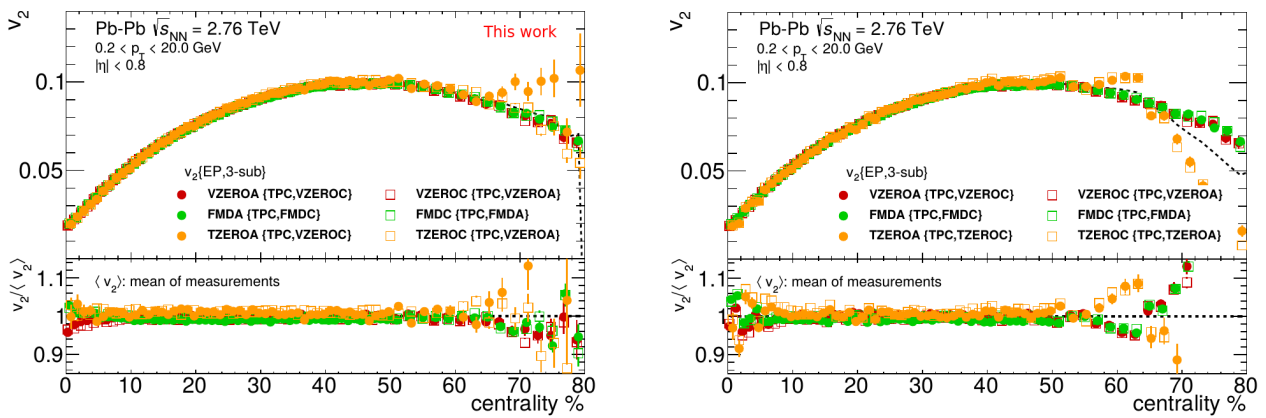


Figure 3.12: v_2 results with T0-A(C)–V0-(C)A subevent correlations on the left side, and T0-A–T0-C on the right side.

3.6 Summary

Detectors with non-uniform azimuthal acceptance present a challenge to studies that include the measurement of azimuthal correlations. In a paper by Selyuzhenkov and Voloshin [51] a procedure was introduced to correct for these effects. Based on this procedure, a correction framework [53] was developed that is broadly applicable to data from heavy ion experiments. Additional corrections such as gain equalization and detector alignment were also developed and included. The software framework is highly configurable, allowing users to define the specific set of subevents and corrections they require, after which a number of iterations is required to extract correction parameters and apply corrections to data. The resulting corrected Q -vectors can be used for symmetry plane related analyses. In a toy model particles were generated with a ν_2 modulated particle distribution for a group of subevents that reflect a setup similar to ALICE (e.g. TPC and V0/FMD), but with introduced non-uniform acceptance effects. After the corrections the magnitude of the input ν_2 was accurately reconstructed. The effect of the corrections, especially for twist and rescaling, deserve closer scrutiny for detector setups without a close to uniform central tracker. The software framework was used to apply corrections to ALICE data, from which the resolution correction parameter R_2 and flow ν_2 were measured using a large group of subevents (TPC, V0, T0, FMD). Corrections for alignment, twist and rescaling were found to be negligible for these measurements. The results demonstrate that ν_2 can be extracted within a systematic uncertainty of 4% depending on event centrality. The existing differences are qualitatively in line with expectations from [48], where detectors with low R are more sensitive to flow fluctuations.

4 Charge-dependent correlations

The charge dependence of the azimuthal correlations was suggested [28] as an observable which can probe the effects of spontaneous local parity violation in quantum chromodynamics (QCD). It was argued [14, 58] that local parity violation, which is driven by nontrivial topological structure of the QCD vacuum [11], coupled with a strong magnetic field generated by the moving ions may result in experimentally observable separation of charges along the direction of the magnetic field. This phenomenon is called the chiral magnetic effect (CME) [14, 58]. Due to spontaneous nature of the CME, its contribution would vanish to the direct parity-odd observables and therefore its search is only possible with parity-even two- and multi-particle correlations.

4.1 Correlators

Charge dependent two-particle correlations relative to the reaction plane Ψ_{RP} (the plane defined by the impact parameter and the moving ion direction),

$$\langle \cos(\varphi_a + \varphi_b - 2\Psi_{\text{RP}}) \rangle, \quad (4.1)$$

were originally proposed in [28] as a sensitive probe of the CME. The angle brackets in Eq. (4.1) denote an average over all particles for large ensemble of events, φ_a and φ_b are the azimuthal angles of the particle with a charge a and b respectively. Equation (4.1) defines the first harmonic of the two particle correlation relative to the reaction plane. The generalized form of this equation that describes the higher mixed harmonics can be written as:

$$c_{nm}^{ab} \{\Psi_k\} = \langle \cos(n\varphi_a - m\varphi_b - [n - m]\Psi_k) \rangle, \quad (4.2)$$

where n , m , and k are integers, and n and k are positive. For $n = -m = 1$ and $\Psi_k = \Psi_{\text{RP}}$ the expression of Eq. 4.1 is retrieved. With the k -th order collision symmetry plane angle Ψ_k the event-by-event fluctuations in the initial energy density of a heavy-ion collision can be taken into account. In the absence of such fluctuations the angle Ψ_k coincides with that of the reaction plane, $\Psi_k = \Psi_{\text{RP}}$.

For $n = m$, Eq. 4.2 gives the two particle correlation, that doesn't have an explicit dependence on the symmetry plane angle:

$$c_n^{ab} = \langle \cos(n[\varphi_a - \varphi_b]) \rangle. \quad (4.3)$$

For $m = 0$ or $n = 0$, Eq. (4.2) becomes a one particle correlation relative to the Ψ_k symmetry plane, which is the measurement of the anisotropic flow coefficients v_n^a :

$$v_n^a \{\Psi_k\} = \langle \cos n\Delta\varphi_a^{(k)} \rangle. \quad (4.4)$$

Here $\Delta\varphi_a^{(k)} = \varphi_a - \Psi_k$ is the azimuthal angle φ_a of the particle with charge a relative to Ψ_k .

The charge dependent correlations are reported for the following combinations:

- The first four harmonics ($n = 1 - 4$) of the two particle correlation defined by Eq. 4.3,
- the first and the second harmonic of Eq. 4.2 relative to the second and the fourth order symmetry planes given by the following equations:

$$\langle \cos(\varphi_a + \varphi_b - 2\Psi_2) \rangle, \quad (4.5)$$

$$\langle \cos(2\varphi_a + 2\varphi_b - 4\Psi_4) \rangle, \quad (4.6)$$

$$\langle \cos(2\varphi_a + 2\varphi_b - 4\Psi_2) \rangle. \quad (4.7)$$

- and the mixed harmonic correlation:

$$\langle \cos(\varphi_a - 3\varphi_b + 2\Psi_2) \rangle; \quad (4.8)$$

Equation 4.1 is also studied with identified particles. Here the first particle is an identified hadron and the second an unidentified hadron, measured with respect to the reaction plane and differentially against the p_T of the identified particle,

$$\langle \cos(\phi^{PID}(p_T) + \phi^h - 2\Psi_2) \rangle. \quad (4.9)$$

This range of measurements can be used to disentangle the contributions originating from the signal (i.e. CME) and the one coming from background sources (e.g. local charge conservation). Below some characteristics of their sensitivity to the relative contributions are discussed.

4.1.1 Sensitivity to the CME

The CME, as discussed in the Section 1.7.2, results in an asymmetry in the charge production relative to the symmetry plane. This leads to the introduction of P -odd sine terms in the Fourier decomposition of the particle azimuthal distribution relative to Ψ_n [14, 28, 58]:

$$\frac{dN}{d\varphi_a} \propto 1 + 2 \sum_n [v_n^a \cos n\Delta\phi_a^{(n)} + a_n^a \sin n\Delta\phi_a^{(n)}]. \quad (4.10)$$

The leading order coefficient a_1^a quantifies the magnitude of the charge separation perpendicular to the symmetry plane, while the higher order coefficients a_n^a with $n > 1$ describe its specific shape in azimuth [59]. The fluctuations can change sign from event to event, and as a result $\langle a_n^a \rangle$ is zero. Instead the values have to be measured with correlation techniques that are sensitive to the parity even product $\langle a_n^a a_m^b \rangle$ through combinations of Eq. 4.2. This becomes apparent when we decompose Eq. 4.1:

$$\begin{aligned} \langle \cos(\varphi_a + \varphi_b - 2\Psi_2) \rangle &= \langle \cos \Delta\varphi_a \cos \Delta\varphi_b \rangle \\ &- \langle \sin \Delta\varphi_a \sin \Delta\varphi_b \rangle, \end{aligned} \quad (4.11)$$

where $\Delta\varphi_{a,b} = \Psi_2 - \varphi_{a,b}$. These two different terms of Eq. 4.11 quantify the correlations in- and out-of-plane, respectively. The construction of the correlator in Eq. 4.11 as the difference

between these two contributions suppresses correlations not related to the reaction plane orientation (non-flow). The latter term of Eq. 4.11 is sensitive to the charge correlations resulting from the CME: $\langle \sin \Delta\varphi_a \sin \Delta\varphi_b \rangle \sim \langle a_1^a a_1^b \rangle$. It follows, that the contribution from the CME to the generalized mixed harmonic correlations of Eq. 4.2 is quantified by the average product $\langle a_n^a a_m^b \rangle$ of the single particle azimuthal asymmetry:

$$c_{nm}^{ab} \{\Psi_k\} \sim (-1)^{n-m} \langle a_n^a a_m^b \rangle. \quad (4.12)$$

There are few quantitative predictions in the literature for the CME at LHC energies. The magnitude of the charge separation due to CME at RHIC energies was predicted [14, 58] to be of the order of $a_1^a \sim 10^{-2}$ for mid-central collisions which corresponds to a $\langle a_1^a a_1^b \rangle \sim 10^{-4}$ contribution to the correlation c_{11}^{ab} . Alternative calculations [60] can also result in much smaller estimates of $\langle a_1^a a_1^b \rangle \sim 10^{-7}$.

The correlations between pairs of particles with same charge due to CME are expected to be positive and of the same magnitude, $\langle a_1^+ a_1^+ \rangle = \langle a_1^- a_1^- \rangle > 0$. The correlations of opposite sign are expected to be of the same magnitude but of opposite sign. Because of the longer average path length for particles of opposite charge, it is expected opposite sign correlations are more diluted by the surrounding medium [14], resulting in $\langle a_1^+ a_1^+ \rangle = \langle a_1^- a_1^- \rangle \gg -\langle a_1^+ a_1^- \rangle$. In addition, the evolution of the magnitude of the correlations originating from CME with the collision centrality, is expected to follow an inverse multiplicity scaling [29], similar to that of any cluster type particle production. The CME is expected to produce correlations of particles separated in pseudorapidity within one unit, which is typical for hadronic cluster production [61]. As a non-perturbative effect of quantum chromodynamics the CME contribution should be localized in the transverse momentum range of $p_T < 1$ GeV/c [14]. However, the momentum boost from radial flow may result in an relevant correlations to a higher transverse momentum range. The collision energy dependence of these correlations strongly depends on the time integration over which the magnetic field develops and decays. Model calculations for the LHC energies range from prediction of no change of the magnitude of the effect [14, 62] to its strong decrease [14, 63] with increasing collision energy i.e. from RHIC to LHC.

4.1.2 Sensitivity to local charge conservation

Local charge conservation, the leading background in the charge dependent measurements, results in a balancing charge partner for every charged particle created in the system, as was already discussed in Sec. 1.7.2. The initial correlation in coordinate space between these balancing charges, is converted via the development of the initial pressure gradients and the subsequent radial expansion of the system modulated by the azimuthal anisotropic flow into non-zero same and opposite charge pair correlation in momentum space [38, 64]. The effects of local charge conservation are conventionally quantified with the balance function [38, 65], defined as the difference between the unlike- and the like-sign pair densities divided by the number of trigger particles. Each pair density term is corrected for detector acceptance and efficiency effects using mixed events. It follows that the charge dependent difference between observables 4.2 for the same and opposite sign pairs of Eq. 4.2, $\Delta c_{nm} \{\Psi_k\} = [2c_{nm}^{+-} - c_{nm}^{--} - c_{nm}^{++}] / 2$,

$$\Delta c_{nm} \{\Psi_k\} = [2c_{nm}^{+-} - c_{nm}^{--} - c_{nm}^{++}] / 2, \quad (4.13)$$

can be related to the different harmonics

$$\Delta c_n = [2c_n^{+-} - c_n^{--} - c_n^{++}] / 2 \quad (4.14)$$

of the balance function via the relation [37, 66, 67]

$$\Delta c_{nm} \{ \Psi_k \} = v_p \Delta c_n + v_{p,c}^{(n)} - v_{p,s}^{(n)}, \quad (4.15)$$

where $p = |n - m|$, and

$$v_{p,c}^{(n)} = \Delta \left\langle \cos n[\varphi_a - \varphi_b] \cos p \Delta \varphi_b^{(k)} \right\rangle - v_p \Delta c_n, \quad (4.16)$$

$$v_{p,s}^{(n)} = \Delta \left\langle \sin n[\varphi_a - \varphi_b] \sin p \Delta \varphi_b^{(k)} \right\rangle. \quad (4.17)$$

The contribution to the charge dependent part of the mixed harmonic correlations (4.2) from local charge conservation is given by three terms on the right hand side of Eq. (4.15). These terms, visible in Fig. 1.16, describe [37, 66] (i) the difference between the number of balancing charges in- and out-of-plane (ii) the azimuthal correlation width in-plane and out-of-plane, and (iii) the preferential in-plane emission of balancing charges. Blast-wave model calculations [37, 66] tuned for RHIC energies can qualitatively describe the charge dependent part of the correlation (4.1) observed at RHIC [26, 29]. According to Eq. (4.15) one may expect a scaling of the contribution due to local charge conservation with the magnitude of the anisotropic flow coefficients v_p . Such scaling can be exploited [68] to disentangle contributions to observables (4.2) from CME and effects of local charge conservation.

4.1.3 Sensitivity to anisotropic flow fluctuations

Anisotropic flow fluctuations due to event-by-event variation of the initial energy density may contribute to the charge independent part of Eq. (4.2). The different harmonics of the two particle correlation relative to Ψ_2 (i.e. Eq. 4.5 and Eq. 4.8) can be related to the dipole-like initial energy fluctuations [69]. Hydrodynamic model calculations [69] for observable (4.5) yield a magnitude which is similar to that measured by the STAR Collaboration [29]. At the same time, it is a challenge for the same hydrodynamic models which assume longitudinal boost invariance of the system to reproduce the strong dependence of (4.1) on the particle pair separation in pseudorapidity reported by STAR [29] and ALICE [30] Collaborations.

4.1.4 Other sources of charge dependent correlations

In addition to the sources described above, the mixed harmonic correlations of Eq. 4.2 are also sensitive to decays of clusters which exhibit anisotropic flow. According to [28], this is a mechanism capable of generating two- and multi-particle correlation relative to Ψ_n . It includes the particle production from flowing resonance decays or the reaction plane dependent particle emission by jets propagating through the dense and azimuthally asymmetric matter created in a heavy-ion collision. Quantum interference (HBT), Coulomb effects, or global polarization [70, 71] may also contribute to the magnitude of the correlations of Eq. 4.2. These effects are known to be either localized in a very narrow kinematic region (e.g. HBT), or expected to be small as in the case of global polarization [29, 72].

4.2 Measurement technique

The mixed harmonic correlations of Eq. (4.2) were measured using the event plane method [73]. In the event plane method, the symmetry plane angle Ψ_k in Eq. (4.2) is estimated with the event plane angle $\Psi_{EP}^{(k)}$ [57], constructed from the charge azimuthal distribution:

$$c_{nm}^{ab} \{ \Psi_{EP}^{(k)} \} = \frac{\langle \cos(n\varphi_a - m\varphi_b - (n-m)\Psi_{EP}^{(k)}) \rangle}{R_p^{(k)}} \quad (4.18)$$

The event plane resolution correction $R_p^{(k)}$ ($p = |n-m|$) is extracted using the three sub-event technique described in [57]:

$$R_p^{(k)} = \sqrt{\frac{\langle \cos p [\Psi_{EP}^{(k)} - \Psi_A] \rangle \langle \cos p [\Psi_{EP}^{(k)} - \Psi_B] \rangle}{\langle \cos p [\Psi_A - \Psi_B] \rangle}}, \quad (4.19)$$

where $\Psi_{A,B}$ are two additional event plane angles calculated for non-overlapping subsets A and B of the measured particles. Effects of non-uniform azimuthal acceptance in the event plane determination are corrected using the method discussed in [51].

A three particle cumulant was also measured

$$c_{nm}^{ab} \{3\} = \langle \langle \cos(n\varphi_a - m\varphi_b - (n-m)\varphi_c) \rangle \rangle / \nu_p. \quad (4.20)$$

The approach described in [50] was used in the analysis to avoid nested loops in the cumulant calculations. The cumulant calculations are robust against the bias due to azimuthal non-uniformity of the detector [49, 74, 75].

The identified particle correlations are measured for the correlation 4.9, with the event plane method from Eq. 4.18 and Eq. 4.19.

4.3 Experimental setup

4.3.1 Event selection

About 13 million minimum bias Pb–Pb collisions at the center of mass energy $\sqrt{s_{NN}} = 2.76$ TeV recorded by ALICE in year 2010 were analyzed. Detailed description of the ALICE detector subsystems can be found in chapter 2.

Event distributions for centrality and vertex along the beam line (z -vertex) is shown in Figure 4.1.

For this analysis, the Time Projection Chamber (TPC), two forward scintillator arrays (V0), and two forward silicon strip detectors (FMD) were used. Online triggering and offline event selection are described in [19, 76]. In this analysis, the collision vertex along the beam direction was restricted to be within 10 cm from the nominal interaction point. Events corresponding to the most central (0-10%) collisions were grouped in 5% centrality bins, while events in 10-70% centrality range were grouped in 10% wide bins. The identified particle correlations are reported in 10-30% and 30-50% centrality bins to ensure good statistical significance, which were merged from measurements in respectively the 10-20% and 20-30%, and 30-40% and 40-50% ranges.

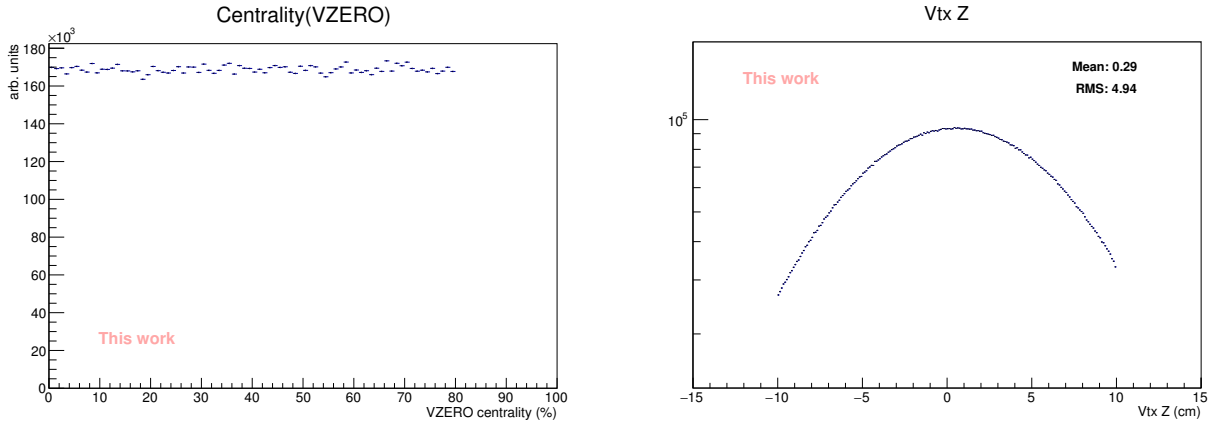


Figure 4.1: Centrality and z -vertex distribution for the selected events.

4.3.2 Track selection

The analysis is performed with TPC standalone tracks and with the following track selection

- $0.2 < p_T < 5 \text{ GeV}/c$
- $|\eta| < 0.8$
- $DCA, |DCA_{x,y,z}| < 3.0 \text{ cm}$
- Number of TPC clusters, $N_{cls} > 70$
- Remove outliers in the TPC energy loss distribution, $dE/dx > 10.0$ (rejects tracks at the edge of the TPC sectors)
- TPC track fit quality, $0.2 > \chi^2 > 4$

The distributions for ϕ , η , p_T and $DCA_{x,y}$ after track selection is shown in Figure 4.2.

Two V0 detectors, covering the pseudorapidity range $2.8 < \eta < 5.1$ and $-3.7 < \eta < -1.7$, are used for triggering and determination of the collision centrality and the event plane reconstruction. Two FMD detectors, which are positioned at $-3.4 < \eta < -1.7$ and $1.7 < \eta < 5.0$ and have a high granularity in azimuthal angle ϕ and pseudorapidity η , are also used for the event plane determination.

4.4 Systematic uncertainties

The dominant source of systematic uncertainty in the measurement of the mixed harmonic correlations of Eq. 4.2 (with exception of Δc_{22}) comes from the event plane determination of Eq. 4.18. The difference between the results with the event plane estimated from the V0 and the FMD detectors was used to assign the relevant systematic uncertainty.

The measured two-particle correlations (4.3) between the same sign pairs of the positive and negative charges are consistent within the statistical uncertainty of the measurement. Figure (4.3) presents three particle cumulants, where the symmetry plane angle is replaced by a third particle measured at midrapidity, and no resolution correction is applied. For most

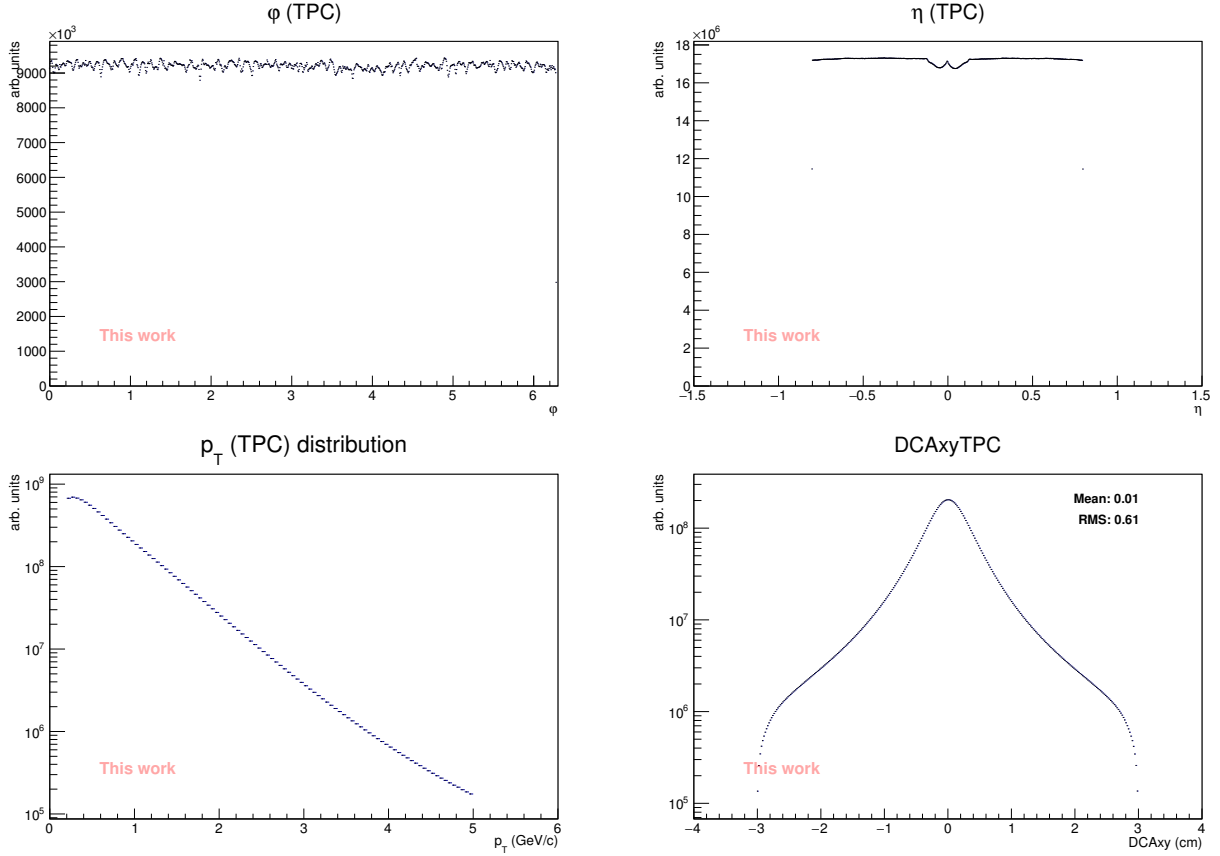


Figure 4.2: ϕ -, η -, p_T - and $DCA_{x,y}$ distribution of tracks after track selection.

of the correlations a considerable dependence on the charge of the third particle c was observed. This charge dependence was studied as a function of $\Delta\eta$ between the third and the first two particles and found to diminish strongly with increasing separation. To avoid this contribution to the charge dependence, further measurements are presented with the event plane method. In Sec. 4.5 results are reported for an average same sign charge pair correlations $c_{nm}^{(same)}\{\Psi_k\} = [c_{nm}^{++} + c_{nm}^{--}]/2$ and opposite sign charge pairs $c_{nm}^{(opp)}\{\Psi_k\} = c_{nm}^{+-}$.

Other sources of systematic uncertainties considered in the analysis are summarized below. The data samples recorded with an opposite polarity of the main magnet in ALICE were analyzed separately and results were found to be consistent within statistical precision. The multiplicity of charged particle tracks recorded in the TPC was used to determine the collision centrality in addition to the multiplicity measured by the V0 detectors which is used for the final results. A cut on the collision vertex position v_z along the beam direction was varied from the nominal value of $|v_z| < 7$ cm to $|v_z| < 10$ cm. The charged particle track selection was varied to estimate the systematic uncertainty due to tracking efficiency, and contamination from fake and secondary tracks which do not originate directly from the primary collision vertex. A cut on the minimum number of TPC hits associated with charged particle track was varied from 70 to 110 hits. The cut on the distance of closest approach of the track to the collision vertex in the transverse plane was reduced from nominal 3 cm to 0.3 which corresponds to the change in relative contamination from the secondary particles from $\sim 6\%$ to $\sim 15\%$. The difference between the reconstruction using TPC and ITS+TPC was also contributed to the systematic uncertainty,

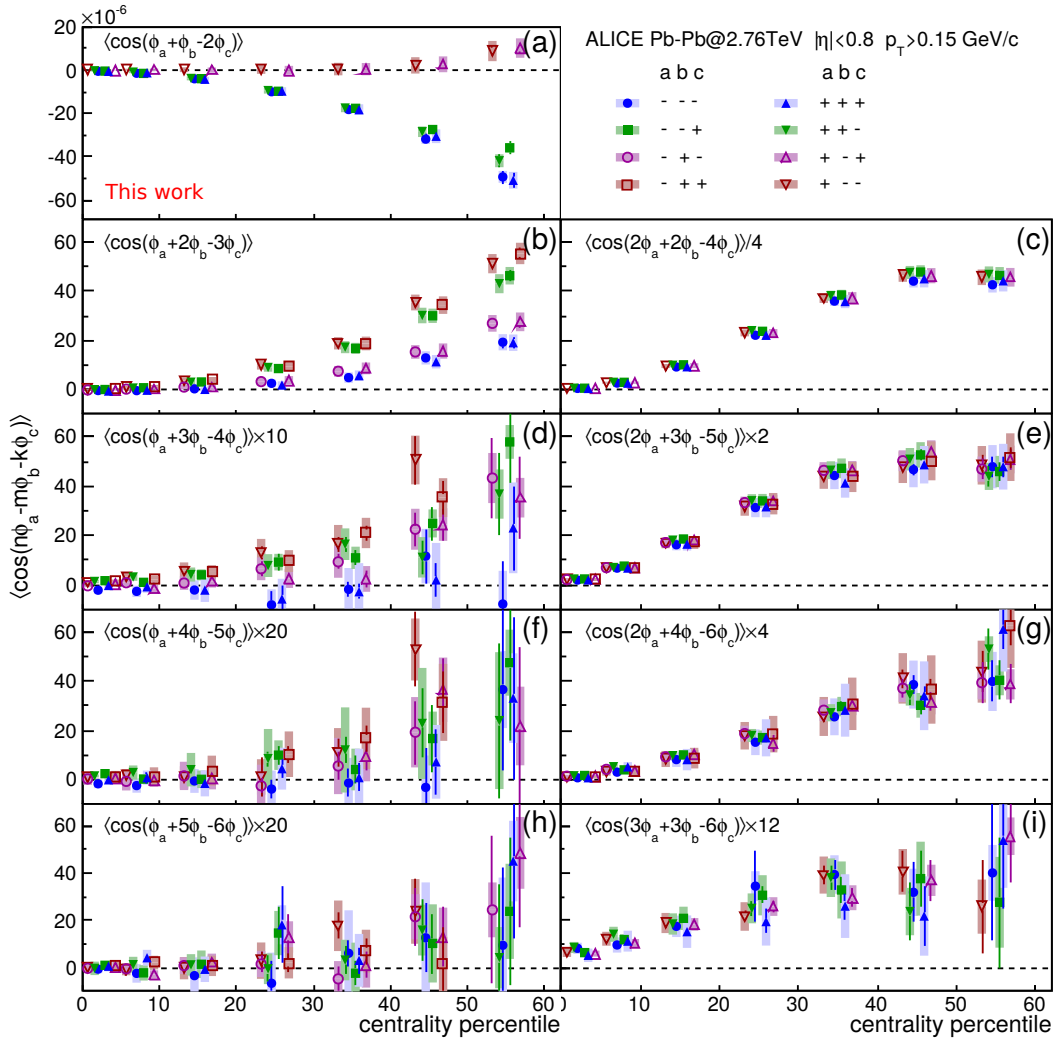


Figure 4.3: Centrality dependence of the correlations (a,c,i) $\langle \cos(n[\varphi_a + \varphi_b - 2\varphi_c]) \rangle$ for $n = 1 - 3$, (b,d,f,h) $\langle \cos(\varphi_a + n\varphi_b - (n+1)\varphi_c) \rangle$ for $n = 2 - 5$, and (e,g) $\langle \cos(2\varphi_a - n\varphi_b + (n-1)\varphi_c) \rangle$ for $n = 3, 4$. This is work by Hori of [77].

especially for the 2-particle correlation. For the correlations with event plane, residual effects from detector non-uniformity are checked by replacing the cosine in Equation 4.18 by a sine.

For the identified particle results, additionally particle identification selection is varied to test the robustness of the observed correlations. Finally a weighted average was made of the identified particle correlations using identified particle spectra and demonstrated consistency with the unidentified hadron correlation. All significant deviations are added to the final systematic uncertainty, which has been calculated for each bin with deviations of the mentioned systematic checks added in quadrature.

For the correlation from Eq. 4.9 in the intermediate p_T region, the total relative systematic uncertainty is around 5% for unidentified hadron correlations and 20% for the correlations with an identified hadron. Figure 4.4 shows the relative magnitude of the systematic uncertainty on the same sign correlation for the identified particle correlations. Systematic uncertainty for unidentified hadrons is around 5% in the mid- p_T region.

Some of the contributions to the systematic uncertainty of the identified particle correlation are detailed in the following sections.

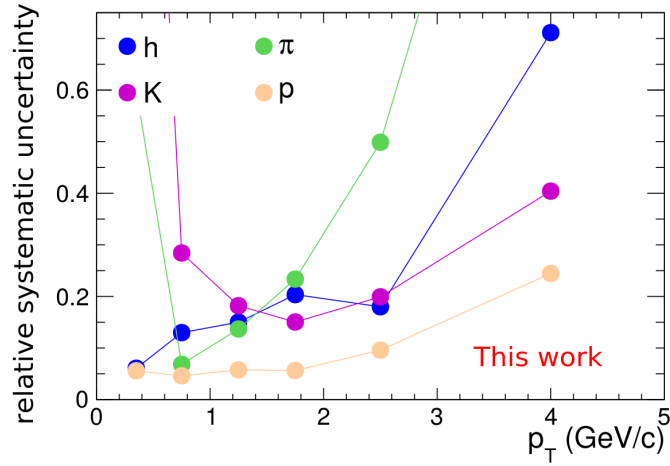


Figure 4.4: Relative total systematic uncertainty for the same sign correlation $\langle \cos(\varphi_\alpha + \varphi_\beta - 2\Psi_{RP}) \rangle$.

4.4.1 Track reconstruction and quality cuts

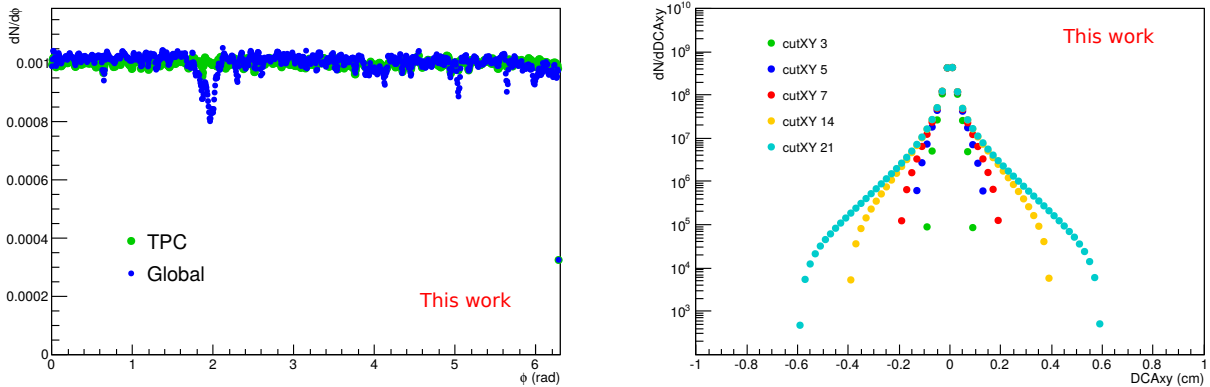


Figure 4.5: Left: normalized ϕ -distribution of TPC and global tracks with respectively standard TPC and global track selection. Right: $DCA_{x,y}$ distribution for global tracks with p_T -dependent DCA cuts.

TPC clusters

TPC clusters were varied from 70 to 100 in steps of ten. The accuracy of the reconstruction of track parameters, as well as the particle identification, is correlated to the number of clusters associated to the track. However as requirement of number of clusters is increased, the efficiency goes down, which may lead to changes in the observed correlation.

The observed variation is small and taken into account for the final systematic.

For further study of the effects of contamination on the measurement a study similar to one from the spectra group is performed for global tracks. The analysis is run with different $DCA_{x,y}$ cuts for the selection of identified particles. The following cut is applied: $DCA_{x,y} > cut_{XY} * (0.0026 + 0.0050/p_T^{1.01})$, for values of cut_{XY} of 3, 5, 7, 14 and 21. The DCA distributions for the respective cuts are shown in Figure 4.5. The variation in the result is small, and taken as a systematic uncertainty, instead of extrapolating to a uncontaminated sample result.

Additionally the value of the Bayesian probability for a given identified particle was varied from 0.7 to 0.8 and 0.9. The increase of the probability corresponds to a larger exclusion of the overlap, and consequently increases the purity of the identified particle sample.

The purity in the sample of identified particles is also varied by tightening the TOF and TPC $n\sigma$ requirements, from 3σ to 2σ and 1σ . The distributions of these samples for $\sigma < 3$ is illustrated in the Figure 4.6. The samples are mostly non-overlapping, though some overlap can be seen. The effect of this contamination is studied by the tightening of the $n\sigma$ cut.

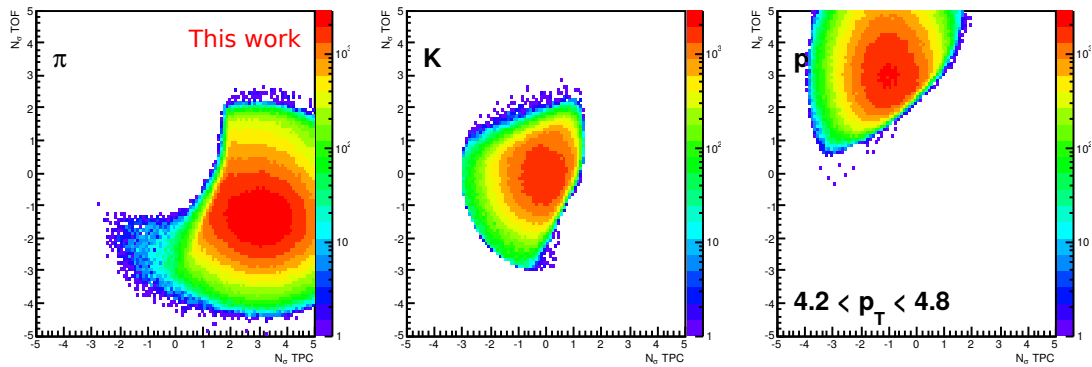


Figure 4.6: TOF kaon- $n\sigma$ vs TPC kaon- $n\sigma$ for selected pions, kaons and protons. Kaons are centered at (0,0).

The resulting variation shown in Figure 4.6 is taken into account for the systematic uncertainty.

Another issue that is investigated is the turn-on curve of the PID efficiency due to the TOF requirement at low p_T . TOF is required over the entire p_T range. The TOF requirement was released to a momentum of 0.2, 0.4 and 0.6 GeV/c to study the effect of the different spectral shapes. The differences are included in the uncertainty. However the contribution to the final systematic uncertainty is minimal. The biggest penalty is payed in the statistical precision of the measurement.

Efficiency

The effect of track efficiency on the correlations is studied by flattening the track efficiency in the p_T range 0.2-5.0 GeV/c. The TPC standalone track reconstruction efficiency with 2010 standard track cuts, shown in Figure 4.7, is used to shape the measured p_T spectrum of particles to the original spectrum. A rejection factor is defined as function of p_T as follows: $r(p_T) =$

$(\varepsilon(p_T) - \varepsilon_{minimum})/\varepsilon(p_T)$. The right panel of the figure shows that the flattening procedure is properly applied and can again reproduce the shape of the track efficiency.

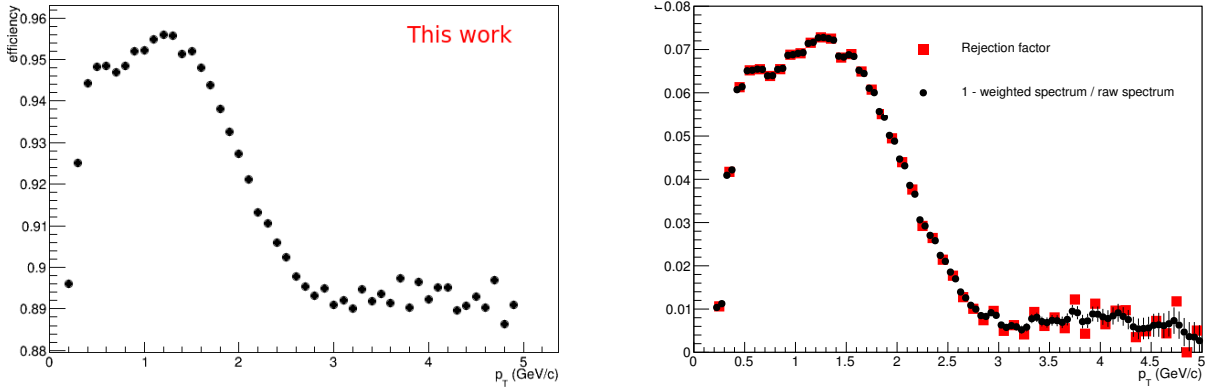


Figure 4.7: Left: TPC reconstruction efficiency vs p_T . Right: Rejection factor used as an input and recovered from the ratio of the distribution before and after the rejection was applied.

The rejection factor was applied to both the identified and the charge particle. The variation of the result is small.

4.4.2 Charge combinations

The individual charge combinations can reveal possible biases, especially interesting for the charge of the identified particle. For protons, it is known that there is contamination from knock-out and weak decays at low p_T . For at least up to 1 GeV/c only antiprotons will be used in the measurement, similar to the elliptic flow analysis for identified particles. ν_2 measurements for protons and antiprotons is consistent above 1 GeV/c. The variations due to the different charge combination is taken into account for the final systematic uncertainty.

4.4.3 Sine term

We can compare the magnitude of $\langle \sin(\phi^{PID}(p_T) + \phi^h - 2\Psi_{2,RP}) \rangle$ to the cosine observable to estimate the magnitude in the correlation of residual detector effects. The sine terms are mostly consistent with zero, the magnitude of the sine correlation is added to the systematic uncertainty.

4.4.4 Event planes

The two particle correlation is calculated with respect to the event plane. Several ALICE sub-detectors are suitable for event plane estimation and are used to cross-check the influence of the choice of the event plane on the measurement. Deviations are added to the systematic uncertainty.

4.4.5 Closure test for identified particle correlations

The hadron-hadron correlation with respect to the reaction plane consists of pion-hadron, kaon-hadron, proton-hadron and other particle-hadron correlations. Since pions, kaons and protons together form the large majority of produced hadrons, it should be possible to use a weighted average of PID-hadron results to get the hadron-hadron results. This is the test is shown in this section. Spectra for positive and negative pions, kaons and protons are used as a weight in the average of the PID-hadron correlations. The different charge combinations are averaged individually, using the corresponding charge spectrum. The result is shown for four centrality ranges in Figure 4.8.

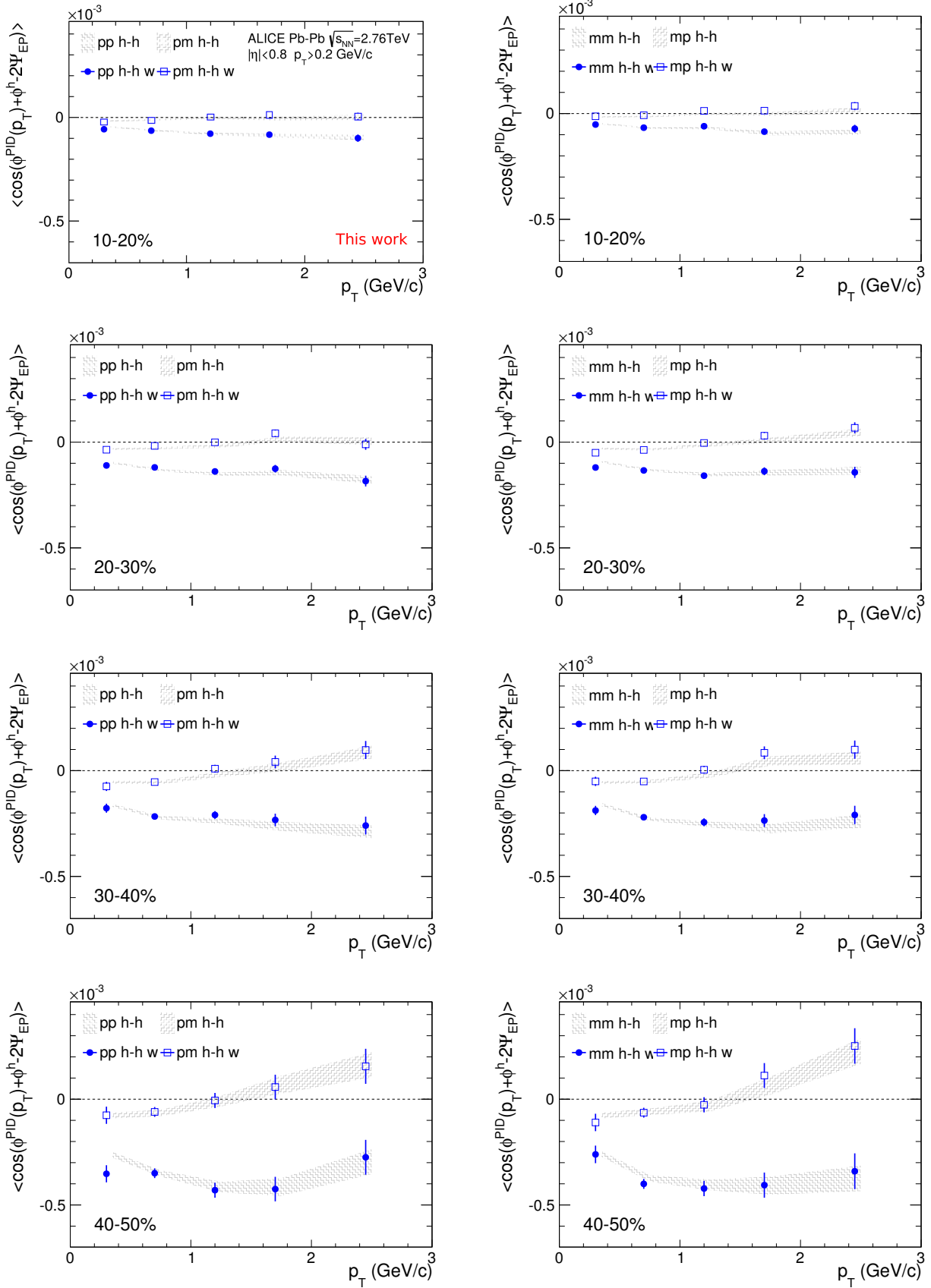


Figure 4.8: Weighted average of PID-hadron correlations (blue circles) compared to the hadron-hadron correlation (grey fill area), in four centrality ranges and for positive and negative charge combinations separately. All errors shown are statistical.

4.5 Results

4.5.1 Two particle correlation

Figure 4.9(a)-(d) shows the centrality dependence of the first four harmonics of the two particle correlation ($\langle \cos(n[\varphi_a - \varphi_b]) \rangle$) for $n = 1 - 4$ for different charge combinations in Pb-Pb collisions at $\sqrt{s_{NN}} = 2.76$ TeV. All four harmonics are positive for all centralities. It is seen that

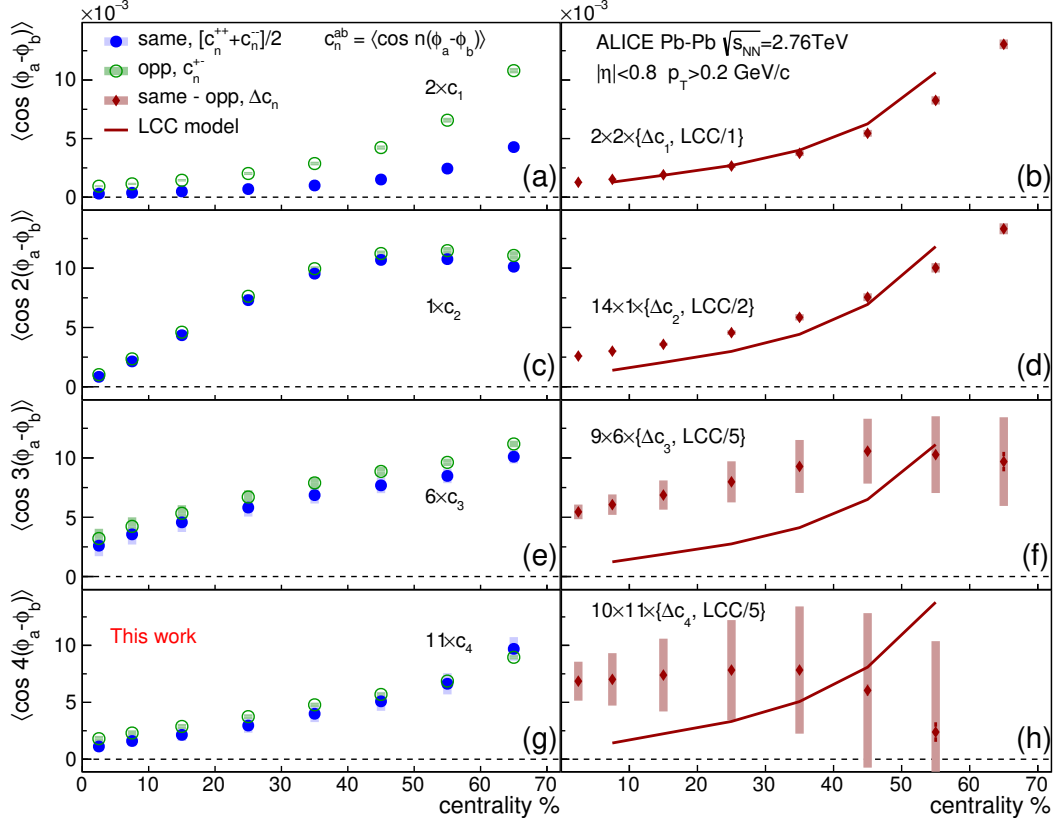


Figure 4.9: On the left side is shown the centrality dependence of the correlation $\langle \cos(n[\varphi_a - \varphi_b]) \rangle$ for $n = 1 - 4$, and on the right side the charge dependent part (Eq. 4.14) of the correlations. Results are compared to model calculations which incorporate effects of the local charge conservation [67].

the correlation between pairs of particles with opposite charge are larger than that of particle pairs with same charge for all harmonics except for $n = 4$ in 50-70% peripheral collisions.

The right side of Figure 4.9 presents the differences in the magnitude of the correlations between particle pairs with opposite and same charge, as a function of centrality. This difference, as discussed in Section 4.1, is related to the different harmonics of the symmetry plane independent balance functions. A strong centrality dependence is reported for the first two harmonics, that reduces for $n = 3$ and $n = 4$. The experimental results are compared with the Blast-Wave model calculations which incorporates effects of local charge conservation [67]. The blast wave parameters were tuned to describe the hadron spectra, thus constraining the magnitude of radial flow, and the anisotropic flow coefficients v_2 and v_4 measured at the LHC [19, 78, 79]. For these model calculations, the azimuthal width σ_ϕ of the emission of balancing charges was set to zero. This choice gives an extreme case of point-like correlated charge particle production

and can be considered as an upper limit for contributions, based on this model, due to local charge conservation. It is seen that the model describes the magnitude and the centrality dependence of the first harmonic up to the 30-40% centrality class. However, for more peripheral collisions and higher harmonics, the measured correlations are systematically below the predictions of this model. It is important to note that the different harmonics of the two-particle correlations of Eq. 4.3 is expected to be dominated by the background (e.g. local charge conservation and cluster formation), while the contribution from the CME will have little impact in this measurement.

The charge independent part of the two-particle correlations of Eq. 4.3 is sensitive to the anisotropic flow harmonics. In particular the shape of the centrality dependence of the second moment shown in the left column of Fig. 4.9 resembles the behavior of the elliptic flow (its squared value) [19] which indicates a dominant flow contribution to the second moment.

4.5.2 First and second moments of the two particle correlation relative to Ψ_n

Figure 4.10(a) presents the centrality dependence of $\langle \cos(\varphi_a + \varphi_b - 2\Psi_2) \rangle$ for different charge combinations similar to what was published [30]. The correlations for particle pairs of the same charge are negative and exhibit a strong centrality dependence. On the other hand the magnitude of the corresponding correlations for particle pairs with opposite charge is significantly smaller, with no evident strong dependence on centrality. This picture is in qualitative agreement with initial CME expectations, where the magnitude of correlations of pairs with opposite charge is diluted due to the interactions with the dense medium that one of these particles has to traverse [14, 80]. The reported centrality dependence at the LHC is in quantitative agreement

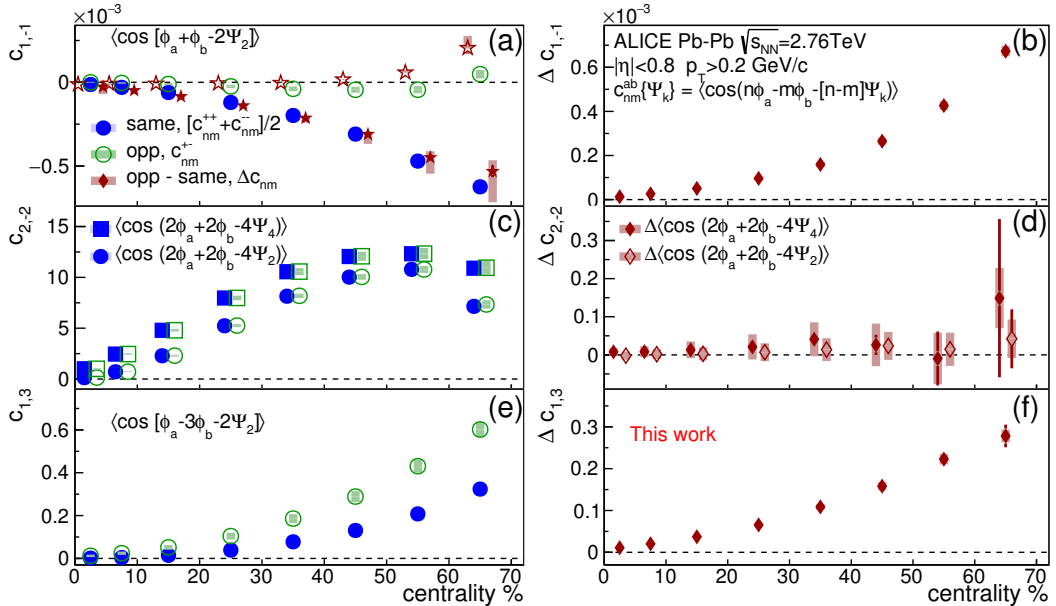


Figure 4.10: Centrality dependence of the correlation (a) $\langle \cos(\varphi_a + \varphi_b - 2\Psi_2) \rangle$, (b) $\langle \cos(2\varphi_a + 2\varphi_b - 4\Psi_4) \rangle$ and $\langle \cos(2\varphi_a + 2\varphi_b - 4\Psi_4) \rangle$, and (c) $\langle \cos(\varphi_a - 3\varphi_b + 2\Psi_2) \rangle$. The correlation $\langle \cos(\varphi_a + \varphi_b - 2\Psi_2) \rangle$ is compared to the RHIC data (star symbols) [26, 29]. The difference of the charge dependence (Eq. 4.13) is shown in panels (b,d,f).

with measurements at lower RHIC energies (i.e. Au–Au collisions at $\sqrt{s_{\text{NN}}} = 200$ GeV). This apparent collision energy independence of $\langle \cos(\varphi_a + \varphi_b - 2\Psi_2) \rangle$ can put stringent constraints on the possible mechanisms responsible for the strong charge dependent signal that develops for more peripheral events. Model calculations [63], based on extrapolation to the LHC energies assuming that the CME accounts for the whole signal measured at RHIC, predicted about 5 times smaller magnitude compared to that shown in Fig. 4.9(a). Dipole-like initial energy fluctuations [69, 81–84] which are expected to result in non-zero directed flow v_1 at midrapidity may also contribute to the charge independent part of the correlations shown in Fig. 4.10-(a).

To further study the relative contribution from various physics phenomena to $\langle \cos(\varphi_a + \varphi_b - 2\Psi_2) \rangle$ it was suggested [85] to investigate the second harmonic of the two particle correlation relative to the collision symmetry plane, $\langle \cos(2\varphi_a + 2\varphi_b - 4\Psi_4) \rangle$. The CME should not contribute to the charge dependence in this measurement and it can be used to experimentally constrain the contribution from effects which constitute the background, such as local charge conservation. According to Eq. (4.15) effects of local charge conservation to leading order approximation should scale with the magnitude of anisotropic flow, and compared to $\langle \cos(2\varphi_a + 2\varphi_b - 4\Psi_4) \rangle$ their contribution should be reduced in $\langle \cos(\varphi_a + \varphi_b - 2\Psi_2) \rangle$ proportionally to the v_4/v_2 ratio.

Figure 4.10(c) shows the centrality dependence of $\langle \cos(2\varphi_a + 2\varphi_b - 4\Psi_4) \rangle$ for different charge combinations. Additionally $\langle \cos(2\varphi_a + 2\varphi_b - 4\Psi_2) \rangle$ is shown, which provides a measurement of the second harmonic of the two particle correlation with respect to the second order collision symmetry plane. The charge independent correlations are strong and statistically significant (and reflects large contribution from v_2 and v_4 [86]), and the statistical precision of the measurements for the charge dependent part in Fig. 4.10(d) is consistent with zero within the systematic uncertainty. These can be used to calculate a constraint on the possible contribution from effects of local charge conservation.

4.5.3 Mixed harmonic correlation with the first moment relative to Ψ_n

Figure 4.10(e) presents the first order mixed harmonic correlations $\langle \cos(\varphi_a - 3\varphi_b + 2\Psi_2) \rangle$. Similar to results in Fig. 4.9 the opposite sign pair correlation is stronger than that measured for the same sign pairs. Results in Fig. 4.10 provide information about the contributions from higher order harmonics to the shape of the two particle correlations. The charge independent part of $\langle \cos(\varphi_a - 3\varphi_b + 2\Psi_2) \rangle$ is sensitive to the dipole-like energy fluctuations which are expected to result in a correlation between the first and third harmonics [69].

Figure 4.10(f) shows the charge dependent part of the correlations shown in Fig. 4.10(e).

4.5.4 Moments of the two particle correlation differentially

Further information about the correlations can be learned from studying various kinematic dependencies. Figure 4.11 shows charge dependent correlations $\langle \cos(\varphi_a - \varphi_b) \rangle$, $\langle \cos(\varphi_a + \varphi_b - 2\Psi_2) \rangle$, and $\langle \cos(\varphi_a - 3\varphi_b + 2\Psi_2) \rangle$ as a function of centrality in two different intervals of the relative transverse momentum $\Delta p_T = |p_{T,a} - p_{T,b}|$ and average $\langle p_T \rangle = (p_{T,a} + p_{T,b})/2$ pair transverse momentum, and pair separation in pseudorapidity $\Delta\eta = |\eta_a - \eta_b|$

The correlations of $\langle \cos(\varphi_a + \varphi_b - 2\Psi_2) \rangle$, and $\langle \cos(\varphi_a - 3\varphi_b + 2\Psi_2) \rangle$ as a function of pseudorapidity separation $\Delta\eta$ are localized within one unit and may even change sign for large values of $\Delta\eta$. The magnitude of these correlations as a function of $\langle p_T \rangle$ extends above 2 GeV/c which is

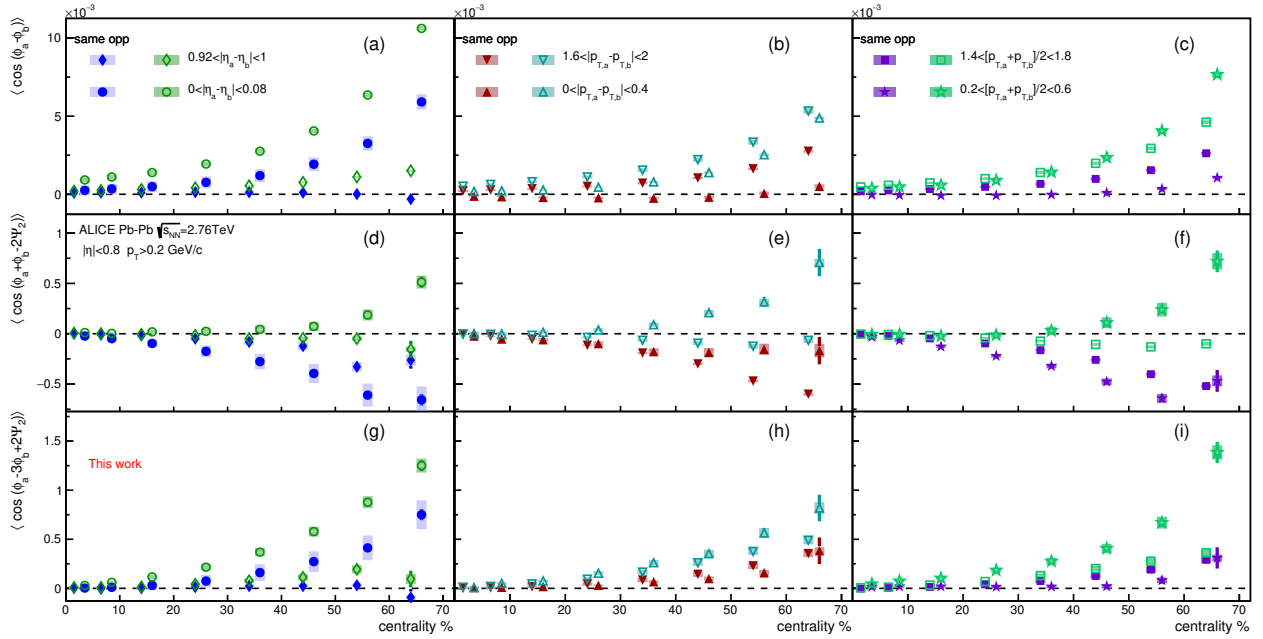


Figure 4.11: (a-c) Correlations $\langle \cos(\varphi_a - \varphi_b) \rangle$, (d-f) $\langle \cos(\varphi_a + \varphi_b - 2\Psi_2) \rangle$, (g-i) $\langle \cos(\varphi_a - 3\varphi_b + 2\Psi_2) \rangle$ as a function of centrality for different intervals of the relative $|p_{T,a} - p_{T,b}|$ and average $(p_{T,a} + p_{T,b})/2$ pair transverse momentum, and pair separation in pseudorapidity $\Delta\eta = |\eta_a - \eta_b|$.

not what one would naively expect for the CME. This can be an effect of the radial flow. Effects of local charge conservation are expected to have a narrow width (smaller signal) at higher p_T due to focusing of the balancing pairs [37, 66]. Figure 4.12 shows the differential correlations for three centrality intervals where the relative magnitude is shown with respect to centrality integrated results. It is interesting to see that the change in the shapes is small for the different centrality ranges.

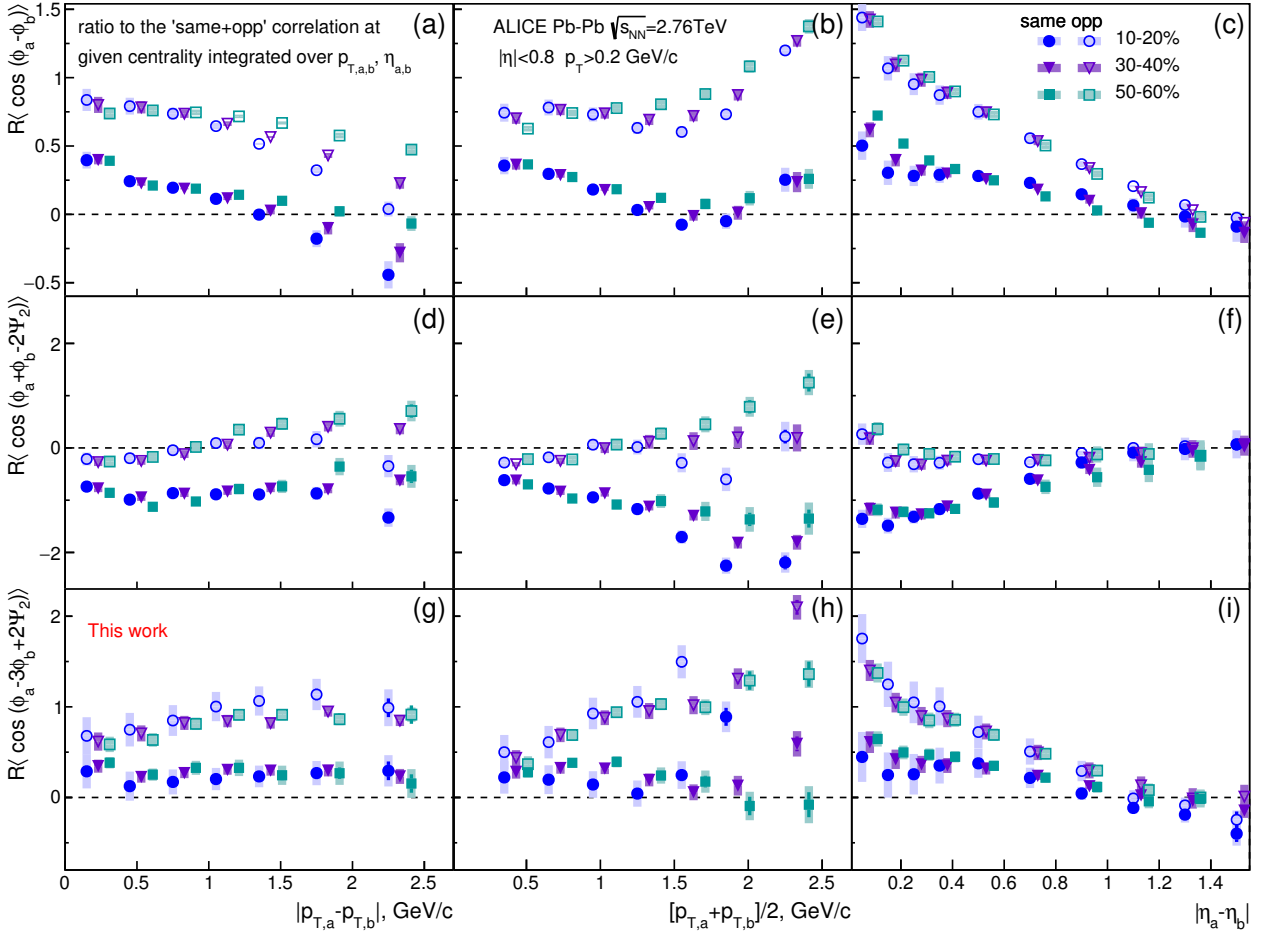


Figure 4.12: (a-c) Relative magnitude of correlations $\langle \cos(\varphi_a - \varphi_b) \rangle$, (d-f) $\langle \cos(\varphi_a + \varphi_b - 2\Psi_2) \rangle$, (g-i) $\langle \cos(\varphi_a - 3\varphi_b + 2\Psi_2) \rangle$ as a function of centrality for different intervals of the relative $|p_{T,a} - p_{T,b}|$ and average $(p_{T,a} + p_{T,b})/2$ pair transverse momentum, and pair separation in pseudorapidity $\Delta\eta = |\eta_a - \eta_b|$.

4.5.5 Three particle correlation with identified particles

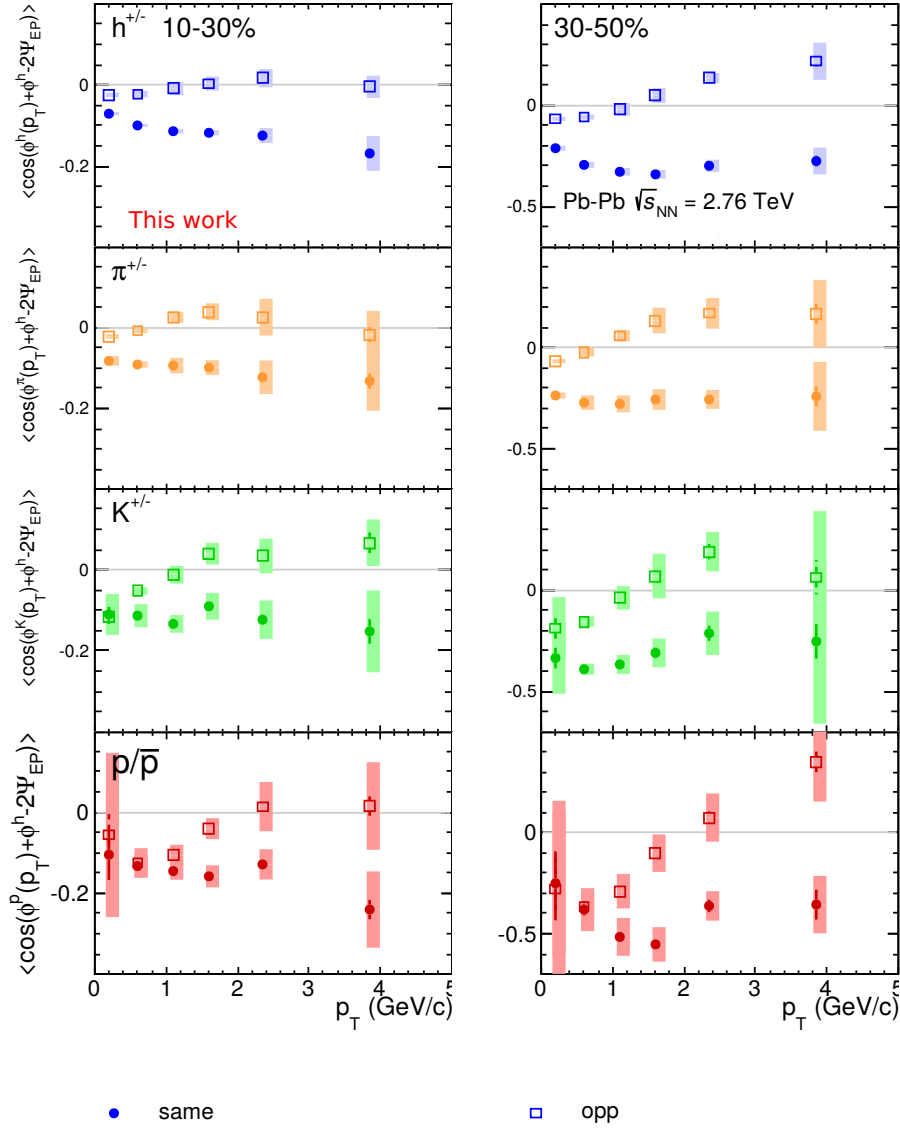


Figure 4.13: $\langle \cos(\phi^{PID}(p_T) + \phi^h - 2\Psi_{2,EP}) \rangle$ in centrality bins 10-30% and 30-50%.

In the measurement a dependency of the charge dependent three particle correlation on the particle species is observed. The pion-hadron opposite and same sign combinations have a large separation starting at low p_T , however the kaons and proton charge combinations are close together and start to deviate towards higher p_T . The opposite sign correlations cross or approach zero at higher p_T in order with the mass of the identified particle. A comparison to models, for example blast-wave, could help to provide insight in the observed correlations.

In Fig. 4.14 the correlation Equation 4.9 is shown for the 10-30% and 30-50% centrality range. The different charge combinations of correlated particle pairs are combined in $\alpha = \beta$ (same) and $\alpha = -\beta$ (opp.) charge pairs. For the proton correlation at $p_T < 1$ GeV/c only anti-protons are used in order to avoid contamination from knock-out protons from detector material. The trends for hadron, pion, kaon and proton correlations for like-sign and unlike-

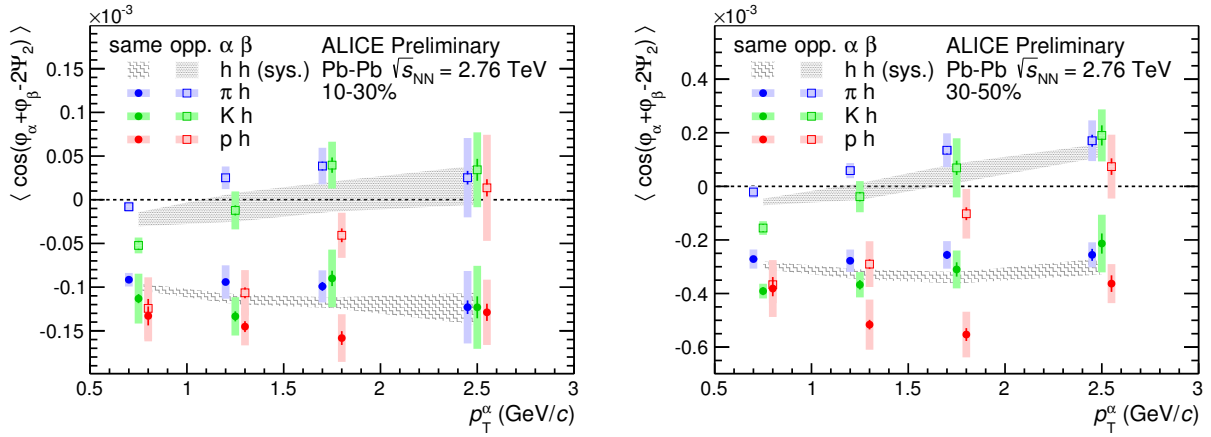


Figure 4.14: Results [87] for $c_{\alpha\beta}^{ij}$ defined in Equation 4.9 in the 10-30% (left) and the 30-50% (right) centrality range. The fine hatched areas show the unlike-sign hadron correlation and the coarse hatched areas the like-sign hadron correlation. The unlike-sign correlations for identified hadrons are shown in open squares, and the like-sign correlations in full squares. Pions are shown in blue, kaons in green, and protons in red. The systematic error is indicated with the colored bands.

sign are similar in both centrality ranges, while the magnitude of the observed correlations are approximately three times stronger in more peripheral collisions. A clear particle species dependence is observed in the unlike-sign correlations, which is close to zero for pions, but increases towards negative values at low transverse momentum for kaons and protons. The like-sign correlations do not have a significant slope as a function of p_T . Although an ordering appears from pions to protons in the magnitude of the correlations, the differences are not significant as for the unlike-sign correlations.

4.6 Summary

A new set of charge dependent azimuthal correlations was measured in Pb–Pb collisions at $\sqrt{s_{NN}} = 2.76$ TeV. The measurements provide detailed information about the shape of the two particle azimuthal correlations relative to the collision symmetry planes. This is an important experimental input for theoretical modeling of charge dependent azimuthal correlations observed in a heavy-ion collision at RHIC and LHC energies. In particular, the measurements provide additional constraints on the possible contribution due to the chiral magnetic effect, effects of the local charge conservation, and fluctuating initial energy profile. The complexity of the differential dependencies measured for these correlations demands realistic modeling of all expected contributions before any conclusion can be made about the origin of these correlations and sensitivity in the data to the CME.

In addition a new charge dependent measurement with identified particles is presented. The charge dependent correlation $\langle \cos(\varphi_\alpha^i(p_T) + \varphi_\beta^j - 2\Psi_{RP}) \rangle$ is measured with a charged pion, kaon or proton (i) and an unidentified charged hadron (j). In the opposite sign correlations a significant dependence on particle species is observed at low p_T . This new result signals that effects contributing to the previously observed charge separation with unidentified hadrons have a different contribution depending on particle species. Model calculations, in particular of the local

charge conservation with identified particles, and further measurements are required to quantify and describe the observed charge separation effects, and achieve a detailed understanding of the charge dependent correlations and possible contributions from CME.



5 Conclusions and outlook

In this work a framework for corrections for the measurement of Q -vectors in detectors with non-uniform azimuthal acceptance was presented, and measurements of charge-dependent correlations in Pb–Pb collisions at $\sqrt{s_{\text{NN}}} = 2.76$ TeV with ALICE at the LHC were made.

The measurement of collision symmetry planes and related observables can be affected by non-uniform azimuthal detector acceptance. To correct for the resulting effects a correction procedure was developed that is based on the recentering, twist and rescaling corrections proposed by Selyuzhenkov and Voloshin [51]. The implemented procedure requires the presence of a tracking detector, and was expanded with corrections for gain equalization and detector alignment. The correction framework is available as a ROOT-based software package [53] that has general applicability to data from heavy ion experiments. The framework is highly configurable, allowing users to define the specific set of subevents and corrections they require, after which a number of iterations is required to extract correction parameters and apply corrections to data. The resulting corrected Q -vectors can be used for symmetry plane related analyses. A study with a toy model was presented where particles were generated with a ν_2 modulated distribution for a group of subevents that reflect a setup similar to ALICE (with a particle tracking detector and two segmented multiplicity detectors), with introduced non-uniform acceptance effects. After the corrections the magnitude of the input ν_2 was accurately reconstructed. The effect of the corrections, especially for twist and rescaling, deserve closer scrutiny for detector setups without a close to uniform central tracker. The software framework was used to apply corrections to ALICE data, from which the resolution correction parameter R_2 and flow ν_2 were measured using a large group of subevents (TPC, V0, T0 and FMD). Corrections for alignment, twist and rescaling were found to be negligible for these measurements. The results demonstrate that ν_2 can be extracted within a systematic uncertainty of 4% depending on event centrality. The existing differences are qualitatively in line with expectations from [48], where detectors with low R_n are more sensitive to flow fluctuations, leading to a slightly higher measured value of $\langle \nu_n \rangle$.

Measurements are presented of charge-dependent correlations in the context of the search for the Chiral Magnetic Effect (CME). The correlations with different sensitivity to CME and background effects show varying degrees of charge separation. The $\langle \cos(\varphi_\alpha + \varphi_\beta - 2\Psi_{\text{RP}}) \rangle$ correlator proposed by Voloshin, with maximum sensitivity to charge separation along the magnetic field (perpendicular to the reaction plane), shows a charge dependence increasing towards peripheral events, as is qualitatively in line with expectations. The second harmonic of this correlator was suggested as a method to estimate the contribution from background correlations, which can be caused for example by clusters of particles exhibiting charge conservation with angular correlations modulated by anisotropic flow. The measurement is consistent with zero within systematic uncertainty, but may be used to estimate an upper limit on the background contribution. Measurements with higher statistics and model comparisons are required to make a more quantitative conclusion about the contributions from background sources in the observation of charge observation of the main CME correlator.

Measurements of the CME correlator with pions, kaons and protons as a function of transverse momentum reveal a particle type dependence in the charge-dependent correlations. Charge separation due to CME may result in a particle type dependence for hadrons because of the different quark content [88], which in turn can be affected by the presence of CME. However there is also a known dependence of anisotropic flow on particle species in azimuthal correlations. To understand these contributions and effects in more detail, accurate models are required for definite conclusions.

Further studies for the presented topics can be suggested. For the Q-vector corrections, the impact of non-flow and multiplicity fluctuations, as well as the interdependence of different flow harmonics limits the effectiveness of the calculation and application of the developed corrections. Furthermore the proposed solutions to the equations involves the presence of at least one tracking detector. A more general solution is in principle possible. The developed software package is designed to easily incorporate new corrections, such that continued improvement is encouraged.

The study of CME that was presented can be further expanded. Previously the CME correlator was already studied with the STAR beam energy scan, as well as for different collision systems. Shortly before this document was submitted CMS presented a measurement in p-Pb collisions [89]. An additional method of interest is to use event-shape-engineering (ESE) to select the event shape and measure charge-dependent correlations for fixed beam parameter but varying magnitude of anisotropic flow. This will allow to probe the contribution of background sources, which are modulated by anisotropic flow, to the measured correlations. In the limit where for a semicentral event $v_2 \rightarrow 0$, but the magnetic field is still large, the contributions from anisotropic flow become zero. The remaining correlation could provide evidence for CME. The \mathcal{CP} -violation in strong interactions can also lead to other effects than CME that may be measured in heavy ion collisions. Studies related to the Chiral Magnetic Wave were published by STAR and ALICE. Searches for the Chiral Vortical Effect, which leads to baryon-charge separation, were proposed [90]. Furthermore on the theoretical and phenomenological side, development of more accurate calculations and models can lead to more quantitative comparisons to the various existing measurements of charge-dependent correlations. Recently hydrodynamical studies including anomalous effects were presented [88, 91]. These developments are crucial to determine that existing and future measurements contain evidence of \mathcal{CP} -conservation in strong interactions.

6 Appendix

6.1 Run list

Analyzed data set: LHC10h.

Number of events: ~ 13 million.

Collision system: Pb–Pb at $\sqrt{s_{\text{NN}}} = 2.76$ TeV.

Data format: ESD.

Run list: 137161, 137162, 137231, 137232, 137235, 137236, 137243, 137366, 137431, 137432, 137434, 137439, 137440, 137441, 137443, 137530, 137531, 137539, 137541, 137544, 137546, 137549, 137595, 137608, 137638, 137639, 137685, 137686, 137691, 137692, 137693, 137704, 137718, 137722, 137724, 137751, 137752, 137844, 137848, 138190, 138192, 138197, 138201, 138225, 138275, 138364, 138396, 138438, 138439, 138442, 138469, 138534, 138578, 138579, 138582, 138583, 138621, 138624, 138638, 138652, 138653, 138662, 138666, 138730, 138732, 138837, 138870, 138871, 138872, 139028, 139029, 139036, 139037, 139038, 139105, 139107, 139173, 139309, 139310, 139314, 139328, 139329, 139360, 139437, 139438, 139465, 139503, 139505, 139507, 139510.



Bibliography

- [1] J. W. Rohlf, *Modern Physics from α to Z^0* . 1994.
- [2] **Particle Data Group** Collaboration, K. A. Olive *et al.*, “Review of Particle Physics,” *Chin. Phys.* **C38** (2014) 090001.
- [3] U. M. Heller, “Recent progress in finite temperature lattice QCD,” *PoS LAT2006* (2006) 011, arXiv:hep-lat/0610114 [hep-lat].
- [4] L. Nuclear Science Division, *Teacher’s Guide to the Nuclear Science*.
<http://www2.lbl.gov/abc/>.
- [5] R. P. Feynman, R. B. Leighton, and M. Sands, *The Feynman Lectures on Physics*. 1963.
<http://www.feynmanlectures.info/>.
- [6] E. Noether, “Invariant Variation Problems,” *Gott. Nachr.* **1918** (1918) 235–257,
arXiv:physics/0503066 [physics]. [Transp. Theory Statist. Phys.1,186(1971)].
- [7] T. D. Lee and C.-N. Yang, “Question of Parity Conservation in Weak Interactions,” *Phys. Rev.* **104** (1956) 254–258.
- [8] C. S. Wu, E. Ambler, R. W. Hayward, D. D. Hoppes, and R. P. Hudson, “Experimental Test of Parity Conservation in Beta Decay,” *Phys. Rev.* **105** (1957) 1413–1414.
- [9] J. H. Christenson, J. W. Cronin, V. L. Fitch, and R. Turlay, “Evidence for the 2π decay of the k_2^0 meson,” *Phys. Rev. Lett.* **13** (Jul, 1964) 138–140.
<https://link.aps.org/doi/10.1103/PhysRevLett.13.138>.
- [10] **LHCb** Collaboration, R. Aaij *et al.*, “Search for the CP -violating strong decays $\eta \rightarrow \pi^+ \pi^-$ and $\eta'(958) \rightarrow \pi^+ \pi^-$,” arXiv:1610.03666 [hep-ex].
- [11] G. ’t Hooft, “Symmetry Breaking Through Bell-Jackiw Anomalies,” *Phys. Rev. Lett.* **37** (1976) 8–11.
- [12] G. ’t Hooft, “Computation of the Quantum Effects Due to a Four-Dimensional Pseudoparticle,” *Phys. Rev.* **D14** (1976) 3432–3450. [Erratum: *Phys. Rev.* **D18**,2199(1978)].
- [13] R. Jackiw and C. Rebbi, “Vacuum Periodicity in a Yang-Mills Quantum Theory,” *Phys. Rev. Lett.* **37** (1976) 172–175.
- [14] D. E. Kharzeev, L. D. McLerran, and H. J. Warringa, “The Effects of topological charge change in heavy ion collisions: ’Event by event P and CP violation’,” *Nucl. Phys.* **A803** (2008) 227–253, arXiv:0711.0950 [hep-ph].
- [15] L. Wei, *Research interests*. <http://wl33.web.rice.edu/research.html>.

-
- [16] S. Shi, *Event anisotropy v_2 at STAR*. 2010.
https://drupal.star.bnl.gov/STAR/files/PhD_Thesis_ShusuShi.pdf.
- [17] F. Gelis, “The Early Stages of a High Energy Heavy Ion Collision,” *J. Phys. Conf. Ser.* **381** (2012) 012021, arXiv:1110.1544 [hep-ph].
- [18] P. F. Kolb and U. W. Heinz, “Hydrodynamic description of ultrarelativistic heavy ion collisions,” arXiv:nucl-th/0305084 [nucl-th].
- [19] ALICE Collaboration, K. Aamodt *et al.*, “Elliptic flow of charged particles in Pb-Pb collisions at 2.76 TeV,” *Phys. Rev. Lett.* **105** (2010) 252302, arXiv:1011.3914 [nucl-ex].
- [20] ALICE Collaboration, B. B. Abelev *et al.*, “Elliptic flow of identified hadrons in Pb-Pb collisions at $\sqrt{s_{NN}} = 2.76$ TeV,” *JHEP* **06** (2015) 190, arXiv:1405.4632 [nucl-ex].
- [21] V. Skokov, A. Yu. Illarionov, and V. Toneev, “Estimate of the magnetic field strength in heavy-ion collisions,” *Int. J. Mod. Phys. A* **24** (2009) 5925–5932, arXiv:0907.1396 [nucl-th].
- [22] V. Voronyuk, V. D. Toneev, W. Cassing, E. L. Bratkovskaya, V. P. Konchakovski, and S. A. Voloshin, “(Electro-)Magnetic field evolution in relativistic heavy-ion collisions,” *Phys. Rev. C* **83** (2011) 054911, arXiv:1103.4239 [nucl-th].
- [23] A. Bzdak and V. Skokov, “Anisotropy of photon production: initial eccentricity or magnetic field,” *Phys. Rev. Lett.* **110** no. 19, (2013) 192301, arXiv:1208.5502 [hep-ph].
- [24] STAR Collaboration, L. Adamczyk *et al.*, “Observation of charge asymmetry dependence of pion elliptic flow and the possible chiral magnetic wave in heavy-ion collisions,” *Phys. Rev. Lett.* **114** no. 25, (2015) 252302, arXiv:1504.02175 [nucl-ex].
- [25] STAR Collaboration, L. Adamczyk *et al.*, “Measurement of Charge Multiplicity Asymmetry Correlations in High Energy Nucleus-Nucleus Collisions at 200 GeV,” arXiv:1303.0901 [nucl-ex].
- [26] STAR Collaboration, B. Abelev *et al.*, “Azimuthal Charged-Particle Correlations and Possible Local Strong Parity Violation,” *Phys. Rev. Lett.* **103** (2009) 251601, arXiv:0909.1739 [nucl-ex].
- [27] K. Hattori and X.-G. Huang, “Novel quantum phenomena induced by strong magnetic fields in heavy-ion collisions,” arXiv:1609.00747 [nucl-th].
- [28] S. A. Voloshin, “Parity violation in hot QCD: How to detect it,” *Phys. Rev. C* **70** (2004) 057901, arXiv:hep-ph/0406311 [hep-ph].
- [29] STAR Collaboration, B. Abelev *et al.*, “Observation of charge-dependent azimuthal correlations and possible local strong parity violation in heavy ion collisions,” *Phys. Rev. C* **81** (2010) 054908, arXiv:0909.1717 [nucl-ex].
- [30] ALICE Collaboration, B. Abelev *et al.*, “Charge separation relative to the reaction plane in Pb-Pb collisions at $\sqrt{s_{NN}} = 2.76$ TeV,” *Phys. Rev. Lett.* **110** (2013) 012301, arXiv:1207.0900 [nucl-ex].

-
- [31] **STAR** Collaboration, L. Adamczyk *et al.*, “Fluctuations of charge separation perpendicular to the event plane and local parity violation in $\sqrt{s_{NN}} = 200$ GeV Au+Au collisions at RHIC,” arXiv:1302.3802 [nucl-ex].
- [32] **STAR** Collaboration, L. Adamczyk *et al.*, “Beam-energy dependence of charge separation along the magnetic field in Au+Au collisions at RHIC,” *Phys. Rev. Lett.* **113** (2014) 052302, arXiv:1404.1433 [nucl-ex].
- [33] F. Wang, “Effects of Cluster Particle Correlations on Local Parity Violation Observables,” *Phys. Rev.* **C81** (2010) 064902, arXiv:0911.1482 [nucl-ex].
- [34] S. Pratt, S. Schlichting, and S. Gavin, “Effects of Momentum Conservation and Flow on Angular Correlations at RHIC,” *Phys. Rev.* **C84** (2011) 024909, arXiv:1011.6053 [nucl-th].
- [35] A. Bzdak, V. Koch, and J. Liao, “Remarks on possible local parity violation in heavy ion collisions,” *Phys. Rev.* **C81** (2010) 031901, arXiv:0912.5050 [nucl-th].
- [36] A. Bzdak, V. Koch, and J. Liao, “Charge-Dependent Correlations in Relativistic Heavy Ion Collisions and the Chiral Magnetic Effect,” *Lect. Notes Phys.* **871** (2013) 503–536, arXiv:1207.7327 [nucl-th].
- [37] S. Schlichting and S. Pratt, “Charge conservation at energies available at the BNL Relativistic Heavy Ion Collider and contributions to local parity violation observables,” *Phys. Rev.* **C83** (2011) 014913, arXiv:1009.4283 [nucl-th].
- [38] S. A. Bass, P. Danielewicz, and S. Pratt, “Clocking hadronization in relativistic heavy ion collisions with balance functions,” *Phys. Rev. Lett.* **85** (2000) 2689–2692, arXiv:nucl-th/0005044 [nucl-th].
- [39] **ALICE** Collaboration, B. Abelev *et al.*, “Charge correlations using the balance function in Pb-Pb collisions at $\sqrt{s_{NN}} = 2.76$ TeV,” arXiv:1301.3756 [nucl-ex].
- [40] **CMS** Collaboration, S. Chatrchyan *et al.*, “Observation of a new boson at a mass of 125 GeV with the CMS experiment at the LHC,” *Phys. Lett.* **B716** (2012) 30–61, arXiv:1207.7235 [hep-ex].
- [41] **ATLAS** Collaboration, G. Aad *et al.*, “Observation of a new particle in the search for the Standard Model Higgs boson with the ATLAS detector at the LHC,” *Phys. Lett.* **B716** (2012) 1–29, arXiv:1207.7214 [hep-ex].
- [42] **ALICE** Collaboration, B. B. Abelev *et al.*, “Performance of the ALICE Experiment at the CERN LHC,” *Int. J. Mod. Phys.* **A29** (2014) 1430044, arXiv:1402.4476 [nucl-ex].
- [43] **ALICE** Collaboration, J. Adam *et al.*, “Particle identification in ALICE: a Bayesian approach,” *Eur. Phys. J. Plus* **131** no. 5, (2016) 168, arXiv:1602.01392 [physics.data-an].
- [44] J. Schukraft, A. Timmins, and S. A. Voloshin, “Ultra-relativistic nuclear collisions: event shape engineering,” *Phys. Lett.* **B719** (2013) 394–398, arXiv:1208.4563 [nucl-ex].

-
- [45] ALICE Collaboration, A. Dobrin, “Event shape engineering with ALICE,” *Nucl. Phys.* **A904-905** (2013) 455c–458c, arXiv:1211.5348 [nucl-ex].
- [46] Z. Qiu and U. Heinz, “Hydrodynamic event-plane correlations in Pb+Pb collisions at $\sqrt{s} = 2.76$ ATeV,” *Phys. Lett.* **B717** (2012) 261–265, arXiv:1208.1200 [nucl-th].
- [47] R. S. Bhalerao, J.-Y. Ollitrault, and S. Pal, “Event-plane correlators,” *Phys. Rev.* **C88** (2013) 024909, arXiv:1307.0980 [nucl-th].
- [48] M. Luzum and J.-Y. Ollitrault, “The event-plane method is obsolete,” arXiv:1209.2323 [nucl-ex].
- [49] N. Borghini, P. M. Dinh, and J.-Y. Ollitrault, “Flow analysis from multiparticle azimuthal correlations,” *Phys. Rev.* **C64** (2001) 054901, arXiv:nucl-th/0105040 [nucl-th].
- [50] A. Bilandzic, R. Snellings, and S. Voloshin, “Flow analysis with cumulants: Direct calculations,” *Phys. Rev.* **C83** (2011) 044913, arXiv:1010.0233 [nucl-ex].
- [51] I. Selyuzhenkov and S. Voloshin, “Effects of non-uniform acceptance in anisotropic flow measurement,” *Phys. Rev.* **C77** (2008) 034904, arXiv:0707.4672 [nucl-th].
- [52] R. Brun and F. Rademakers, “ROOT – an object oriented data analysis framework,” *Nucl. Inst. & Meth. in Phys. Res. A* **389** no. 1, (1997) 81 – 86. <http://root.cern.ch/>.
- [53] Flow vector correction framework, available under GNU General Public License v.3. <https://github.com/FlowCorrections/FlowVectorCorrections>.
- [54] K. Grosse, ed., *GSI Scientific Report 2015*. GSI, Darmstadt, 2016. <https://repository.gsi.de/record/189686>.
- [55] ALICE Collaboration, “The ALICE off-line project,” <http://alice-offline.web.cern.ch/>.
- [56] ALICE Collaboration, E. Abbas *et al.*, “Centrality dependence of the pseudorapidity density distribution for charged particles in Pb-Pb collisions at $\sqrt{s_{NN}} = 2.76$ TeV,” *Phys. Lett.* **B726** (2013) 610–622, arXiv:1304.0347 [nucl-ex].
- [57] A. M. Poskanzer and S. Voloshin, “Methods for analyzing anisotropic flow in relativistic nuclear collisions,” *Phys. Rev.* **C58** (1998) 1671–1678, arXiv:nucl-ex/9805001 [nucl-ex].
- [58] D. Kharzeev, “Parity violation in hot QCD: Why it can happen, and how to look for it,” *Phys. Lett.* **B633** (2006) 260–264, arXiv:hep-ph/0406125 [hep-ph].
- [59] D. E. Kharzeev and H.-U. Yee, “Anomalies and time reversal invariance in relativistic hydrodynamics: the second order and higher dimensional formulations,” *Phys. Rev.* **D84** (2011) 045025, arXiv:1105.6360 [hep-th].
- [60] S.-Q. Feng, L. Pei, F. Sun, Y. Zhong, and Z.-B. Yin, “Study of the correlation of charge separation of the chiral magnetic effect in Relativistic Heavy-ion Collisions,” arXiv:1609.07550 [nucl-th].

-
- [61] L. Foa, “Inclusive Study of High-Energy Multiparticle Production and Two-Body Correlations,” *Phys.Rept.* **22** (1975) 1–56.
- [62] A. R. Zhitnitsky, “P and CP Violation and New Thermalization Scenario in Heavy Ion Collisions,” *Nucl. Phys.* **A853** (2011) 135–163, arXiv:1008.3598 [nucl-th].
- [63] V. Toneev and V. Voronyuk, “The Chiral Magnetic Effect: Beam-energy and system-size dependence,” *Phys. Atom. Nucl.* **75** (2012) 607–612, arXiv:1012.1508 [nucl-th].
- [64] S. Cheng, S. Petriconi, S. Pratt, M. Skoby, C. Gale, *et al.*, “Statistical and dynamic models of charge balance functions,” *Phys. Rev.* **C69** (2004) 054906, arXiv:nucl-th/0401008 [nucl-th].
- [65] S. Pratt, “General Charge Balance Functions, A Tool for Studying the Chemical Evolution of the Quark-Gluon Plasma,” *Phys. Rev.* **C85** (2012) 014904, arXiv:1109.3647 [nucl-th].
- [66] S. Schlichting and S. Pratt, “Effects of Charge Conservation and Flow on Fluctuations of parity-odd Observables at RHIC,” arXiv:1005.5341 [nucl-th].
- [67] Y. Hori, T. Gunji, H. Hamagaki, and S. Schlichting, “Collective flow effects on charge balance correlations and local parity-violation observables in $\sqrt{s_{NN}} = 2.76$ TeV Pb+Pb collisions at the LHC,” arXiv:1208.0603 [nucl-th].
- [68] V. Skokov, P. Sorensen, V. Koch, S. Schlichting, J. Thomas, S. Voloshin, G. Wang, and H.-U. Yee, “Chiral Magnetic Effect Task Force Report,” arXiv:1608.00982 [nucl-th].
- [69] D. Teaney and L. Yan, “Triangularity and Dipole Asymmetry in Heavy Ion Collisions,” *Phys. Rev.* **C83** (2011) 064904, arXiv:1010.1876 [nucl-th].
- [70] Z.-T. Liang and X.-N. Wang, “Globally polarized quark-gluon plasma in non-central A+A collisions,” *Phys. Rev. Lett.* **94** (2005) 102301, arXiv:nucl-th/0410079 [nucl-th].
- [71] S. A. Voloshin, “Polarized secondary particles in unpolarized high energy hadron-hadron collisions?,” arXiv:nucl-th/0410089 [nucl-th].
- [72] **STAR** Collaboration, B. Abelev *et al.*, “Global polarization measurement in Au+Au collisions,” *Phys. Rev.* **C76** (2007) 024915, arXiv:0705.1691 [nucl-ex].
- [73] S. A. Voloshin, A. M. Poskanzer, and R. Snellings, “Collective phenomena in non-central nuclear collisions,” arXiv:0809.2949 [nucl-ex].
- [74] N. Borghini, P. M. Dinh, and J.-Y. Ollitrault, “A New method for measuring azimuthal distributions in nucleus-nucleus collisions,” *Phys. Rev.* **C63** (2001) 054906, arXiv:nucl-th/0007063 [nucl-th].
- [75] N. Borghini, P. M. Dinh, and J.-Y. Ollitrault, “Flow analysis from cumulants: A Practical guide,” arXiv:nucl-ex/0110016 [nucl-ex].
- [76] **ALICE** Collaboration, K. Aamodt *et al.*, “Centrality dependence of the charged-particle multiplicity density at mid-rapidity in Pb-Pb collisions at $\sqrt{s_{NN}} = 2.76$ TeV,” *Phys. Rev. Lett.* **106** (2011) 032301, arXiv:1012.1657 [nucl-ex].

-
- [77] Y. Hori, *Mixed harmonic azimuthal correlations in $\sqrt{s_{NN}} = 2.76$ TeV Pb-Pb collisions measured by ALICE at LHC*. PhD thesis, Tokyo U., 2013-03-25.
<https://inspirehep.net/record/1231061/files/CERN-THESIS-2013-021.pdf>.
- [78] ALICE Collaboration, B. Abelev *et al.*, “Anisotropic flow of charged hadrons, pions and (anti-)protons measured at high transverse momentum in Pb-Pb collisions at $\sqrt{s_{NN}} = 2.76$ TeV,” arXiv:1205.5761 [nucl-ex].
- [79] ALICE Collaboration, R. Preghenella, “Identified-particle production and spectra with the ALICE detector in pp and Pb-Pb collisions at the LHC,” *Acta Phys. Polon.* **B43** (2012) 555, arXiv:1111.7080 [hep-ex].
- [80] K. Fukushima, D. E. Kharzeev, and H. J. Warringa, “The Chiral Magnetic Effect,” *Phys. Rev.* **D78** (2008) 074033, arXiv:0808.3382 [hep-ph].
- [81] F. G. Gardim, F. Grassi, M. Luzum, and J.-Y. Ollitrault, “Mapping the hydrodynamic response to the initial geometry in heavy-ion collisions,” *Phys. Rev.* **C85** (2012) 024908, arXiv:1111.6538 [nucl-th].
- [82] R. S. Bhalerao, M. Luzum, and J.-Y. Ollitrault, “Understanding anisotropy generated by fluctuations in heavy-ion collisions,” *Phys. Rev.* **C84** (2011) 054901, arXiv:1107.5485 [nucl-th].
- [83] R. Bhalerao, M. Luzum, and J. Ollitrault, “New flow observables,” *J. Phys.* **G38** (2011) 124055, arXiv:1106.4940 [nucl-ex].
- [84] R. S. Bhalerao, M. Luzum, and J.-Y. Ollitrault, “Determining initial-state fluctuations from flow measurements in heavy-ion collisions,” *Phys. Rev.* **C84** (2011) 034910, arXiv:1104.4740 [nucl-th].
- [85] S. A. Voloshin, “Collective phenomena in ultra-relativistic nuclear collisions: anisotropic flow and more,” *Prog. Part. Nucl. Phys.* **67** (2012) 541–546, arXiv:1111.7241 [nucl-ex].
- [86] STAR Collaboration, J. Adams *et al.*, “Azimuthal anisotropy at RHIC: The First and fourth harmonics,” *Phys. Rev. Lett.* **92** (2004) 062301, arXiv:nucl-ex/0310029 [nucl-ex].
- [87] ALICE Collaboration, J. Onderwaater, “Charge dependence of identified two-hadron correlation relative to the reaction plane in Pb-Pb collisions measured with ALICE,” *J. Phys. Conf. Ser.* **612** no. 1, (2015) 012044.
- [88] Y. Yin and J. Liao, “Hydrodynamics with chiral anomaly and charge separation in relativistic heavy ion collisions,” *Phys. Lett.* **B756** (2016) 42–46, arXiv:1504.06906 [nucl-th].
- [89] CMS Collaboration, V. Khachatryan *et al.*, “Observation of charge-dependent azimuthal correlations in pPb collisions and its implication for the search for the chiral magnetic effect,” arXiv:1610.00263 [nucl-ex].
- [90] D. E. Kharzeev and D. T. Son, “Testing the chiral magnetic and chiral vortical effects in heavy ion collisions,” *Phys. Rev. Lett.* **106** (2011) 062301, arXiv:1010.0038 [hep-ph].

-
- [91] Y. Hirono, T. Hirano, and D. E. Kharzeev, “The chiral magnetic effect in heavy-ion collisions from event-by-event anomalous hydrodynamics,” [arXiv:1412.0311 \[hep-ph\]](#).



List of Figures

1.1	The Standard Model of elementary particles.	8
1.2	Running of the strong coupling constant.	10
1.3	The QCD phase diagram.	11
1.4	Sketch of a relativistic heavy ion collision.	14
1.5	Different phases of heavy ion collision (left) and the early universe (right).	15
1.6	Two nuclei approaching with impact parameter b (left) and the spatially asymmetric overlap area in the transverse plane (right).	15
1.7	Simulation of the time evolution of the spatial and momentum anisotropy for Au–Au collisions at RHIC.	16
1.8	ε_2 versus impact parameter (left) and ν_2 versus collision centrality for Pb–Pb collisions at $\sqrt{s_{NN}} = 2.76$ TeV (right).	17
1.9	Identified particle ν_2 versus p_T (left) and versus $(m_T - m_0)/n_q$ (right).	17
1.10	Fourier coefficients ν_n as a function of centrality for $n = 2, 3, 4$ for Pb–Pb collisions at $\sqrt{s_{NN}} = 2.76$ TeV.	18
1.11	Time evolution of the magnetic field in heavy ion collisions (left) and values for the electric conductivity (right) at RHIC top energy for Au–Au collisions.	20
1.12	Strong magnetic field and non-zero topological charge leading to a charge current called the Chiral Magnetic Effect.	21
1.13	Charge dependence of $c_{\alpha\beta}$ versus centrality including STAR and HIJING.	22
1.14	Charge dependence of $c_{\alpha\beta}$ versus Δp_T , $\langle p_T \rangle$ and $\Delta\eta$	22
1.15	Beam energy dependence of the charge dependent correlation [32].	23
1.16	Measurement of the charge separation at STAR compared to a Blast-Wave model.	23
2.1	The CERN accelerator complex.	26
2.2	The ALICE detector.	27
2.3	Tracking efficiency in the TPC.	29
2.4	TPC dE/dx (left), TOF β (right) and the combined measurement (bottom).	31
2.5	Centrality estimation using V0 multiplicity (left) and ZDC energy (right).	35
2.6	R_2 for TPC, V0, FMD and PMD detectors (left) and for other (mixed) harmonics with V0 detector (right).	35
2.7	Measurement and selection of q_2 with the V0-A detector (left) and its impact on the measurement of ν_2 (right) [45].	36
3.1	Estimates of input ν_1 from simulated azimuthal angle distributions before and after different corrections.	46
3.2	Raw and calibrated V0 and T0 channel multiplicity distributions.	47
3.3	Raw and calibrated multiplicity distributions for one V0 and one T0 channel.	48
3.4	V0-A $q_{x,y}$ versus centrality before (top) and after (bottom) channel gain equalization.	49

3.5	T0-C $q_{x,y}$ versus centrality before (top) and after (bottom) channel gain equalization.	49
3.6	T0-A (left), V0-A (middle) and FMD-A (right) Q/M measurement before (top) and after (bottom) channel recentering.	50
3.7	Q -vector correlations between ring 4 of the V0-C and the TPC, before (left) and after (right) the alignment correction.	51
3.8	ν_2 with higher order corrections.	51
3.9	R_2 for TPC and A- and C-sides of the V0, T0, and FMD detectors calculated with the 3-subevent method.	52
3.10	ν_2 of charged particles estimated with event planes from A- and C- side V0, T0, and FMD detectors.	53
3.11	Resolution of the FMD with various sizes of η -gap as a ratio to the full FMD.	54
3.12	ν_2 results with T0-A(C)-V0-(C)A subevent correlations (left), and T0-A-T0-C (right).	55
4.1	Centrality and z -vertex distribution for the selected events.	62
4.2	ϕ -, η -, p_T - and $DCA_{x,y}$ distribution of tracks after track selection.	63
4.3	Centrality dependence of the correlations $\langle \cos(n[\varphi_a + \varphi_b - 2\varphi_c]) \rangle$ for $n = 1 - 3$, $\langle \cos(\varphi_a + n\varphi_b - (n + 1)\varphi_c) \rangle$ for $n = 2 - 5$, and $\langle \cos(2\varphi_a - n\varphi_b + (n - 1)\varphi_c) \rangle$ for $n = 3, 4$	64
4.4	Relative total systematic uncertainty for the same sign correlation $\langle \cos(\varphi_a + \varphi_b - 2\Psi_{RP}) \rangle$	65
4.5	Normalized ϕ -distribution of TPC and global tracks (left) and $DCA_{x,y}$ distribution with p_T -dependent DCA cuts (right).	65
4.6	TOF kaon- $n\sigma$ vs TPC kaon- $n\sigma$ for selected pions, kaons and protons.	66
4.7	TPC reconstruction efficiency vs p_T (left) and the rejection factor for flattening (right).	67
4.8	Weighted average of PID-hadron correlations compared to the hadron-hadron correlation.	69
4.9	$\langle \cos(n[\varphi_a - \varphi_b]) \rangle$ versus centrality for $n = 1 - 4$ (left) and the charge dependent difference of the correlations (right).	70
4.10	Centrality dependence of the correlation $\langle \cos(\varphi_a + \varphi_b - 2\Psi_2) \rangle$, $\langle \cos(2\varphi_a + 2\varphi_b - 4\Psi_4) \rangle$, $\langle \cos(2\varphi_a + 2\varphi_b - 4\Psi_4) \rangle$, and $\langle \cos(\varphi_a - 3\varphi_b + 2\Psi_2) \rangle$, and the difference of the charge dependence.	71
4.11	Correlations $\langle \cos(\varphi_a - \varphi_b) \rangle$, $\langle \cos(\varphi_a + \varphi_b - 2\Psi_2) \rangle$, $\langle \cos(\varphi_a - 3\varphi_b + 2\Psi_2) \rangle$ versus centrality for different intervals of $ p_{T,a} - p_{T,b} $, $(p_{T,a} + p_{T,b})/2$ and $\Delta\eta = \eta_a - \eta_b $	73
4.12	Relative magnitude of the correlations $\langle \cos(\varphi_a - \varphi_b) \rangle$, $\langle \cos(\varphi_a + \varphi_b - 2\Psi_2) \rangle$, $\langle \cos(\varphi_a - 3\varphi_b + 2\Psi_2) \rangle$ versus centrality for different intervals of $ p_{T,a} - p_{T,b} $, $(p_{T,a} + p_{T,b})/2$ and $\Delta\eta = \eta_a - \eta_b $	74
4.13	$\langle \cos(\phi^{PID}(p_T) + \phi^h - 2\Psi_{2,EP}) \rangle$ in centrality bins 10-30% and 30-50%.	75
4.14	$c_{\alpha\beta}^{ij}$ in the 10-30% (left) and the 30-50% (right) centrality range for charged hadrons, pions, kaons and protons.	76

List of Tables

1.1	The fundamental forces and their relative strength, force carriers and ranges. . . .	8
1.2	Symmetry operators and corresponding conservation laws.	12
2.1	The accelerator chain with associated energies for protons and lead ions.	25



Acknowledgements

For several years I have been part of the ALICE group at GSI and it has been a wonderful environment to work on this project. I would like to thank the group for all the support they offered and the many discussions we had, some related to my work, some related to physics, and others concerning all topics of life.

Crucial was of course the continuous and invaluable feedback and discussions with Ilya, which often extended outside the usual office hours.

Many people have left the group to different places during my time here. Mikolaj and Ionut were always interested in a discussions about flow or programming, and we also found common interests in excursions to various, but mainly one, location in Darmstadt Stadtmitte. Markus F., Markus K., Jacek and Jochen have all been valuable friends and colleagues. Jan and I started at a similar time and have been brothers in arms through lecture weeks and conferences. Fortunately many still remain. Steffen can always be bothered for a discussion about code, physics or more abstract topics. Also thanks to Steffen for making the translation for the German summary. Greatly enjoyable was to hear of Julius' adventures around the world.

Later the group was joined by Tona, Edgar, Tatiana and Lilith, all of whom contribute to the character of the group and I wish them lots of luck in the future.

Of course the many seniors in the group, Silvia, Anton, Ralf, Dariusz, Marian, Peter M., Kai, Ana and Alberica are all essential to what makes the ALICE group what it is, an incredibly interesting and welcoming place to study and develop as a physicist. As a group leader Silvia does incredible work for us all.

With Karin there was always time for a 'gezellig praatje' and offered a sense of a far away home at work.

Valuable and unforgettable time was spent abroad thanks to opportunities to work with Sergei and Ron at Wayne State University, and with Arkadiy at MEPH.

Also thanks to all the people who work at the HGS-HIRe and HQM graduate schools for offering excellent lecture weeks and support for travel and study.

Last but not least I want to offer special gratitude to my parents and to Tuğba. My parents have always supported me in where my studies took me, even if it was mostly not close to home. Tuğba, who though occupied with her own PhD work, was always there with unwavering patience, support and understanding, and without her this work could not have been done.



Curriculum vitae

PERSONAL INFORMATION

Name: Jacobus Onderwaater
Date of birth: July 28, 1987
Place of birth: Stavanger, Norway
E-mail: j.onderwaater@gsi.de
Nationality: Netherlands

EDUCATION & QUALIFICATIONS

Doctoral research at TU Darmstadt, Darmstadt 09/2012 - present
Thesis: Charge dependent correlations and collective dynamics in Pb–Pb collisions at $\sqrt{s_{NN}} = 2.76$ TeV.

Master Particle Physics at Utrecht University, The Netherlands 02/2010 - 08/2012
Thesis: Measurement of the Z boson Production in Lead-Lead Collisions at $\sqrt{s_{NN}} = 2.76$ TeV with the ATLAS Detector.
(Research done at Weizmann Institute of Science, Israel)

Bachelor Physics & Astronomy at Utrecht University, The Netherlands 09/2005 - 01/2011
Thesis: Parton Quenching in Heavy Ion Collisions.
Minors: Arabic language, Conflict studies.

OTHER RESEARCH EXPERIENCE

CERN summer student programme, LHCb 06/2011 - 08/2011
Reconstruction of Lambda and Xi baryons.

PHYSICS CONFERENCES AND WORKSHOPS

MEPhI heavy ion seminar (speaker) 2015
DPG (speaker) 2014; 2015
Chiral QCD (speaker) 2015
Hot Quarks (speaker) 2014
Quark Matter (poster presentation) 2014
International School on Quark-Gluon Plasma and Heavy Ion Collisions past, present, future 2013

PUBLICATIONS

"Detector non-uniformity corrections for collision symmetry plane estimates"

GSI Scientific Report 2015

doi: 10.15120/GR-2016-1

"Charge dependence of identified two-hadron correlation relative to the reaction plane in Pb-Pb collisions measured with ALICE"

Proceedings, Hot Quarks 2014

J.Phys.Conf.Ser. 612 (2015) no.1, 012044

doi: 10.1088/1742-6596/612/1/012044

"Charge dependent correlations with identified hadrons relative to the reaction plane with the ALICE experiment at the LHC"

GSI Scientific Report 2014

doi: 10.15120/GR-2015-1

"Azimuthal correlation measurements in a heavy-ion collisions"

GSI Scientific Report 2013

doi: 10.15120/GR-2014

"Measurement of Z boson Production in Pb+Pb Collisions at $\sqrt{s_{NN}} = 2.76$ TeV with the ATLAS Detector"

Phys.Rev.Lett. 110 (2013) no.2, 022301

doi:10.1103/PhysRevLett.110.022301

Erklärung zur Dissertation

Hiermit versichere ich, die vorliegende Dissertation ohne Hilfe Dritter nur mit den angegebenen Quellen und Hilfsmitteln angefertigt zu haben. Alle Stellen, die aus Quellen entnommen wurden, sind als solche kenntlich gemacht. Diese Arbeit hat in gleicher oder ähnlicher Form noch keiner Prüfungsbehörde vorgelegen.

Darmstadt, den 6th November 2017

(J. Onderwaater)